

Department of Materials Science

PhD program Materials Science and Nanotechnology Cycle: XXX

Curriculum: Industrial

NOVEL APPROACH TO RUBBER REINFORCEMENT BY SEPIOLITE NANOFILLER

PhD Candidate: Elkid Cobani

Registration number: 073278

Tutor: Dr Barbara Di Credico

Supervisor: Dr Luca Gianinni

Coordinator: Prof Marco Bernasconi

ACADEMIC YEAR 2016 / 2017

Contents

1	Introduction and Aims	
1.1	<i>Polymer nanocomposites and the nanoeffect in rubber materials</i>	3
1.2	Nanofillers in rubber polymers	5
1.2.1	Clay – LS	8
1.2.1.1	Sep clay	12
1.3	<i>Rubber NCs for tires applications: properties and performance</i>	13
1.3.1	Mechanical properties of Rubber NC	14
1.3.2	Tire performance: Rubber polymer influences	16
1.4	<i>Filler in rubber NCs</i>	17
1.4.1	Silane coupling agents chemistry	17
1.4.2	NC Morphology and filler networking	21
1.4.3	Rubber reinforcement	23
1.5	<i>Clay Rubber NCs for tires applications</i>	27
1.6	<i>Aim of the thesis</i>	30
1.6.1	Structure of the thesis	31
1.7	<i>Bibliography</i>	33
2	Materials, Procedures & Methods of Characterization	
2.1	<i>Materials</i>	43
2.1.1	Rubber	44
2.1.2	Fillers	48
2.1.3	Silane coupling agent	49
2.1.4	Curing agent and additives	49
2.2	<i>Procedures</i>	50
2.2.1	Acid filler treatment approach	50
2.2.1.1	Acid treatment of SepS9 and SepB5	52
2.2.1.2	One-pot procedure for acid treatment/silanization SepS9 and SepB5	52
2.2.2	Ionic functionalization of SepS9	52
2.2.2.1	Basic treatment and ionic functionalization of SepS9	53
2.2.2.2	Synthesis of sulfonated SBR	53
2.2.3	Preparation of Sep/SBR nanocomposites by melt mixing	54
2.2.3.1	Preparation of Sep/SBR nanocomposites	56
2.2.3.2	Preparation of TC materials	56
2.2.4	Preparation of Sep/SSBR nanocomposites by solution mixing	57
2.3	<i>Methods of Characterization</i>	58
2.3.1	Morphological, structural and spectroscopic characterization of fillers	58
2.3.1.1	Electron microscopy	58

2.3.1.2	X-Ray Diffraction	59
2.3.1.3	Infrared spectroscopy	59
2.3.1.4	Nuclear Magnetic Resonance (NMR)	59
2.3.1.5	Inductively Coupled Plasma Atomic Emission Spectrometry (ICP-AES)	60
2.3.2	Morphological, structural and spectroscopic characterization of nanocomposites	60
2.3.3	Dynamic-mechanical analysis of nanocomposites	61
2.3.3.1	Rubber Process Analyzer (RPA) of Sep/SBR Nanocomposites	61
2.3.3.2	Dynamic Mechanical Thermal Analysis (DMTA) of Sep/SBR Nanocomposites	62
2.3.3.3	Tensile Test	63
2.3.4	Static and dynamic mechanical characterization of TC materials	63
2.4	Bibliography	64
3	Sep Rubber Nanocomposites by Melt Mixing: Results and Discussion	
3.1	<i>Modified Sepiolites NS-SepX and NS-SilSepX: chemical structural and characterization</i>	69
3.1.1	Morphological investigation by SEM and TEM analyses	69
3.1.2	Powder X-Ray diffractometry	72
3.1.3	FT-IR Spectroscopy	74
3.1.4	Solid State NMR	77
3.1.5	Elemental analysis	83
3.1.6	ICP-AES analysis Mg ²⁺ determination	84
3.1.7	Nitrogen adsorption-desorption experiments	86
3.2	<i>Sep SBR Nanocomposite</i>	91
3.2.1	Rheological and dynamic-mechanical properties	91
3.2.2	Temperature dependent dynamic-mechanical analysis	97
3.2.3	Morphology characterization by HR-TEM	103
3.2.4	Analysis of immobilized rubber at filler/rubber interface by TD-NMR	112
3.3	<i>TC Sep Nanocomposite</i>	120
3.4	<i>Bibliography</i>	122
4	Sep Ionomer Nanocomposites by Solution Mixing: Results and Discussion	
4.1	<i>Ionic interaction in PNCs</i>	129
4.2	<i>Chemical and morphological characterization</i>	132
4.2.1	Characterization of SBR by FT-IR spectroscopy	132
4.2.2	Characterization of N'SepS9 by ²⁹ Si NMR	133
4.2.3	Morphological investigation of N'SepS9 by SEM	135
4.3	<i>Sep Ionomer NC characterization</i>	136
4.3.1	Micro-structure and morphology N'SepS9-SSBR nanocomposite	136
4.3.2	Mechanical properties of N'SepS9-SSBR	137

4.3.3	Temperature dependent dynamic-mechanical analysis	139
4.4	<i>Bibliography</i>	141
	Conclusions	143
A	Appendix: Characterization Methods	
A1	SS-NMR: Hydrogen content of the sepiolite fillers from ¹ H FID analysis	147
A2	Solid State NMR	149
A3	Attenuated Total Reflectance Fourier Transform Infrared Spectroscopy (ATR-FTIR)	150
A4	Nitrogen physisorption measurements	150
A5	Scanning Electron Microscope (SEM)	153
A6	High-Resolution Transmission Electron Microscopy (HRTEM)	154
A7	Oscillating Dish Rheometry (ODR) and stress-strain measurements	155
A8	Dynamic Mechanical Thermal Analysis (DMTA)	155
A9	Tensile Tests	156
A10	Inductively coupled plasma (ICP)	157

Abstract

The incorporation of different types of nanoparticles (NPs) into the elastomer matrix is now a growing area of interest rubber research in order to produce high-performance polymer nanocomposites (PNCs). However, the “nanoeffect” on the materials properties and performance can be observed only in the presence of controlled dispersion and distribution of filler particles in the polymer matrix. Due to their unique structure and physical properties associated with two-dimensional confinement, clay fillers are of great interest because environmental friendly, naturally occurring and readily available in large quantities at lower cost compared to the other fillers. Nevertheless, the clay dispersion and distribution in the polymer matrix to the point where particles are coated by the polymer, are still extremely critical. For this, it is necessary to chemically modify a natural clay in order to favors: i) good clay compatibilization and dispersion in polymer matrix, ii) effective chemically filler-rubber interaction and simultaneously iii) well-defined NPs spatial organization and distribution that influence the material properties, such as reinforcing and hysteretical properties in rubber NCs for tire application

In this context, this PhD thesis proposes the use of sepiolite (Sep) clay with intrinsically anisotropic character as possible reinforcing filler for rubber NCs. Since this system presents some drawbacks, such as poor compatibilization with the rubber, due to his hydrophilic character, and low concentration of superficial hydroxyl groups, that make them less reactive with the typical compatibilizers, the chemical surface modification of Sep fibers is mandatory. With this aim, pristine Sep was structurally modified by an acid treatment, which provides nano-sized Sep (NS-Sep) fibers with reduced particle size and increased silanol groups on the surface layer. The simultaneous functionalization with bis[3-(triethoxysilyl)propyl] tetrasulfide (TESPT) allows

to obtain *ex-situ* compatibilized Sep (NS-SilSep). NS-Sep and NS-SilSep fibers were used to prepare styrene-butadiene rubber (SBR) NCs with enhanced mechanical properties. Dynamic-mechanical analysis of Sep NCs demonstrated that the NS-Sep and NS-SilSep fibers provided an excellent balance between reinforcing and hysteretic behavior compared with large-sized pristine Sep and isotropic silica. This was related to the enhanced interfacial chemical interaction between NS-Sep/NS-SilSep and rubber, as well as to the size and self-assembly of anisotropic nanofibers. They form filler network structures, as supported by low field ^1H Nuclear Magnetic Resonance analysis (NMR) and transmission electron microscopy analyses (TEM). In detail, TEM analysis shows that inside elastomeric matrix, the Sep smaller size allows the self-assembly of fibers in Sep network structures, while the NMR reveals the presence of surface-immobilized rubber only in the presence of both modified NS-Sep and NS-SilSep fillers. Thus, the preparation of NCs, based on Sep nanofibers obtained by a versatile acid treatment, is a simple and effective method to prepare Sep NCs suitable for advanced technological applications.

An alternative approach to modified Sep fibers was proposed, suitable for prepare rubber NCs. This consists of the functionalization of Sep and SBR with amino-silane and sulfonate groups respectively, that can be positively or negatively ionized in aqueous solution and interact by ionic bonds. Thus Sep NCs were successfully prepared by solution mixing of functionalized Sep and SBR, showing an effective enhancement in the mechanical properties. Preliminary investigations support that filler-rubber ionic interaction favors the self-assembly of highly aligned filler in domains in which polymer chains are bridge between Sep fibers.

In summary, the whole results suggest that Sep clay, suitable modified, can be a promising filler for energy saving tires.

Riassunto

L'introduzione di differenti tipi di nanoparticelle (NP) in matrici polimeriche è attualmente un'area di crescente interesse per la ricerca sulla gomma al fine di ottenere nanocompositi polimerici (NCP) ad alte prestazioni. D'altra parte, l'effetto "nano" sulle proprietà del materiale può essere osservato solo in presenza di una dispersione e distribuzione controllate nella matrice polimerica. Grazie a proprietà strutturali e fisiche uniche, associate con il confinamento bidimensionale, i *clay* sono *filler* di grande interesse perché a basso impatto ambientale, facilmente reperibili in natura e disponibili in grande quantità a un costo più basso rispetto agli altri *filler*. Ciononostante la dispersione e distribuzione dei *clay* fino al punto in cui le particelle sono rivestite dal polimero sono ancora punti estremamente critici.

Per questo è necessario modificare chimicamente un *clay* naturale in modo tale da favorire: i) una buona compatibilizzazione e dispersione del clay nella matrice polimerica, ii) una interazione efficace tra il *filler* e la gomma e simultaneamente iii) una ben definita distribuzione e organizzazione spaziale delle NP, che influenzano le proprietà del materiale, così come le proprietà di rinforzo e di isteresi nei NC in gomma per applicazioni nei pneumatici.

In questo contesto, questa tesi dottorale propone l'uso della sepiolite (Sep) con un carattere intrinsecamente anisotropo come possibile *filler* rinforzante per NC in gomma. Poiché tale sistema presenta alcuni inconvenienti, quali bassa compatibilità con la gomma dovuta al suo carattere idrofilico e bassa concentrazione di gruppi idrossilici superficiali, che lo rendono poco reattivo con i tipici compatibilizzanti, è obbligatoria la modifica chimica superficiale delle fibre di Sep. Perciò, l'originale Sep era strutturalmente modificata mediante un trattamento acido, che produce fibre di Sep di grandezza nano (NS-Sep) aventi dimensioni ridotte della particella e aumento dei siti silanolicci superficiali. La simultanea funzionalizzazione con bis[3-

(trietossisilil)propil]tetrasolfuro (TESPT) ha permesso di ottenere nanoparticelle di Sep precompatibilizzate (NS-SilSep). Le fibre NS-Sep e NS-SilSep erano usate per preparare NC a base di gomma stirene-butadiene (SBR) con migliorate proprietà meccaniche. L'analisi dinamo-meccanica dei NC a base di Sep producono un eccellente bilancio tra isteresi e rinforzo rispetto alla Sep di dimensioni maggiori a alla silice isotropica. Ciò è stato relazionato all'aumento dell'interazione interfacciale tra NS-Sep e polimero, così come alle dimensioni e all'autoassemblaggio delle nanofibre anisotropiche. Queste formano un *filler* network, come dimostrato dalle analisi di risonanza magnetica nucleare a basso campo (NMR) e di microscopia elettronica di trasmissione (TEM). In particolare, l'analisi TEM mostra che all'interno della matrice elastomerica, la minore grandezza delle particelle permette l'autoassemblaggio in un network organizzato, mentre l'analisi NMR evidenzia la presenza di uno strato di gomma immobilizzata solo nel caso delle fibre modificate NS-Sep e NS-SilSep. Quindi la preparazione dei NC, basati su nanofibre, ottenute mediante un versatile trattamento acido, è un semplice e efficace metodo per preparare NC contenenti Sep per applicazioni tecnologiche avanzate.

Un approccio alternativo per modificare le fibre di Sep era proposto, adatto alla preparazione di NC in gomma. Questo consiste nella funzionalizzazione di Sep e SBR rispettivamente con un gruppo amminosilano e solfonico, che possono essere ionizzati positivamente o negativamente in soluzione acquosa e interagire mediante legami ionici. Quindi NC contenenti Sep erano preparati con successo mediante mescolamento in soluzione di Sep e SBR funzionalizzati, mostrando un effettivo aumento nelle proprietà meccaniche. Analisi preliminari sostengono che l'interazione ionica *filler*-gomma favorisce l'autoassemblaggio dei *filler* fortemente allineati in domini in cui le catene polimeriche sono a ponte tra le fibre di Sep.

In sintesi, questi risultati suggeriscono che la Sep, opportunamente modificata, può essere un promettente filler per pneumatici ad alta efficienza energetica.

Glossary

AR	Aspect Ratio
ATR-FTIR	Attenuated Total Reflection-Fourier Transform Infrared Spectroscopy
BR	Butadiene Rubber
CP-MAS	Cross-Polarization Magic-Angle Spinning
DMTA	Transmission Electron Microscopy
HR-TEM	High Resolution Transmission Electron Microscopy
ICP-AES	Inductively Coupled Plasma Atomic Emission Spectrometry
IR	Isoprene Rubber
LS	Layered Silicates
NMR	Nuclear Magnetic Resonance
NC	Nanocomposite
NP	Nanoparticles
NR	Natural Rubber
NIM	Nanoscale Ionic Materials
NS-SepX	Nano-Sized Sepiolite X
NS-SilSepX	Nano-Sized Silanized Sepiolite X
NS-SepX/SBR	SBR-based Nanocomposite containing NS-SepX
NS-SilSepX/SBR	SBR-based Nanocomposite containing NS-SilSepX filler
N'SepS9	SepS9 functionalized with aminosilane group
N'SepS9-SSBR	Ionomer Nanocomposite obtained by solution mixing
PCN	Polymer Nanocomposite
SepX	SepS9 or SepB5
SBR	Styrene Butadiene Rubber
SEM	Scanning electron microscopy
Sep	Sepiolite
SepX	SepS9 or SepB5

SSBR	SBR functionalized with sulfonic group
TC	Technical Composition
TESPT	Bis (3-triethoxysilylpropyl)tetrasulfide
TD-NMR	Time Domain NMR
V	Vulcanized
V-NS-SepX/SBR	Vulcanized SBR-based Nanocomposite containing NS-SepX filler
V-NS-SilSepX/SBR	Vulcanized SBR-based Nanocomposite containing NS-SilSepX filler
XRD	X-Ray Diffraction

1

Introduction and Aims

1.1 Polymer nanocomposites and the *nanoeffect* in rubber materials

Nanoscience and nanotechnology consist of a multidisciplinary area combining physics, chemistry, material science and electronics. It's one of the most fascinating and revolutionary study area of this century. As generally defined, nanoscience and nanotechnologies are based on design, characterization, production and application of structures, devices and systems by controlling shape and size at the nanometric scale (1-100 nm). Much of nanoscience and many nanotechnologies are concerned with producing new or enhanced materials, such as polymer nanocomposite (PNC).

PNC represent a new class of material alternative to conventional filled polymers, in which *nanosized* inorganic particles (at least one dimension) are dispersed in polymer matrix offering tremendous improvement in the polymer performance.

These novel materials benefit from the synergy between filler NPs and polymer chains interaction and the large quantity of interfacial area relative to the volume of the material [1][2]. The combination of polymer and NP provides an added value in materials properties that are neither displayed by the individual phase or conventional composites. In fact, PNCs often exhibit remarkable properties including unique mechanical and electrical conductivity, solvent resistance and diffusion barrier improvement, flame retardant and thermal properties. Thus, PNC offer significant potential in numerous industrial applications, such as energy storage, novel catalysts, transportation sector, construction/building, defense system and so on [3],[4],[5] (Fig. 1.1). The first example of PNC was in the field of automotive industry in the late 1980. Toyota researchers found that the incorporation of exfoliated clay *nanosheets* produced remarkable property enhancement of nylon, especially in term of reinforcement effect [6]. Since then, the incorporation of different types of *NP* into the elastomer matrix

have become a prominent area of current composite research in order to produce high-performance materials.

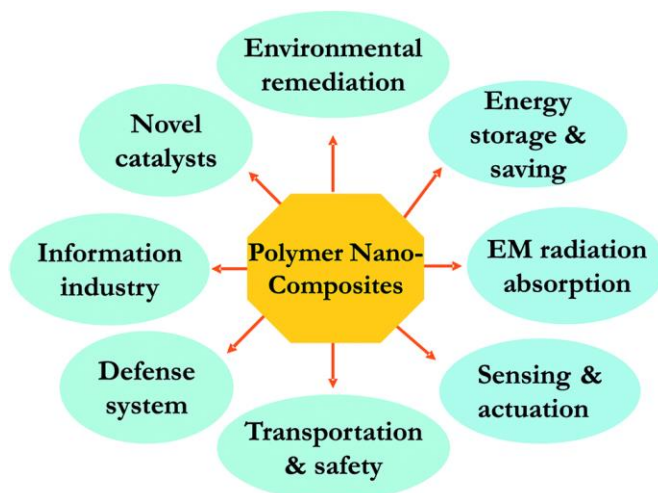


Figure 1.1 Application of PCNs [7]

Among polymer composites, rubber composite is a formulate obtained by the combination of an elastomer (e.g. NR Natural Rubber, IR Isoprene Rubber, BR Butadiene Rubber, SBR Styrene Butadiene Rubber, NBR Nitrile butadiene, CPR Chloroprene rubber) and inorganic fillers which are fundamental for making them applicable in various fields, such as the manufacture of tires and inner tubes or other industrial including various belts, hoses, oil seals, gaskets and so on.

Carbon black and mineral fillers such as silica has been widely used in rubber industry for the past many decades to improve rubber properties. Usually a high percentage, around 20–40 wt% conventional fillers are needed to get adequate reinforcement varying on the applications. However, there are certain drawbacks associated with these traditionally filled rubbers. Due to the high structure of carbon black strong shear fields or filler modification needed to ensure fine dispersion. Higher content of filler reduces the processability and increases the weight of the final product.

Under these circumstances, the *nano* effect has become highly relevant for rubber compounds since their application requires filler reinforcement [8]–[10]. Okada et al [11] observed that the mechanical properties of NR with 10 parts for hundred rubber (phr) of organoclay have been comparable to the compound with 40 phr of carbon black, many researchers and industrialists have prepared various rubber nanocomposites by considering the number of potential *nanofillers* such as carbon nanotubes (CNTs), polyhedral oligomeric silsesquioxane (POSS), lignine, cellulose, talc, silica, layered silicates (LS).

1.2 Nanofillers in rubber polymers

Nanofillers have an crucial role on the improvement of rubber materials properties such as hardness, toughness wear resistance, rolling resistance and wet grip [12]. Nanofillers have at least one of the particle dimensions on the nanometric scale in order to obtain higher properties respect to the traditional macro- and micro-sized fillers, such as in reinforcing effect (Fig. 1.2).

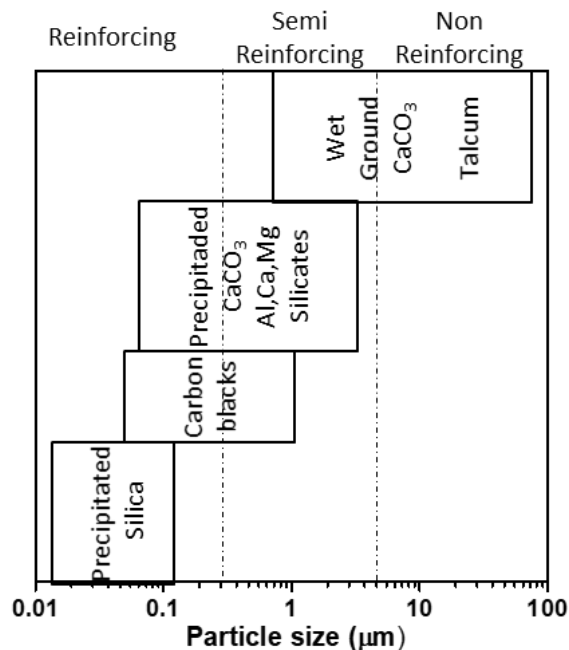


Figure 1.2 Classification of filler reinforcing effect according to particle size

Many types of nanofillers (Fig. 1.3) can be incorporated in PCN for reinforcement issue.

Among black nanofillers, CNTs are of particular interest in the field of material science to develop significantly lightweight strong materials. CNTs are made of cylindrical graphitic sheets with fullerene end-caps, diameter ranging from 1 to 100 nm and length up to several millimeters. Based on the structure, there are single walled (SWCNT) and multi walled (MWCNT) nanotubes and both are widely used as nanofillers. Owing to their structural characteristics, electrical and mechanical properties, CNTs are used in a wide variety of applications in the automotive and aerospace industries [13], [14].

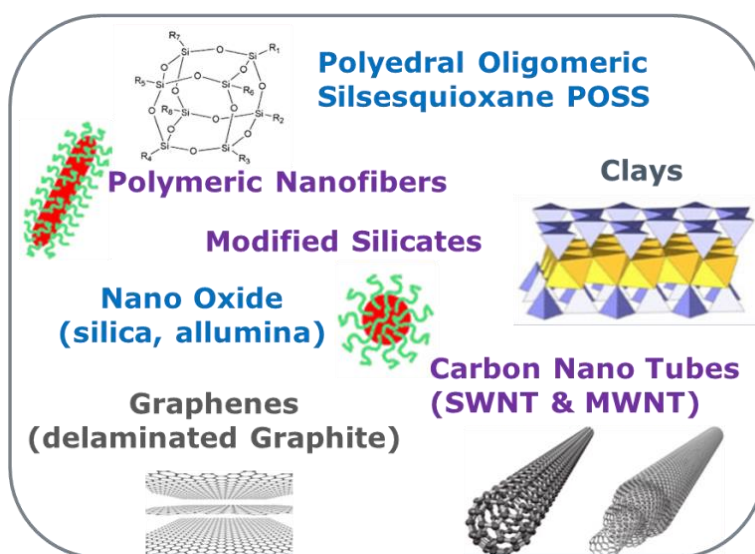


Figure 1.3 Nanofillers used in rubber polymers

POSS chemical technology is the recent development in PCN science and technology. POSS molecules are considered as the smallest particles possible for silica. POSS having combined organic/inorganic material properties are excellent lightweight, high performance hybrid materials used to modify many polymer properties. Having 1–3 nm diameter, POSS can enhance the service

temperatures, decomposition temperatures, oxidation resistance, surface hardening, mechanical properties, flame retardancy, heat evolution etc. of several polymeric materials to a great extent [15].

Very recently, bionanofibers and their nanocrystals obtained from natural resources have been used as reinforcing agents in several polymeric matrices and have attracted the attention of researchers. Bionanofibers include nanocellulose, nanochitin and nanostarch and their nanocrystals [16],[17].

Among the so-called "white" reinforcement nanofillers, silica is the most important filler. Depending on the synthetic method used for preparation it is mainly classified in three categories: precipitated silica (Fig. 1.4), fumed silica and silica gel [18], [19].

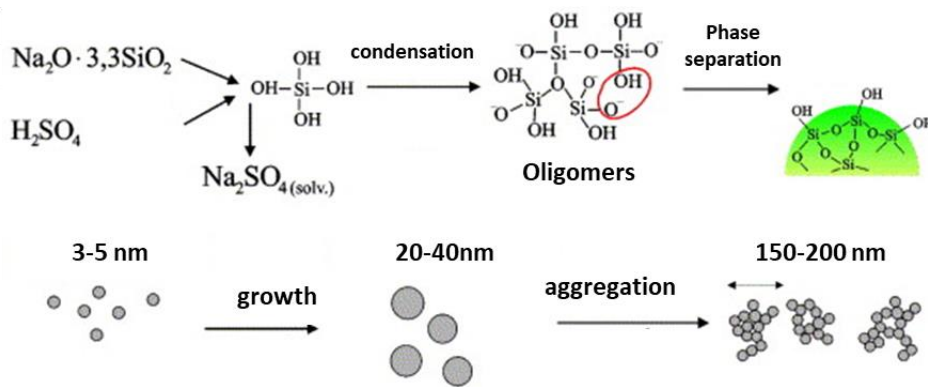


Figure 1.4 Schematic representation of nanosilica precipitation process

Silica fillers, having three dimensions in the nanometer regime, are spherical nanofillers. The average dimensions of silica nanoparticles (NPs) ranges from 5 to 40 nm with a high specific surface area (40-850 m^2/g). because of high content of silanol groups on silica surface, aggregates (100 – 500 nm) of multiple primary particles are formed by chemical and physical-chemical interactions. In addition, the aggregates are condensed into agglomerates (1 – 40 μm) by polar interaction and Van der Waals forces. Usually silica agglomerates are disintegrated during rubber mixing, more or less to the size of aggregates, but tend to rapidly re-

agglomerates after mixing. This results in a poor dispersion and low interaction with rubber. This difficult mixing and dispersion behaviour of hydrophilic silica are often managed with a silane coupling agent.

Although, approximately silica is used in tire industry is $>10^9$ kg/year corresponding to an average of 1 kg per produced tire. Recently interest has been shown in the use of clay and layered silicates [20], [21]

1.2.1 Clay – LS

Clay is a class of minerals with a fine-grained particles with an equivalent spherical diameter of less than $2\mu\text{m}$ and a general chemical formula $(\text{Ca}, \text{Na}, \text{H})(\text{X})_2(\text{Si}, \text{Al})_4\text{O}_{10}(\text{OH})_{2-n}\text{H}_2\text{O}$ [22], where X is a metal like Al, Mg, Fe, Zn. They include natural and synthetic clays such as mica, bentonite, magadiite, laponite, fluorohectorite and so on. Fig. 1.5 summarizes the major class of clays.

Most of clays belong to the category of LS or phyllosilicates because they are composed from alternating sheets of tetrahedral SiO_2 and octahedral layers of XO_6 in a 1:1 ratio, such as halloysite and kaolinite, or 2:1 ratio such as montmorillonite and sepiolite (Sep).

One side of the tetrahedral layer remains linked through a common oxygen atom (Fig 1.6a) and the different rearrangement of this structure give rise to different materials (Fig 1.6b, c and d). The layer thickness is around 1 nm and lateral dimension vary from 30 nm to several μm ; as a result, they possess a high aspect ratio. Therefore, polymer/silicate nanocomposites provide an attractive method to improve the polymer properties such as stiffness, strength and barrier properties without any change in processing technique.

The 2:1 type of LSs is characterized by a moderate negative surface charge that is due to the partial replacement of Si^{4+} for Al^{3+} in the tetrahedral sheets and Al^{3+}

for Mg^{2+} in octahedral sheets. For this the galleries are occupied by cations to counterbalance the excess of negative charges.

These cations can be exchanged by bulkier organic cations, typically alkyl ammonium ions. When the polar organic part is added, this replaces the inorganic ones. After the exchange the ammonium group is restrained on the clay surface while the hydrocarbon tail is positioned in the inter-layer space. This exchange has two main effect: the expansion of the interlayer spacing (Fig. 1.7 a and b) and the conversion of LS from hydrophilic into organophilic moiety.

The cation exchange allows: i) to enhance the interlayer clay distance and ii) to made clay hydrophobic. For this, it is the principal approach to disperse the clay nanofillers in polymer matrix.

Primarily, the interaction between polymer and LSs produce intercalated or exfoliated structure. A regular pattern of insertion of polymer in between the galleries of silicates can be found in intercalated structure. However, in exfoliated structure, the individual silicate layers of approximately 1 nm are separated and dispersed in a continuous polymer matrix. Usually the later system exhibits better properties due to the higher polymer/LS interactions.

Depending on the length of organic chain and its disposition in the interlayer space, different degree of intercalation [23] is possible and therefore there are different spacing of the layers. The efficiency of organoclay preparation by ion exchange depends from the cation exchange capacity (CEC) their specific surface area and the accessibility of the organic cation in the interlayer space. One of the most widely studied LS is Montmorillonite. The Montmorillonite CEC values is in the range of 80-120 mequiv/100g. As a consequence, is possible to prepare montmorillonite with weight fraction of ammonium up to 60% [24], favoring the dispersion and compatibilization in rubber NCs [25].

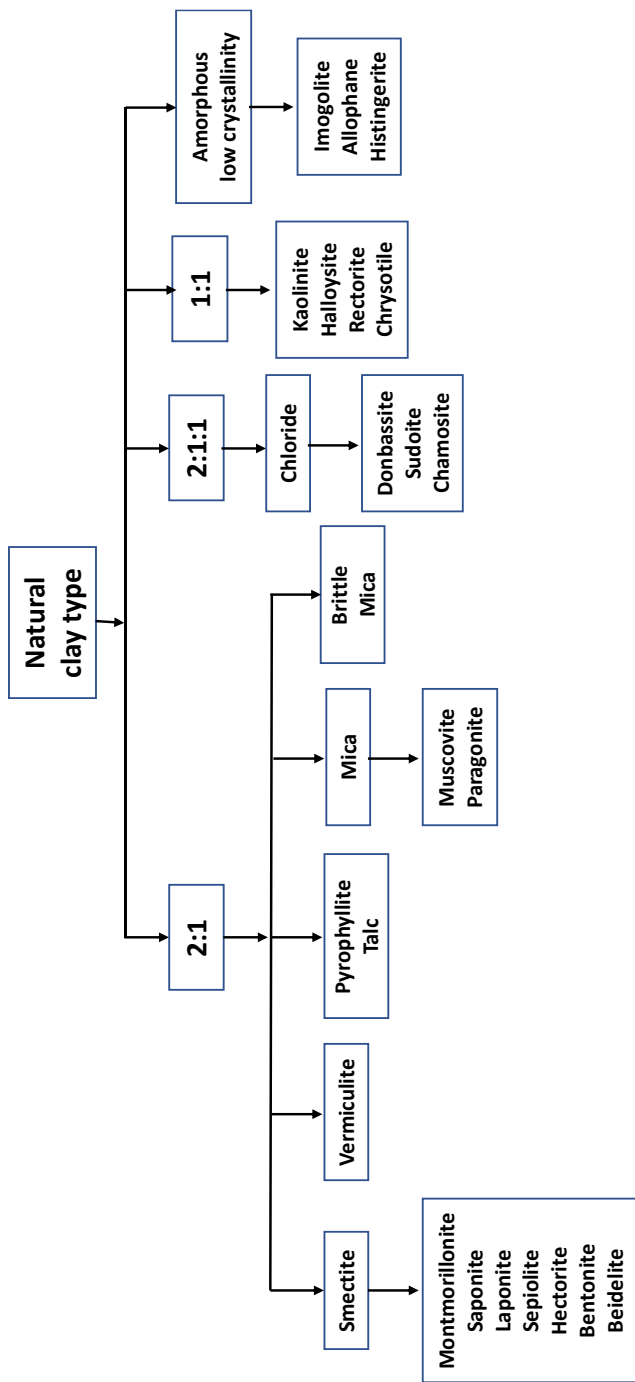


Figure 1.5 Natural clay classification referenza della figura

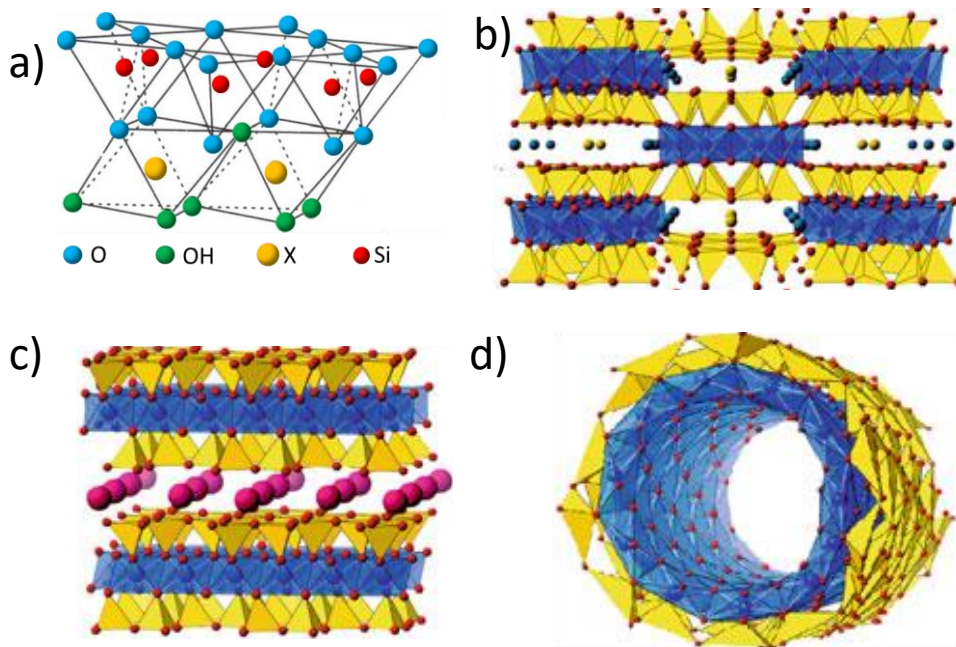


Figure 1.6 Schematic representation of (a) LS structure, (b) fibrous structure of Sep, (c) plate-like structure of montmorillonite and (d) and tubular form of halloysite

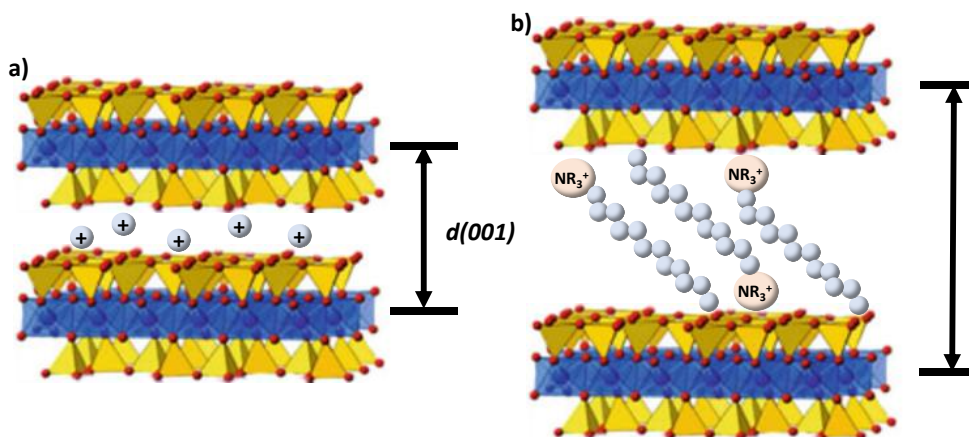


Figure 1.7 Schematic representation of (a) LS and (b) organically-modified LS

The maximum quantity of cations that can be exchanged is expressed in milli equivalent per 100 g of the dry clay and is denominated as ‘cation exchange capacity’ (CEC) of the clay [26].

Other clays of the same family, e.g. Sep, that have a low CEC and consequently a low affinity in the exchange procedure have found a limited application in the NC technology.

1.2.1.1 Sep clay

Sep is a magnesium layered silicate with the chemical formula $Mg_8Si_{12}O_{30}(OH)_4(H_2O)_4 \cdot 8H_2O$ with periodic structural interval along the b -axis and micropore tunnels along the c -axis with a dimension of 0.37×1.06 nm (Fig. 1.8 a and b) [27]. This provides a high specific surface area up to 300 m²/g.

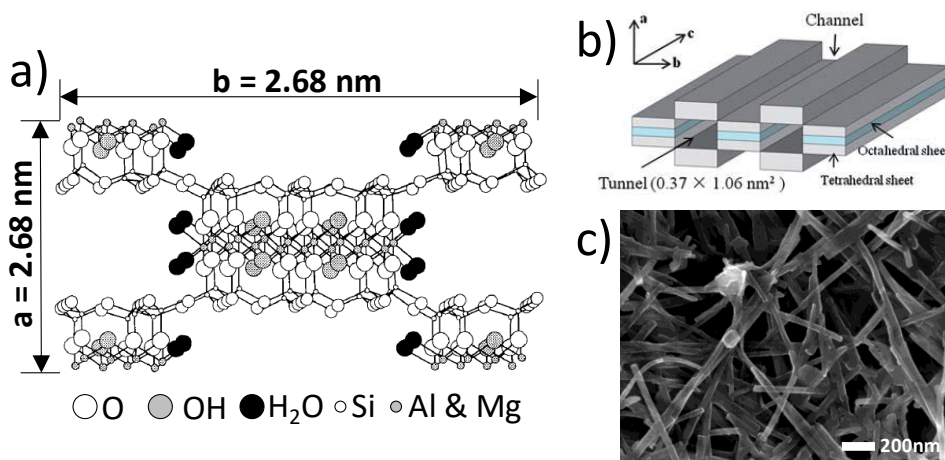


Figure 1.8 Schematic structure of (a, b) Sep and (c) its SEM micrograph

Sep has a rather unusual structure, organized in two-dimensional silica tetrahedral sheets including one central magnesium octahedral sheet, continuous in one direction. In the third direction, sheets have a thickness of about 1.34 nm and share each edge with the neighboring one, producing a “checkerboard” type pattern. As the sheets are covalently bonded they cannot be exfoliated. The Sep elemental particle appears as tiny fibers 40-150 nm width and 1-10 μ m length. Fibers usually stick together in bundles having 0.1 to 1 μ m

diameter. The bundles form randomly-oriented aggregates having size ranging 10-100 μm . The breaking down of these almost tightly packed aggregates is still a challenge for scientists, if they want to take advantage of the peculiar Sep shape for designing nanostructured materials.

The low value in CEC for Sep, that is a consequence of complex internal structure, limits the possibility to functionalize it with the traditional ways used for LS. Contrarily to the other LS, the silica layer at regular intervals in the *b*-axis undergoes an inversion of the tetrahedral sheets [28]. This discontinuity results in the presence of silanol groups at the edge of the channels and makes Mg^{2+} ions exposed to the external surface. The percentage of Mg^{2+} in weight of the pristine Sep is 10-15 % depending on the hydration degree, about 33% is estimated to be exposed to the external surface [29],[30].

Up to now some fundamental studies have been performed in Sep/nanocomposites in order to better control the Sep dispersion [31] and different functionalization treatments of Sep have been reported to prepare clay nanocomposites [32],[33]. Recently, de Lima et al. [34] proposed the Sep modification by ionic liquids, García et al. [35] by methoxysilanes in aqueous gels and Mejía et al. [36] by poly(ethylene glycol). These treatments demonstrate the positive effect of Sep functionalization on improving the nanofiber dispersion in polymer matrix and the functional properties of the nanocomposites. Besides these the results are related to specific materials, very different from rubber.

1.3 Rubber NCs for tires applications: properties and performance

Rubber NCs are a complex and multicomponent system, containing many different components with specific roles to play such as NR and/or synthetic rubbers, chemicals which function as antidegradants, curatives, processing aids

and reinforcing fillers. These materials are selected based on their physico-chemical properties and their interactions with other constituent materials to provide a broad range of mechanical properties.

1.3.1 Mechanical properties of Rubber NC

In an oversimplified picture, the properties derived from the combination of two system can be described from a classical rule of mixture that can be represented by equation 1.1:

$$P(NC) = \varphi P(f) + (1 - \varphi)P(m) \quad (1.1)$$

where $P(NC)$ are the property of the mixture, $P(f)$ and $P(m)$ the property of the filler and the matrix, φ the filler volume fraction and $(1-\varphi)$ the matrix volume fraction. This equation does not take in to account synergic factors originating from the filler and matrix mixing, which involve the formation of interphase and filler interparticle interaction.

As regards, rubber composite is a viscoelastic material it's properties are intermediate between that of an elastic and viscous material. As it deforms, a fraction of the energy is stored elastically, and the remaining is dissipated as heat in a hysteretic manner.

Viscoelastic behavior is most commonly characterized in an oscillatory dynamic mechanical test. The application of an oscillatory shear strain γ of angular frequency ω , results for a linear viscoelastic material in a sinusoidal stress σ , out of phase by an angle of δ as expressed in eq. 1.2

$$\gamma(t) = \gamma_0 + \sin(\omega t) \quad \sigma(t) = \sigma_0 \sin(\omega t + \delta) \quad (1.2)$$

By developing this equation, it is possible to obtain:

$$\sigma(t) = \sigma_0 [\sin(\omega t) \cos(\delta) + \cos(\omega t) \sin(\delta)] \quad (1.3)$$

Therefore, we can define:

$$G' = \frac{\sigma_0}{\gamma_0} \cos(\delta) \quad G'' = \frac{\sigma_0}{\gamma_0} \sin(\delta) \quad (1.4)$$

and the effect of reinforcement is commonly represented by the complex modulus G^* shown in equation 1.5

$$G^* = G' + iG'' \quad (1.5)$$

G^* is composed from an in-phase elastic component (G' , storage modulus) and an out of phase dissipative component (G'' , loss modulus). From these two components is possible to define $\tan\delta$ (dissipating factor) as the ratio G''/G' and which express the energy lost in cyclic deformation. The dissipative mechanism in rubber NC are reasonably well understood, but its mathematical formulation is rather complex, except in simple models. The model preferred for rubber NCs is the one-dimensional sinusoidal deformation of linear viscoelastic materials in a geometrically simple specimen. Actually, deformations that rubber NCs undergoes in tire working regime, are neither one-dimensional nor sinusoidal. As tire is used, it goes through revolution and is subjected to a three-dimensional, non-sinusoidal strain cycle, which hampers a mathematical analysis. The analysis is complicated further by non-linearities of the material response, and by temperature and frequency effects. These complexities forced researchers to resort in this simpler and linear sinusoidal model that can be a rough guide but if handled carefully can be quite useful.

The deformation of a tyre tread can be resolved approximately into a constant strain (bending) and a constant stress (compression) condition. Since the geometric mean of the hysteresis under these two conditions is approximately proportional to $\tan \delta$, tire tread hysteresis is as a first approximation, proportional to $\tan \delta$.

1.3.2 Tire performance: Rubber polymer influences

The $\tan \delta$ value has a high significance for the most important properties of a polymer. The significance of the $\tan \delta$ curve for a number of important functions of rubber is shown in Fig. 1.9 [37].

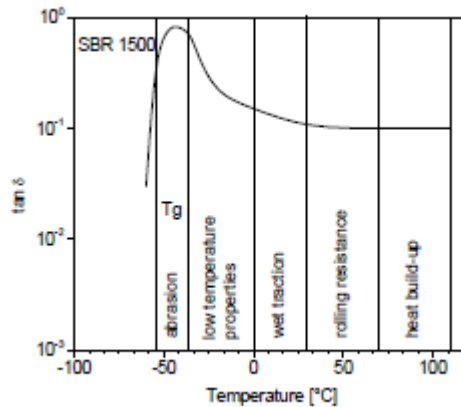


Figure 1.9 $\tan \delta$ as a function of temperature and related performance

The behaviour of the tyre for winter use can be related to $\tan \delta$ in the low temperature range, where the beginning of the glass state indicated by a strong upturn of the loss tangent marks the limit of elastic behaviour.

As an indicator of rubber grip/traction on wet, the level of the loss tangent around 0 °C till approximately +30 °C can be taken. In the range between +30 °C and approximately +70 °C, that is the running temperatures of a tyre, the loss factor essentially determines the degree of rolling resistance. At temperatures exceeding this limit the tyre enters into a region of maximum stress and reaches the limit of safe operation with the risk of destruction. $\tan \delta$ values in this range indicate the heat build-up behaviour and allow an estimate of incipient thermal decomposition and the limit of good tyre performance.

Since the peak in $\tan \delta$ correlates with the glass transition temperature (T_g) of the polymer, this value became a tool for the selection of a suitable tyre rubber.

The choice of the rubber polymer with the optimum Tg therefore plays a key role in modulating many tyre requirements.

1.4 Filler in rubber NCs

Reinforcing fillers are the second most abundant ingredients in rubber formulations after the rubber itself; this is testified by their presence in relatively high amount if compared to other rubber additives. The main features of the filler that impact on the NC properties are:

- Filler particle size: particles produced for tire application must be nanometric in size (at least along one dimension) to exert reinforcement on rubber, as represented in Fig. 1.2. Bulky particulate materials can be employed just to reduce the cost of the final material without any improvement of properties. In this case they can be simply called extenders or non-reinforcing fillers.
- Filler particle surface chemistry: the nature of the filler surface determines the type of bonding with the matrix (covalent, ionic, Van Der Waals, H-bond, etc.) and as a consequence controls the nanocomposite homogeneity and the mechanical properties related (wear/abrasion resistance, properties at break). While carbon black surface chemistry can be controlled by its degree of oxidation, silica or LS can be surface-modified with chemical compounds, in order to reduce their high hydrophilicity and to create a covalent bond with the matrix. This is the case of sulfurated silanes that are able to react both with silica and rubber; these are the benchmark coupling agents for tire applications.

1.4.1 Silane coupling agents chemistry

The difficult mixing and dispersion behavior of hydrophilic silica are often managed with a silane coupling agent, which change the surface polarity of silica and generate direct bindings with the rubber chains [38],[39]. Silane coupling

agents are used in a wide range of applications because of their unique ability to bond polymers with dissimilar materials such as inorganic oxides, silica, alumina and silicates.

Among silane coupling agents, bifunctional organic silane are widely used in rubber NCs, especially in the tire industry. A bifunctional organosilane coupling agent is generally characterised by two functions: one for the adhesion to the hydrophilic silica surface and the other for adhesion to or enhancement of the compatibility with the hydrophobic polymer matrix. Fig. 1.10 shows the silane coupling mechanism [16], [40]–[42].

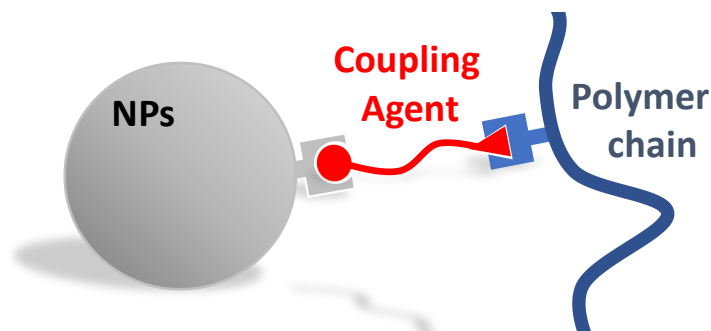


Figure 1.10 Coupling agent interaction mechanism

Coupling agents are used as a surface modification, either applied on the silica particle itself before the mixing, or by adding during the mixing to the rubber compound.

Silane coupling agents have usually three hydrolysable reactive alkoxy groups, e.g., $-\text{OCH}_3$, $-\text{OCH}_2\text{CH}_3$, and one non-hydrolyzable organo functional group, e.g. amino, vinyl, mercapto. They have also an organo spacer group typically aryl or alkyl that separates the organofunctional group from the silicon atom [43]. Typical commercial examples of silane coupling agents used in the tire industrie are illustrated in Table 1.1. The most commune used coupling agents in tire

industry are the bis(triethoxysilylpropyl) tetrasulphide (TESPT) and bis(triethoxysilylpropyl) disulphide (TESPD).

Coupling agents have been widely used and studied as compatibilizer for silica [39][44]. Many researchers have studied the TESPT silanization mechanism of silica NPs. The fundamental steps are reported in Fig. 1.11[45],[46].

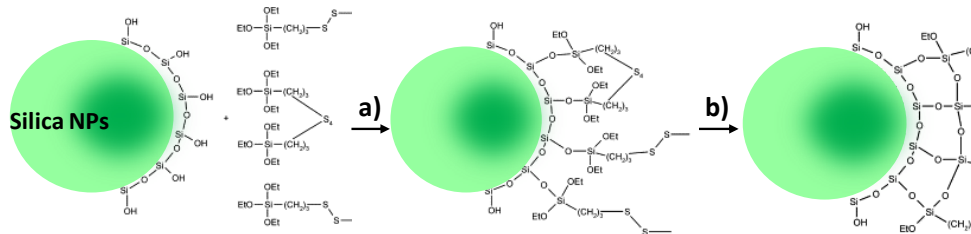
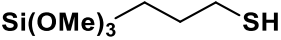
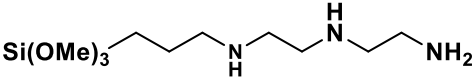
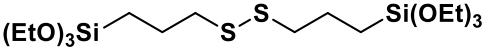
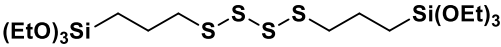
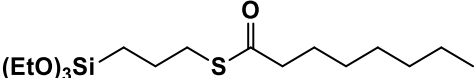


Figure 1.11 Silanization mechanism of silica NPs with TESPT: a) hydrolysis and condensation; b) intermolecular condensation.

The primary step involves the reaction of the first alkoxy groups following two possible mechanisms both releasing ethanol: the direct condensation (step a in Fig. 1.11) between the alkoxy group and silanol or the hydrolysis of the alkoxy group to form a silanol, which successively condensates with the silanols of silica. The rate of the condensation is faster than hydrolysis, which is the rate determining step of the primary reaction [47]. In the second step (step b in Fig. 1.11), the intermolecular condensation between the unreacted ethoxy groups of the grafted silanes occurs. This secondary reaction is slower compared to the primary one, but also a low degree of intermolecular condensation contributes in the improvement of reinforcing properties.

Table 1.1 Chemical structure of different coupling agents.

	TMSPM
	TMDETA
	VTEOS
	TESPD
	TESPT
	NXT

Recently silane grafting has proven to be an efficient alternative on modifying clay surfaces [48]–[51], this greatly enhances the interaction between clay and hydrophobic molecules by simply grafting hydrophilic silane groups on the surface [52]. Subsequently, the obtaining materials showed suitable properties for application in polymer clay NCs.

Silylation reaction of clays is slightly different from silica, it undergoes, in general, through different steps. As presented in Fig. 1.12. Firstly, silane undergoes a hydrolysis in presence of water to form a more reactive acid silanol group, that can partially self-condensate with other hydrolyzed silane. Different oligomers may be formed in this step. Next, this hydrolyzed silane and oligomers are physically adsorbed to the surface of the clay by hydrogen bonds with the hydroxyl present. At this point, a dehydration condensation reaction bonds the silane to the surface with a covalent Si-O-Si bond. Furthermore, the functional group R' remains available in the composite step formation and can react with the polymer chain resulting in the formation of the coupling agent interaction mechanism.

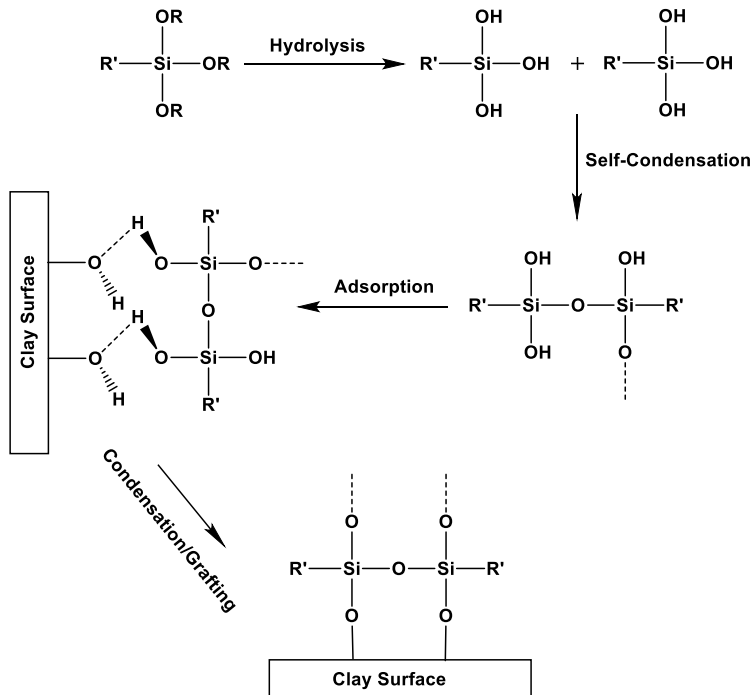


Figure 1.12 Different steps of silylation mechanism in clay.

In this way the resultant NC exhibit a significant enhancement of their properties, mechanical, rheological and handling properties[53]–[55]. Generally, the silanization can occur at the interlayer space, external surface and at the edges. The interlayer and edge grafting can increase the basal spacing of the clay layers

1.4.2 NC Morphology and filler networking

The simple mixing of a filler and a rubber matrix should result in homogeneous distribution of the filler, if the filler does not have a tendency to agglomerate. Aggregate formation starts to take place when the filler volume fraction is relatively high (>0.05) because the total interfacial area, while the interparticle distance is decreased. Not only, but the increasing in filler content result in a nonlinear change of the properties of the composite e.g. conductivity, permeability, mechanical properties (Fig. 1.13). A percolative threshold f_c is

achieved and all the aggregated nanoparticles become part of an extended network through the matrix as schematized from the insets of Fig. 1.13 [56].

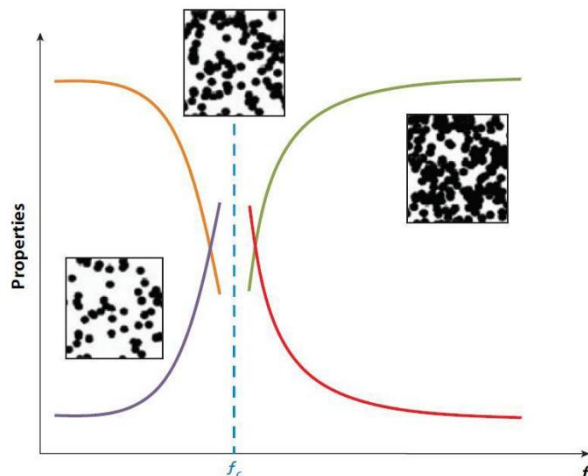


Figure 1.13 Scheme of nonlinear changes in the properties of composites near the percolation threshold f_c . The insets show the morphology during the phase transition of fillers in the composites near percolation [56]

This threshold can be defined as the filler fraction in which particles are interconnected. From a geometrical point of view, it is possible to define the maximum volume fraction to be 0.74 of the entire volume in the case of a closely packed spheres with equal radius [57]. However, in a polymer composite the actual percolation threshold values are much lower. The lower value is a consequence of the interaction occurring between particles (filler–filler interaction), between polymer and particles (filler–rubber interaction) and the formation of an interphase that allows the formation of a continuous network even without close packing of the particles.

Upon filler introduction, the polymer NC undergoes dramatic changes especially near f_c : polymers with filler content below f_c exhibit mainly viscous character, similar to the unfilled polymer, while above f_c the properties of the polymer are improved, increment in elastic modulus and decreased dissipating factor.

The key parameter that play an important role in the determination of f_c is not only the distribution of the filler in the matrix, but even geometric filler parameters. As the shape of the fillers changes the value of f_c which decreases to lower value for higher AR as shown in Fig. 1.14.

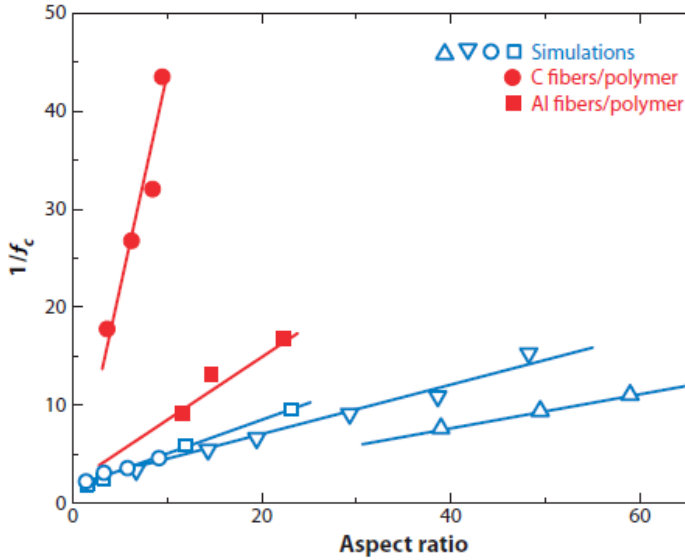


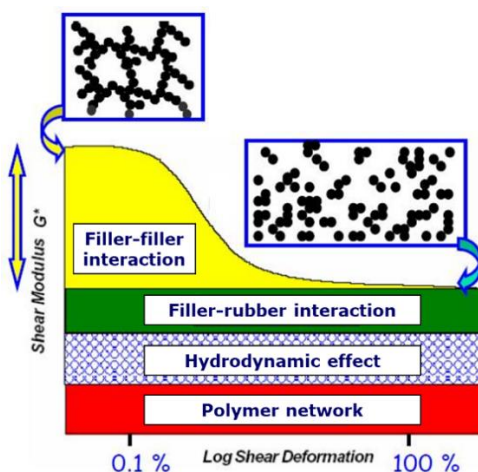
Figure 1.14 Dependence of the percolation threshold f_c on AR of the fillers in a randomly oriented matrix. Data presented in red express experimental data in blue are presented data from simulation results[58].

The formation of network is associated to a dramatic change on the mechanical properties, fillers with AR great than 1 allow to obtain higher reinforcement at low filler content. As an example, silica NPs and CB based NCs have a f_c of approximately 0.17 [59]. Layered silicates with their wide range of aspect ratio (5-100) exhibit lower value than spherical particles, even at 0.02 [60]. Finally, carbon nanotubes that can have AR in the range of 100 to 200 can percolate in rubber matrix even at lower volume fraction, 0.002 [60].

1.4.3 Rubber reinforcement

Several models have been proposed and used for the evaluation of the structural and compositional contribution on the reinforcement in terms of G' , G'' and

$\text{Tan}\delta$ [61], [62]. The most widely used model is based on the work of Payne, who studied the relation between the 3D filler aggregates and the dependence of the G' and G'' from strain. In this model, in the case of a viscoelastic material subjected to a low oscillatory strain, a sigmoidal decrease in the value of the initial storage modulus (G'_0) is observed until a plateau is reached at high strain (G'_∞). In fact, in a percolated system an interaction network of particles is diffused through the entire matrix. By applying a deformation, the filler network starts to break at low strain. The filler particles are held together by relatively weak forces, H-bonds or Van der Waals while covalent bonds exist at the interface with the filler through the coupling agent and the rubber structure. It is possible to define two main components contributing to the elastic modulus G' : a strain dependent component associated to the reinforcement due to the filler-filler interaction and a strain independent component mainly attributed to filler-rubber interaction (Scheme 1.1).



Scheme 1.1 Schematic representation of a stress-strain curve describing Payne effect and the strain independent contribution on reinforcement.

The extent of network breakdown can be quantified as difference between G'_0 and G'_∞ this is associated with an energy dissipative process. However, this network is not the only parameter that influences in the reinforcement. A key

role is played by the interaction at the interface between NPs and polymer. The presence of this contact surface (Fig. 1.15) introduces a constrain in the mobility of polymer chains as proposed by Medalia [63] and firstly observed by Tsagaropoulos [64]. The presence of a well-defined fraction of rubber with higher T_g respect to the bulk was detected by dynamic-mechanical thermal analysis (DMTA). The amount of this “rigid” fraction was correlated with the filler amount and exposed surface area [65]. Numerical methods were also proposed by Arrighi [66] in order to determine the amount of immobilized rubber from DMTA curves.

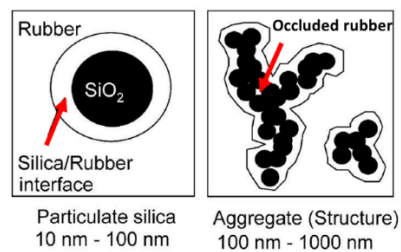


Figure. 1.15 Schematic representation of the rubber NP interface and the constrain rubber at this interface.

The interpretation of these observation have found opposition in literature [67], therefor further investigation were necessary to clarify this issue. There are experimental data suggesting that the mechanical reinforcement of crosslinked rubbers is mainly related to the secondary structure of filler particles and others suggesting chain stiffening due to the rubber filler interactions is the primary reinforcing mechanism. Intensive discussions have been held on the nature of this effect, but the exact causes of this non-linear behavior are still a matter of investigations.

NMR study on rubber NC have shown the presence regions with different mobility at the polymer NPs interface: a mobile region far from the particles, an outer shell with less mobility and an inner shell with very little mobility (Fig. 1.16) [68],[69]. The surrounding polymer layer is therefore divided into two

parts: a firmly anchored portion (close to the surface) and a weakly bound outermost portion composed of chains interacting with the strongly bonded area

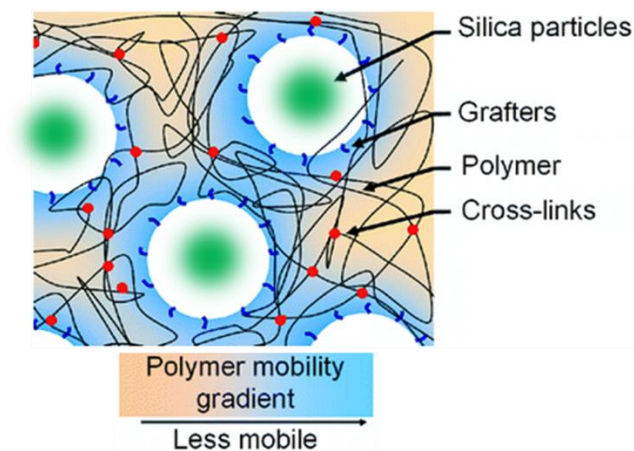


Figure 1.16 Representation of filler-rubber interface and polymer mobility gradient is evidenced.

By considering this layer that encapsulate the particles, the concept of the filler-filler interaction should be updated especially regarding the interpretation of the Payne effect. The polymer layers encapsulating each NP start to overlap when the percolative network is reached. So the destruction of the network is not only the rupture of weak bonds between the filler, but as the filler-filler is mediated by the interfacial rubber, the Payne effect can be associated to the disentanglement of the polymer chains[70].

The polymer layers surrounding each single NP overlap, connecting them in a percolative filler network diffuse throughout the whole nanocomposite [38].

Thus, filler network structure contributes to the total modulus together with the polymer network [71]. The rationale of this is that, in a given range of particle loading, the filler gives rise to interconnected structures, through both direct particles interactions, and their bridging by polymer chains [72]. This enable the material to support large dynamic loads over millions of load cycles. This has important technical implication for the control and reduction of rolling

resistance, directly linked to fuel efficiency and emission reduction, in tire materials as well as in many other elastomer applications involving dynamic loading. In this respect, the size and shape of the filler have a pronounced significance. In fact, it is clearly demonstrated that the anisotropic NPs in rubber matrix self-assemble in superstructures able to immobilize rubber [73],[74].

1.5 Clay Rubber NCs for tires applications

Recent studies have demonstrated that anisotropic filler particles provide a significant rubber reinforcement. The degree of reinforcement depends on the aspect ratio (AR) [74] and the ability of self-alignment that this anisotropic particles demonstrate [68].

In detail, it was observed that rod-like silica with different AR (2-10) compared to spherical one shows an increase in reinforcement. This reinforcement, beside the filler-filler interaction, is related to the AR and alignment that provide a higher percentage of immobilized SBR chains at the filler-rubber interface (Fig.1.17).

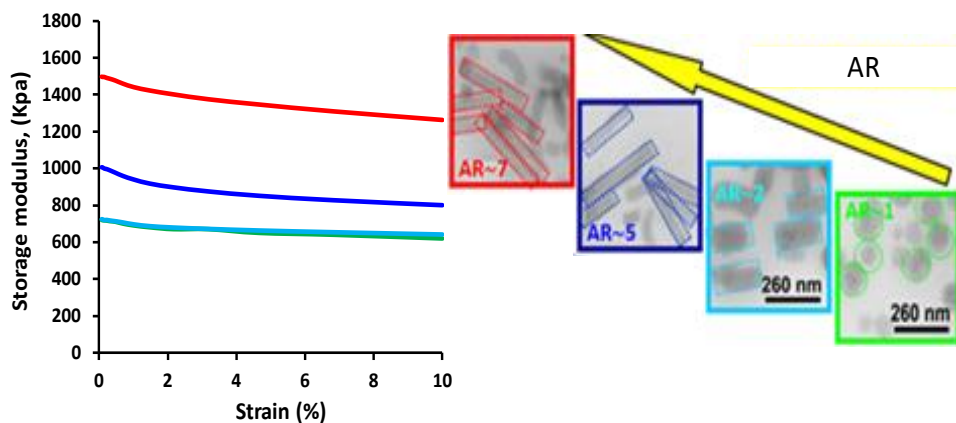


Figure 1.17 Effect of AR and particle alignment on the reinforcement

This suggests that the use of NPs with high AR and functionalities are a promising candidate as new filler, able to enhance the filler networking and promote the filler rubber interaction by increasing the immobilized rubber.

In this contest, rubber/clay nanocomposites have been of particular interest for the past few years due to their unique physical and chemical properties. Rubber/LS NCs exhibited good properties due to the high AR of LS arising from their platelet-like morphology. In the presence of LS, rubber nanocomposites can form either intercalated or exfoliated structure and partly intercalated and exfoliated structure (Fig. 1.18)[23], [75], [76].

Unfortunately, the *clay dispersion* and *distribution* in the polymer matrix to the point where particles are coated by the polymer is still extremely critical. This is mainly due to:

- i) poor dispersability of the LS due to the low affinity between the organic polymer and inorganic nature of the silicate,
- ii) LS is present as an aggregate or agglomerate of a macroscopic scale.

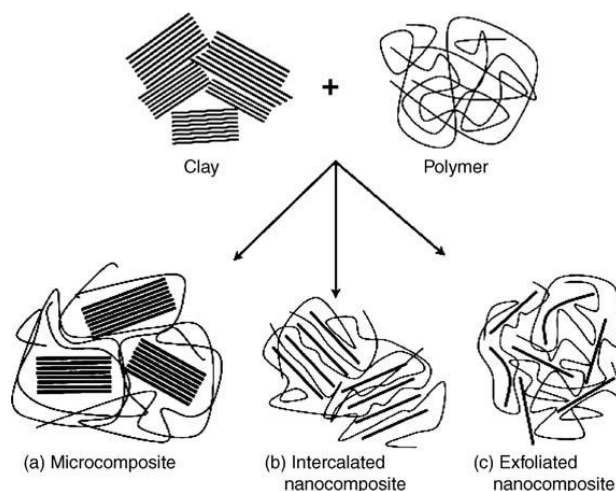


Figure 1.18 Scheme of possible dispersions of LS in a polymer [23]

Thus, a modification of the filler surface is required to favor the interfacial interactions. To this aim, the hydrophilic pristine clays are generally modified by organic molecules (typically cationic surfactants), via ion exchange reaction or by grafting reaction with silane-based coupling agents [77] [21].

These treatments improve the dispersion of clays in polymer matrix to the detriment of filler network. In fact, the clay particles in PNCs is arranged in small groups of finely dispersed clay tactoids (containing ~ 10 layers). These tactoids are largely isolated and separated each other by ~ 10 -50 nm without forming any rigid filler framework. This is due to the high level of dispersion clay in the rubber matrix, when exfoliated and organically-modified. For this an advantageous balance between good dispersion and well controlled distribution state of clay particles is still a challenge to improve the mechanical behaviour of a clay-based rubber material. It has been shown that changing the clay surface chemistry modifies also the filler distribution state in the matrix

In order to have a successful development of clay-based PNCs, it is necessary to chemically modify a natural clay so that it can be compatible with a chosen polymer matrix and simultaneously induce a well-defined spatial organization and NCs distribution in order to tailor material properties, such as reinforcement and rolling resistance. In fact, up to now, rubber systems containing clay particles not show the typical percolating network, that affect the total modulus and hysteretical property together with the polymer network.

Among clays, the use of pristine Sep in rubber NCs is very limited, once again due to its hydrophilic surface and to the consequent low affinity towards organic polymers. On the other hand, even if the Sep clays, organically-modified with alkyl ammonium groups, result more easily dispersible in a polymer matrix, the polymer-filler interaction is generally not improved because of hydrophilic silanol groups on the Sep surface [78]. Meanwhile, surface treatment via silane

coupling agent is poorly effective, consisting only in 10% of functionalized Sep [79], due to the low bonding sites number.

1.6 Aim of the thesis

The aim of the present work is to investigate the influence of the anisotropic Sep particles on the dynamic-mechanical behavior of the SBR NCs, based on the controlled modification of Sep fibers with specific and defined morphology and surface chemistry.

Moreover, the influence of the self-assembly of *nanosized* Sep particles in SBR matrix was studied, mainly considering the formation of the nanoscale rigid rubber at the interface with the filler.

In detail, a controlled acid treatment was performed in order to obtain modified Sep fibers, suitable for prepare Sep rubber NCs. This treatment provides needle-shaped Sep fibers with nanometric size (namely nano-sized Sep, NS-Sep), preserving the filler anisotropic features and increasing the amount of bonding sites at the Sep edge surfaces. The simultaneous silanization of Sep surface, during acid treatment, was also investigated by using tri-functional silane coupling agent. Morphological, spectroscopic and thermal analyses were performed for a complete characterization of the modified Sep clays. NS-Sep fibers were used to prepare SBR NCs by *ex-situ* blending. The filler-filler and filler-rubber interactions were investigated through dynamic-mechanical tests and by assessing the NS-Sep NC structure by transmission electron microscopy (TEM) analysis. The topography of the immobilized rubber were investigated by the integrated approach of TEM with low field Nuclear Magnetic Resonance (NMR).

An alternative approach (namely *second approach* in this thesis) was proposed in order to obtain Sep fibers, suitable for prepare rubber NCs. Amino silane functionalization of Sep was performed, after a basic treatment used for

increasing the number of hydroxyl groups by maintaining the shape and AR of the particles. Meanwhile the SBR matrix was functionalized with sulfonate group. These groups can be positively or negatively ionized in aqueous solution, promoting the ionic filler-rubber interaction. Therefore, the introduction of these groups in both Sep fillers and SBR polymer chains allows to prepare Sep *Ionomer* NCs by solution mixing. A complete characterization of the modified Sep and SBR was performed. The modified Sep NCs was preliminary investigated by TEM and static-dynamic analyses.

In both approach, self-assembly ability of modified Sep on rubber matrix was investigated and related to both filler network structures and mechanical properties of obtained NCs.

1.6.1 Structure of the thesis

The research described hereby employs filler/rubber model systems to understand the reinforcing mechanism operated by silica nanofillers, having spherical and/or rod-like particle shape:

Chapter 2 reports the materials, procedures and methods used in this thesis was. A complete description of the materials and their use was described, followed by the procedures of modification and preparation methods used. Also, methods used for the full characterization of the new materials was reviewed.

Chapter 3 is focused on the results related to Sep rubber NCs based on modified Sep fibers, obtained by applying a controlled surface treatment on bare Sep (*first approach*). A complete characterization of the modified Sep clays was reported followed by dynamic-mechanical analysis of clay PCNs. In addition, technical composites (TC) was investigated and possible industrial use of modified Sep as co-filler in tire formulations was illustrated.

Chapter 4 is dedicated to the preparation of Sep NCs by solution mixing, based on ionic filler-rubber of both modified Sep and SBR. For this Sep particles and SBR matrix were modified with functional groups that can be positively or negatively ionized in aqueous solution.

Conclusions sum up the main results and reports the findings of the investigation.

1.7 Bibliography

- [1] B. M. Novak, "Hybrid nanocomposite materials - Between inorganic glasses and organic polymers," *Adv. Mater.*, vol. 5, no. 6, pp. 422–433, 1993.
- [2] A. J. Crosby and J. Y. Lee, "Polymer nanocomposites: The 'nano' effect on mechanical properties," *Polym. Rev.*, vol. 47, no. 2, pp. 217–229, 2007.
- [3] D. Galpaya, M. Wang, M. Liu, N. Motta, E. Waclawik, and C. Yan, "Recent Advances in Fabrication and Characterization of Graphene-Polymer Nanocomposites," *Graphene*, vol. 1, no. 2, pp. 30–49, 2012.
- [4] H. Ishida and G. Kumar, Eds., *Molecular Characterization of Composite Interfaces*, 1st ed. Boston, MA: Springer US, 1985.
- [5] T. Agag, T. Koga, and T. Takeichi, "Studies on thermal and mechanical properties of polyimide \pm clay nanocomposites," *Polymer (Guildf.)*, vol. 42, pp. 3399–3408, 2001.
- [6] Y. Fukushima *et al.*, "Composite material and process for manufacturing same," 4.739.07, 1988.
- [7] C. Yang *et al.*, "Polymer nanocomposites for energy storage, energy saving, and anticorrosion," *J. Mater. Chem. A*, vol. 3, no. 29, pp. 14929–14941, 2015.
- [8] G. Heinrich and T. A. Vilgis, "Contribution of Entanglements to the Mechanical Properties of Carbon Black Filled Polymer Networks," *Macromolecules*, vol. 26, no. 5, pp. 1109–1119, 1993.
- [9] M. Arroyo, M. A. López-Manchado, and B. Herrero, "Organo-montmorillonite as substitute of carbon black in natural rubber compounds," *Polymer (Guildf.)*, vol. 44, no. 8, pp. 2447–2453, 2003.
- [10] M. D. Frogley, D. Ravich, and H. D. Wagner, "Mechanical properties of carbon nanoparticle-reinforced elastomers," *Compos. Sci. Technol.*, vol. 63, no. 11, pp. 1647–1654, 2003.
- [11] A. Okada, A. Usuki, T. Kurauchi, and O. Kamigaito, "Polymer—Clay Hybrids," 1995, pp. 55–65.
- [12] A. N. Gent, *Engineering with Rubber*. Hanser Publishers, 2012.
- [13] K. E. Wise, C. Park, E. J. Siochi, and J. S. Harrison, "Stable dispersion of single wall carbon nanotubes in polyimide: The role of noncovalent interactions," *Chem. Phys.*

- Lett.*, vol. 391, no. 4–6, pp. 207–211, Jun. 2004.
- [14] O. Breuer and U. Sundararaj, “Big returns from small fibers: A review of polymer/carbon nanotube composites,” *Polym. Compos.*, vol. 25, no. 6, pp. 630–645, Dec. 2004.
- [15] M. D’Arienzo *et al.*, “Hybrid SiO₂@POSS nanofiller: a promising reinforcing system for rubber nanocomposites,” *Mater. Chem. Front.*, vol. 1, no. 7, pp. 1441–1452, Jun. 2017.
- [16] G. P. Baeza *et al.*, “Effect of Grafting on Rheology and Structure of a Simplified Industrial Nanocomposite Silica/SBR,” *Macromolecules*, vol. 46, no. 16, pp. 6621–6633, Aug. 2013.
- [17] I. Mora-Barrantes, L. Ibarra, A. Rodriguez, L. Gonzalez, and J. L. Valentin, “Elastomer composites based on improved fumed silica and carbon black. Advantages of mixed reinforcing systems,” *J. Mater. Chem.*, vol. 21, no. 43, pp. 17526–17533, 2011.
- [18] J. Schlomach and M. Kind, “Investigations on the semi-batch precipitation of silica,” *J. Colloid Interface Sci.*, vol. 277, no. 2, pp. 316–326, Sep. 2004.
- [19] E. A. Gorrepati, P. Wongthahan, S. Raha, and H. S. Fogler, “Silica Precipitation in Acidic Solutions: Mechanism, pH Effect, and Salt Effect,” *Langmuir*, vol. 26, no. 13, pp. 10467–10474, Jul. 2010.
- [20] M.-H. Yeh and W.-S. Hwang, “High Mechanical Properties of Polychloroprene/Montmorillonite Nanocomposites,” *Mater. Trans.*, vol. 47, no. 11, pp. 2753–2758, 2006.
- [21] C. Zha, W. Wang, Y. Lu, and L. Zhang, “Constructing covalent interface in rubber/clay nanocomposite by combining structural modification and interlamellar silylation of montmorillonite,” *ACS Appl. Mater. Interfaces*, vol. 6, no. 21, pp. 18769–18779, 2014.
- [22] B. Velde, *Clay Minerals: A Physio-Chemical Explanation of their Occurrence*. Elsevier, 1985.
- [23] M. Alexandre and P. Dubois, “Polymer-layered silicate nanocomposites: preparation, properties and uses of a new class of materials,” *Mater. Sci. Eng. R Reports*, vol. 28, no. 1–2, pp. 1–63, Jun. 2000.
- [24] M. Galimberti, *Rubber-Clay Nanocomposites : Science, Technology, and Applications*.

- John Wiley & Sons, 2011.
- [25] J. Bottazzo, "Rubber compounds for industrial applications," 2012.
- [26] H. Van Olphen, *An introduction to clay colloid chemistry : for clay technologists, geologists, and soil scientists*. Wiley, 1977.
- [27] J. Santaren, J. Sanz, E. Ruiz-hitzky, and I. D. C. De Materiales, "Structural fluorine in sepiolite," *Clays Clay Miner.*, vol. 38, no. 1, pp. 63–68, 1990.
- [28] M. Kotal and A. K. Bhowmick, "Polymer nanocomposites from modified clays: Recent advances and challenges," *Prog. Polym. Sci.*, vol. 51, pp. 127–187, 2015.
- [29] A. Esteban-Cubillo, R. Pina-Zapardiel, J. S. Moya, M. F. Barba, and C. Pecharromán, "The role of magnesium on the stability of crystalline sepiolite structure," *J. Eur. Ceram. Soc.*, vol. 28, no. 9, pp. 1763–1768, 2008.
- [30] L. G. Hernandez, L. I. Rueda, and A. R. Diaz, "Preparation of Silica by Acid Dissolution of Sepiolite and Study of its Reinforcing Effect in Elastomers," vol. 103, no. 1579, pp. 51–60, 1982.
- [31] C. Fernandez-Barranco, A. E. Koziół, K. Skrzypiec, M. Rawski, M. Drewniak, and A. Yebra-Rodriguez, "Study of spatial distribution of sepiolite in sepiolite/polyamide6,6 nanocomposites," *Appl. Clay Sci.*, vol. 127–128, pp. 129–133, 2016.
- [32] E. Ruiz-Hitzky, P. Aranda, M. Darder, and G. Rytwo, "Hybrid materials based on clays for environmental and biomedical applications," *J. Mater. Chem.*, vol. 20, no. 42, p. 9306, 2010.
- [33] E. Galan, "Advances in the crystal chemistry of sepiolite and palygorskite," in *Developments in Clay Science*, Singer, 2011, pp. 281–298.
- [34] J. A. de Lima, F. F. Camilo, R. Faez, and S. A. Cruz, "A new approach to sepiolite dispersion by treatment with ionic liquids," *Appl. Clay Sci.*, vol. 143, no. April, pp. 234–240, 2017.
- [35] N. García *et al.*, "Surface modification of sepiolite in aqueous gels by using methoxysilanes and its impact on the nanofiber dispersion ability," *Langmuir*, vol. 27, no. 7, pp. 3952–3959, 2011.
- [36] A. Mejía, N. García, J. Guzmán, and P. Tiemblo, "Surface modification of sepiolite nanofibers with PEG based compounds to prepare polymer electrolytes," *Appl. Clay Sci.*, vol. 95, pp. 265–274, 2014.

- [37] J. Y. Ko, K. Prakashan, and J. K. Kim, "New silane coupling agents for silica tire tread compounds," *J. Elastomers Plast.*, vol. 44, no. 6, pp. 549–562, 2012.
- [38] L. Wahba *et al.*, "In situ sol–gel obtained silica–rubber nanocomposites: influence of the filler precursors on the improvement of the mechanical properties," *RSC Adv.*, vol. 3, no. 17, p. 5832, Apr. 2013.
- [39] R. Scotti *et al.*, "Rubber–silica nanocomposites obtained by in situ sol–gel method: particle shape influence on the filler–filler and filler–rubber interactions," *Soft Matter*, vol. 8, no. 7, p. 2131, Jan. 2012.
- [40] A. Romo-Uribe, P. T. Mather, T. S. Haddad, and J. D. Lichtenhan, "Viscoelastic and morphological behavior of hybrid styryl-based polyhedral oligomeric silsesquioxane (POSS) copolymers," *J. Polym. Sci. Part B Polym. Phys.*, vol. 36, no. 11, pp. 1857–1872, Aug. 1998.
- [41] I. Mora-Barrantes, L. Ibarra, A. Rodriguez, L. Gonzalez, and J. L. Valentin, "Elastomer composites based on improved fumed silica and carbon black. Advantages of mixed reinforcing systems," *J. Mater. Chem.*, vol. 21, no. 43, pp. 17526–17533, Oct. 2011.
- [42] J. Ramier, L. Chazeau, C. Gauthier, L. Guy, and M. N. Bouchereau, "Grafting of silica during the processing of silica-filled SBR: Comparison between length and content of the silane," *J. Polym. Sci. Part B Polym. Phys.*, vol. 44, no. 1, pp. 143–152, Jan. 2006.
- [43] H. Ishida, *Molecular Characterization of Composite Interfaces*, 1st ed. Boston, MA: Springer US, 1985.
- [44] I. Mora-Barrantes, A. Rodriguez, L. Ibarra, L. Gonzalez, and J. L. Valentin, "Overcoming the disadvantages of fumed silica as filler in elastomer composites," *J. Mater. Chem.*, vol. 21, no. 20, pp. 7381–7392, 2011.
- [45] J. W. ten Brinke, S. C. Debnath, L. A. E. M. Reuvekamp, and J. W. M. Noordermeer, "Mechanistic aspects of the role of coupling agents in silica-rubber composites," *Compos. Sci. Technol.*, vol. 63, no. 8, pp. 1165–1174, 2003.
- [46] H.-D. Luginsland, J. Fröhlich, and A. Wehmeier, "Influence of Different Silanes on the Reinforcement of Silica-Filled Rubber Compounds," *Rubber Chem. Technol.*, vol. 75, no. 4, pp. 563–579, 2002.
- [47] P. Vondracek, M. Hradec, V. Chvalovsky, and H. D. Khanh, "The Effect of the Structure of Sulfur-Containing Silane Coupling Agents on Their Activity in Silica-Filled SBR," *Rubber Chemistry and Technology*, vol. 57. pp. 675–685, 1984.

- [48] L. R. Avila *et al.*, “New synthesis strategies for effective functionalization of kaolinite and saponite with silylating agents,” *J. Colloid Interface Sci.*, vol. 341, no. 1, pp. 186–193, Jan. 2010.
- [49] S. Rooj, A. Das, V. Thakur, R. N. Mahaling, A. K. Bhowmick, and G. Heinrich, “Preparation and properties of natural nanocomposites based on natural rubber and naturally occurring halloysite nanotubes,” *Mater. Des.*, vol. 31, no. 4, pp. 2151–2156, 2010.
- [50] S. qin Yang *et al.*, “Effect of reaction temperature on grafting of γ -aminopropyl triethoxysilane (APTES) onto kaolinite,” *Appl. Clay Sci.*, vol. 62–63, pp. 8–14, 2012.
- [51] V. S. Raman *et al.*, “Reinforcement of solution styrene butadiene rubber by silane functionalized halloysite nanotubes,” *J. Macromol. Sci. Part A Pure Appl. Chem.*, vol. 50, no. 11, pp. 1091–1106, 2013.
- [52] N. Takahashi and K. Kuroda, “Materials design of layered silicates through covalent modification of interlayer surfaces,” *J. Mater. Chem.*, vol. 21, no. 38, p. 14336, 2011.
- [53] S. Sánchez-Valdes *et al.*, “Effect of PEGMA/amine silane compatibilizer on clay dispersion of polyethylene-clay nanocomposites,” *Polym. Bull.*, vol. 63, no. 6, pp. 921–933, Dec. 2009.
- [54] S. R. Ha, S. H. Ryu, S. J. Park, and K. Y. Rhee, “Effect of clay surface modification and concentration on the tensile performance of clay/epoxy nanocomposites,” *Mater. Sci. Eng. A*, vol. 448, no. 1–2, pp. 264–268, Mar. 2007.
- [55] A. M. Shanmugaraj, K. Y. Rhee, and S. H. Ryu, “Influence of dispersing medium on grafting of aminopropyltriethoxysilane in swelling clay materials,” *J. Colloid Interface Sci.*, vol. 298, no. 2, pp. 854–859, Jun. 2006.
- [56] C.-W. Nan, Y. Shen, and J. Ma, “Physical Properties of Composites Near Percolation,” *Annu. Rev. Mater. Res.*, vol. 40, no. 1, pp. 131–151, 2010.
- [57] H. Mollet and A. Grubermann, *Formulation Technology*. Weinheim, Germany: Wiley-VCH Verlag GmbH, 2001.
- [58] J. Y. Yi and G. M. Choi, “Percolation Behavior of Conductor-Insulator Composites with Varying Aspect Ratio of Conductive Fiber,” *J. Electroceramics*, vol. 3, no. 4, pp. 361–369, 1999.
- [59] K. Yurekli, R. Krishnamoorti, M. F. Tse, K. O. McElrath, A. H. Tsou, and H. C. Wang, “Structure and dynamics of carbon black-filled elastomers,” *J. Polym. Sci. Part*

- B Polym. Phys.*, vol. 39, no. 2, pp. 256–275, 2001.
- [60] L. Giannini *et al.*, “A Rubber Vision of High Aspect Ratio Nanofillers. International Rubber Conference.” Paris, 2013.
- [61] T. Sabu and R. Stephen, *Rubber Nanocomposites. Preparation, properties, and applications*. John Wiley & Sons, 2010.
- [62] A. R. Payne and G. Kraus, *Reinforcement of elastomers*, vol. 69. New York, 1965.
- [63] A. I. Medalia, “Effect of Carbon Black on Dynamic Properties of Rubber Vulcanizates,” *Rubber Chemistry and Technology*, vol. 51, no. 3. pp. 437–523, 1978.
- [64] G. Tsagaropoulos and A. Eisenberg, “Dynamic Mechanical Study of the Factors Affecting the Two Glass Transition Behavior of Filled Polymers. Similarities and Differences with Random Ionomers,” *Macromolecules*, vol. 28, no. 18, pp. 6067–6077, 1995.
- [65] G. Tsagaropoulos and A. Eisenberg, “Direct Observation of Two Glass Transition in Silica-Filled Polymers. Implications for the Morphology of Random Ionomers,” *Macromolecules*, vol. 28, no. 1, pp. 396–398, 1995.
- [66] V. Arrighi, I. . McEwen, H. Qian, and M. . Serrano Prieto, “The glass transition and interfacial layer in styrene-butadiene rubber containing silica nanofiller,” *Polymer (Guildf)*, vol. 44, no. 20, pp. 6259–6266, 2003.
- [67] C. G. Robertson, C. J. Lin, M. Rackaitis, and C. M. Roland, “Influence of particle size and polymer– filler coupling on viscoelastic glass transition of particle-reinforced polymers,” *Macromolecules*, vol. 41, pp. 2727–2731, 2008.
- [68] L. Tadiello *et al.*, “The filler-rubber interface in styrene butadiene nanocomposites with anisotropic silica particles: morphology and dynamic properties,” *Soft Matter*, vol. 11, p. , 2015.
- [69] J. Berriot, H. Montes, F. Lequeux, D. Long, and P. Sotta, “Evidence for the shift of the glass transition near the particles in silica-filled elastomers,” *Macromolecules*, vol. 35, no. 26, pp. 9756–9762, 2002.
- [70] Y. Fukahori, “New progress in the theory and model of carbon black reinforcement of elastomers,” *J. Appl. Polym. Sci.*, vol. 95, no. 1, pp. 60–67, 2005.
- [71] T. a Vilgis, G. Heinrich, and M. Kluepell, *Reinforcement of Polymer Nano-Composites: Theory, Experiments and Applications*. Cambridge University Press, 2009.

-
- [72] M. Klüppel, R. H. Schuster, and G. Heinrich, "Structure and Properties of Reinforcing Fractal Filler Networks in Elastomers," *Rubber Chem. Technol.*, vol. 70, no. 2, pp. 243–255, 1997.
- [73] J.-B. Donnet and E. Custodero, "Reinforcement of Elastomers by Particulate Fillers," in *Science and Technology of Rubber*, Elsevier, 2005, pp. 367–400.
- [74] R. Scotti *et al.*, "Shape controlled spherical (0D) and rod-like (1D) silica nanoparticles in silica/styrene butadiene rubber nanocomposites: Role of the particle morphology on the filler reinforcing effect," *Polym. (United Kingdom)*, vol. 55, no. 6, pp. 1497–1506, Mar. 2014.
- [75] P. C. Lebaron, Z. Wang, and T. J. Pinnavaia, "Polymer-layered silicate nanocomposites: An overview," *Appl. Clay Sci.*, vol. 15, no. 1–2, pp. 11–29, 1999.
- [76] S. Sinha Ray and M. Okamoto, "Polymer/layered silicate nanocomposites: A review from preparation to processing," *Prog. Polym. Sci.*, vol. 28, no. 11, pp. 1539–1641, 2003.
- [77] E. Ruiz-Hitzky and A. Van Meerbeek, "Chapter 10.3 Clay Mineral- and Organoclay-Polymer Nanocomposite," *Dev. Clay Sci.*, vol. 1, no. C, pp. 583–621, Jan. 2006.
- [78] L. Hernández, González, L. I. Rueda, and C. Chamorro Antón, "Magnesium Silicate Filler in Rubber Tread Compounds.pdf," *Rubber Chem. Technol.*, vol. 60, no. 4, pp. 606–617, 1987.
- [79] N. M. Nahmias, L. Giannini, and A. Lostritto, "High-performance tyre for motor vehicle wheels," WO 2012164436 A1, 2012.

2

Materials, Procedures & Methods of Characterization

This chapter describes materials and their procedures of preparation used in this thesis. A complete description of the materials and their use will be given together with the procedures of modification and preparation methods used. Finally, methods used for the full characterization of the new materials will be described.

2.1 Materials

The list of these materials employed for rubber compounding is usually referred as formulation. The Table 2.1 is a generic composition of an individual tire compound [1]. The unit of measurement used for the quantities by weight of the various constituents of the recipe is phr (parts per hundred rubber), which indicates the quantity of additive required per 100 parts of rubber.

Table 2.1 General tire formulation

Ingredient	phr
Rubber	100
Filler	50
Softener	5
Antioxidant	1
Stearic acid	1
Zinc oxide	5
Accelerator	1
Sulphur	2
Total	165

A rubber formulation consists mainly on a single polymer or the mixture (*blend*) of two or more polymers for getting unique properties in the final rubber materials. Besides polymer, the compound has many different components, as reported in Table 2.1, with specific roles to play. Tire compound are made from materials such as natural rubber and/or synthetic rubbers, chemicals which function as antidegradants, curatives, processing aids and reinforcing fillers. These materials are selected according to their physico-chemical properties and their interactions with other constituent materials to provide a broad range of mechanical properties. Individual compounds are designed and formulated to

meet the specific set performance requirements of the tire component [1]–[4]. This is primarily accomplished through selection of elastomer type(s), selection of chemicals for vulcanization, selection of materials for facile processing and tire manufacturing, and selection of materials for in-service performance.

The compound ingredients can be classified on the basis of their specific functions:

- Fillers - CB, Silica, LS
- Softeners – processing aids, plasticizers, extenders
- Antidegradants – antioxidant, antiozonants, age resisters, protective waxes
- Vulcanizing & Curing – vulcanizing agents, accelerators, activators.

2.1.1 Rubber

Base polymer (raw elastomer, gum rubber) is the main ingredient of rubber materials and can consist of natural or synthetic rubber, or thermoplastic elastomers. Typical rubbers are amorphous polymers with high molecular weight ($M_n > 10^5$), having a random coil arrangement and show a low glass transition and high viscosity.

The characteristic common to all elastomeric substances is therefore the presence of long polymer chains interconnected by cross-links. The chains, which are normally folded in the non-deformed state, change their spatial distribution under the effect of an external force, aligning themselves parallel to the direction of the elongation. The appearance of a retraction force in the deformed rubber, having the same direction but opposite to the deforming force, is directly connected to the natural tendency of the macromolecules to return to their original conformations. As the deformation of the material and the consequent lengthening of the macromolecules continue the number of

accessible isoenergetic conformations diminishes, until there is only one conformation for every completely extended chain.

After the removal of the external force causing the deformation, each polymer chain recovers its original shape, which corresponds to the state characterized by a majority of the isoenergetic conformations. Therefore, the emerging retractive force (*elastic recovery*) results from the natural tendency of the system to increase its own entropy up to the maximum value that it possesses in the non-deformed state.

The elastomers used in this thesis were the followings: isoprene rubber (IR), styrene-butadiene rubber (SBR), and butadiene rubber (BR), below briefly described.

Natural Rubber (NR) is the most widely used polymer, literature is full of composite based on this rubber [5]–[8]. It is composed from 1,4 polyisoprene in the *cis* and *trans* configurations (Fig 2.1).

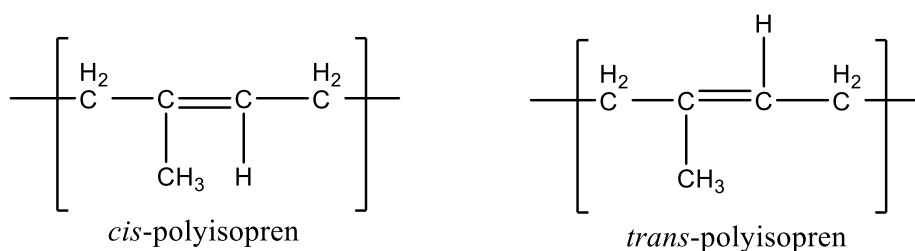


Figure 2.1 *Cis* and *trans* configurations of NR

The importance of NR elastomer, especially in industrial application, is associated with the discovery of the sulfur-based vulcanization process, that causes the formation of bonds between the macromolecules and leads to important physical variations of the elastomer introducing mechanical properties that are technologically useful [9], [10].

NR plays an important role in the tire industry market because of its unique properties that make it irreplaceable in the manufacture of the carcasses and sidewalls of the tire themselves. Maintaining adhesion between the carcass, the belt and the other parts of the tire, especially in the areas that are subjected to the greatest increases in temperature, is guaranteed by compounds in which the quantity of NR is at least 30% for cars and 50-100% for heavy vehicles.

IR is a *synthetic polymer* obtained from polymerization of isoprene with properties similar to those of NR.

Isoprene molecule can react in several ways to form the structural unit 1,4-cis, the 1,4-trans and two units, 1,2 and 3,4. Since the addition of 1,2 and 3,4 causes the formation of a chiral carbon, it would be possible for each of the above-mentioned units to prepare three different IR: isotactic, syndiotactic, atactic. Among the eight possible pure structures, only 1,4-cis, the 1,4-trans and the 3,4 atactic can be synthesized.

There are various types of synthetic IR containing various quantities of the above-mentioned four units linked together in a random way. There are two synthetic processes for obtaining IR with a high isomeric purity: anionic and metal coordinated polymerization developed by Shell Oil and Goodyear Tire & Rubber. Among the various types, IR 1,4-cis is by far the most important for the elastic and mechanical properties that it imparts to the vulcanizates; these properties come from the high degree of isomeric purity of the material, which, in the case of NR is higher than 99% in terms of 1,4-cis. IR, synthesized with Ziegler-Natta catalysts, exhibits properties exactly like those of NR, even if inferior in terms of isomeric purity and cost of production.

Other synthetic polymers can be used in tire formulation as partial substituting or completely replacing NR and IR. The most important are SBR and PB (Fig. 2.2).

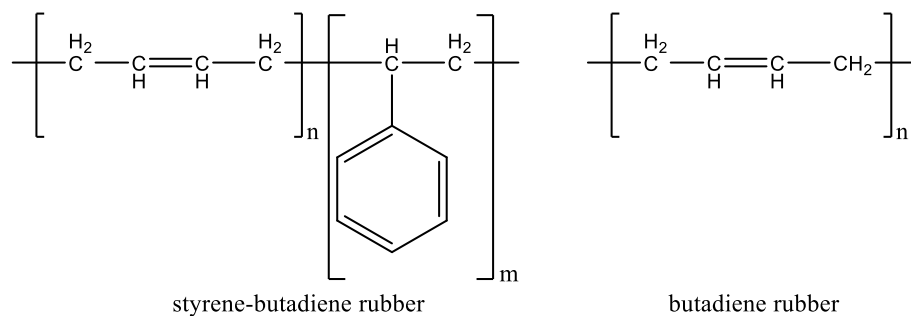


Figure 2.2 Chemical structure of SBR and BR rubber

SBR is a non-polar copolymer of styrene and butadiene. SBR can be synthesized by cold emulsion technology and designed as E-SBR or in solution through anionic polymerization and designed as S-SBR.

SBR are principally used in the manufacture of tire treads in a blend with PB and/or NR. SBR properties are influenced from the ratio of the two copolymers. In general, higher is the amount of styrene harder the polymer is. Some of the properties, such as strength, heat build-up and stickiness are inferior of the NR, but SBR shows higher abrasion and degradation resistance.

PB is the product of polymerization of butadiene, the raw material of various synthetic rubbers. Butadiene polymerizes with a chain addition mechanism, 1,2 or 1,4-polymerization. Since 1,2 polymerization produces the formation of a chiral carbon, three types of vinyl structures are possible: isotactic, syndiotactic and atactic.

Depending on the quantity of 1,4-cis units, two grades of PB are distinguished, namely low-cis and high-cis, that can be prepared through anionic and metal-coordinated polymerization respectively. High-cis PB is a soft and soluble material with excellent dynamic characteristics, low hysteresis and good resistance to abrasion. The high melting temperature of trans PB precludes its use as an elastomer.

BR-based vulcanizates possess superior characteristics to those of NR and SBR in terms of abrasion resistance, flexibility at low temperature, resistance at high temperature, resilience at low deformations and resistance to ozone.

In comparison with NR and SBR, BR-based vulcanizates can incorporate high quantities of oil and fillers without reduction in their properties.

In this thesis, high-cis BR was Europrene 40 from Versalis; synthetic IR was SKI3 from produced by Nitzhnekamsk; SBR was SLR 4630 from Styron Europe GmbH (25% styrene; 63% vinyl; 12% butadiene)

2.1.2 Fillers

Pristine Sep, namely sepiolite Pangel S9 (SepS9) is a commercially available clay and was used as filler (see Chapter 1) in the preparation of rubber composites. SepS9, used in this thesis, was extracted from the landfill of Vallecas (Spain).

Sep Pangel B5 is a organically modified Sep, produced in order to have a better dispersion and compatibility with hydrophobic matrix. Specifically SepB5 is a Sep modified with N,N-didodecyl-N-methyl-ammonium (DDMA), as reported in Fig. 2.3). SepB5 used in this work were supplied by Tolsa and derived from SepS9 extracted from the landfill of Vallecas (Spain). The description of the chemical nature and of the microstructure of Sep fibers is reported in Paragraph 1.2.1.1 of Chapter 1.

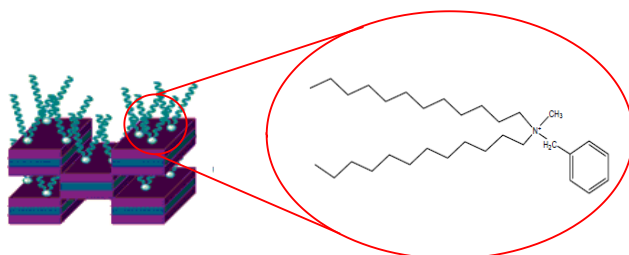


Figure 2.3 Schematic representation of SepB5 and the chemical structure of DDMA

Silica, used in this thesis to prepare SBR nanocomposites and in technical composition (TC) materials by melt mixing, was a commercial Zeosil MP1165 with BET specific surface area $160 \text{ m}^2\text{g}^{-1}$ from Solvay.

In addition colloidal silica, namely LUDOX[®] SM-30 from Sigma-Aldrich, were used to prepare rubber composites from solution mixing. Colloidal silica consists of spherical NPs dispersed in water (30% w/w). In particular HS-30 sample presents an average of spherical diameter of 18 nm.

Also carbon black, the most important reinforcing filler, was used in TC materials: Carbon Black N550, purchased by Cabot.

2.1.3 Silane coupling agent

Coupling agents have a fundamental role in the preparation of rubber composites (see Paragraph 1.5.1 of Chapter 1) to favors the filler dispersion and improve filler/rubber interactions.

In this thesis, bis (3-triethoxysilylpropyl)tetrasulfide (TESPT) [11] and N1-(3-trimethoxysilylpropyl) diethylenetriamine were used and purchased from Aldrich.

2.1.4 Curing agent and additives

The curing agents and additives, used in SBR composites from melt mixing, are the followings: Treated Distillate Aromatic Extract (TDAE) extender oil (37.5 phr); N-(1,3-dimethylbutyl)-N'-phenyl-p-phenylenediamine (6PPD) used as antidegradant was Santoflex-6PPD from Flexsys; stearic acid was Stearina TP8 from Undesa; sulfur was from Zolfoindustria; zinc oxide was from Zincol Ossidi; N-cyclohexyl-2-benzothiazole sulfenamide (CBS) was Vulkacit CZ/C from Lanxess; N-tert-butyl-2-benzothiazyl sulfenamide.

In addition, for TC materials, the following ingredients were used: N-tert-butyl-2-benzothiazyl sulfenamide (TBBS) from Lanxess; polymerized 2,2,4-trimethyl-1,2-dihydroquinoline (TMQ) was from General Quimica S.A.

2.2 Procedures

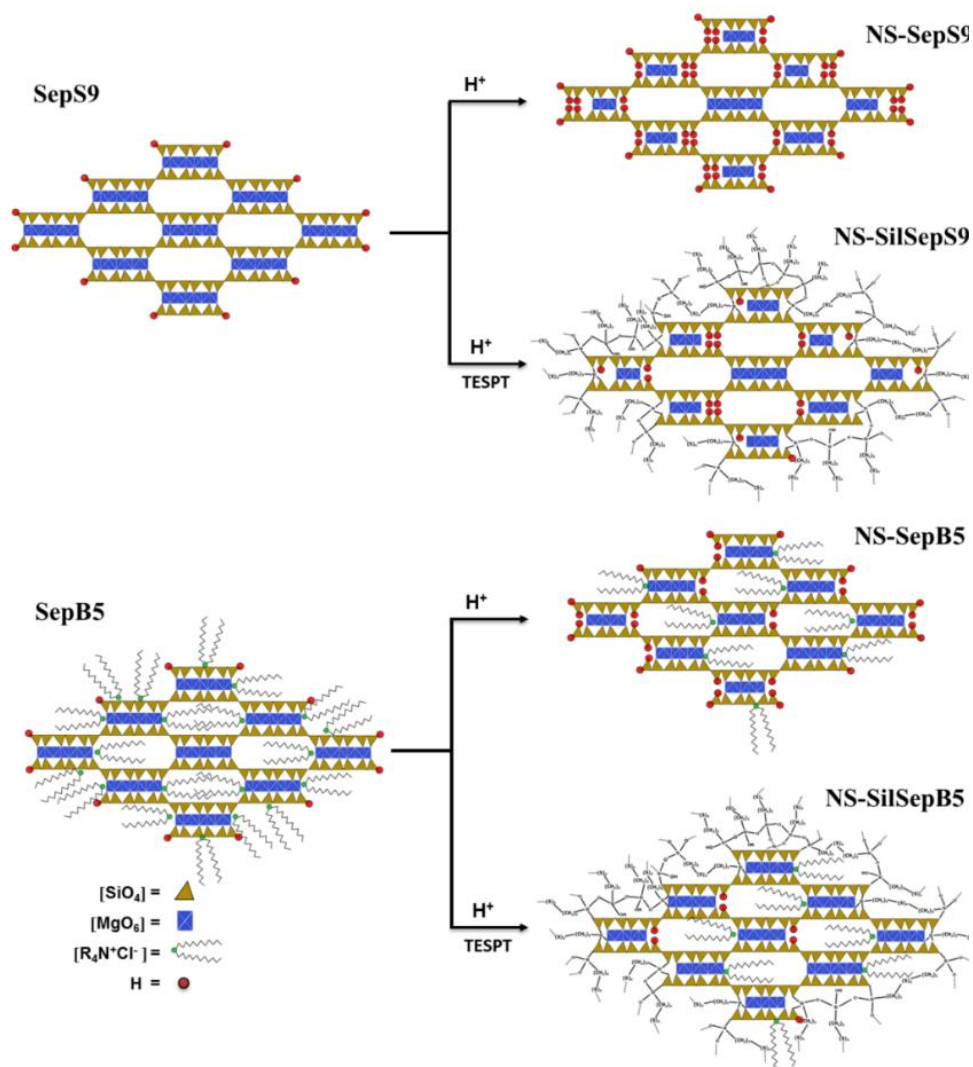
The incorporation of pristine Sep in rubber nanocomposites is affected by surface hydrophilicity surface and consequent low affinity towards organic matrix. Also, SepB5, organically-modified with alkyl ammonium groups, presents better ability to disperse in a polymer matrix, but modest polymer-filler interaction, as reported by Nohales et al.[12]. Meanwhile, surface treatment *via* silane coupling agent is poorly effective, consisting only in 10% of functionalized Sep [13], due to the low bonding sites number. To avoid these problems and make Sep fibers more suitable as reinforcing filler, the surface modification of Sep fibers is mandatory. This thesis proposes two different approaches:

1. *the acid treatment of Sep fibers to prepare rubber composites by melt-mixing)*
2. *the functionalization of Sep fibers with ionizable group to prepare rubber composites by solution mixing*

2.2.1 Acid filler treatment approach

A controlled surface acid treatment on bare Sep was applied, moving from literature methods [14]–[17]. This treatment NS-Sep preserving the filler anisotropic features and increasing the amount of bonding sites at the Sep edge surfaces.

The simultaneous silanization of Sep surface, during acid treatment, was also investigated by using TESPT silane (Scheme 2.1).



Scheme 2.1 Experimental procedure for acid treatment and for one-pot procedure of (a) SepS9 and (b) SepB5. The SepX structural representation consists of two tetrahedral silica sheets and a central octahedral Mg sheet. In evidence, the partial extraction of structural Mg^{2+} from the octahedral sheet, the increase of silanol groups on the sepiolite surface and the TESPT silanization on the sepiolite surface.

2.2.1.1 Acid treatment of SepS9 and SepB5

SepX (with X = S9 or B5, 120.0 g) was suspended in iPr-OH (1.2 L) at 65 °C and vigorously stirred (800 revolutions per minute (rpm)) for 30 min. Then 37% aqueous HCl solution (480 mL) was added to the reaction mixture. The reaction mixture was stirred at 65 °C (600 rpm) for 2 h, and then filtered. The resulting solid was washed repeatedly with deionized water and with aqueous ammonium hydroxide (60%) until pH 7 ± 0.2 . Finally, the powder was filtered, washed again with water (until no chloride anions were detected by AgCl precipitation) and dried in an oven at 120 °C for 48 h. The obtained product was labeled NS-SepX. Scheme 2.1 (synthetic pathway with H⁺) illustrates the changes in the SepX structure after the above described acid treatment.

2.2.1.2 One-pot procedure for acid treatment/silanization SepS9 and SepB5

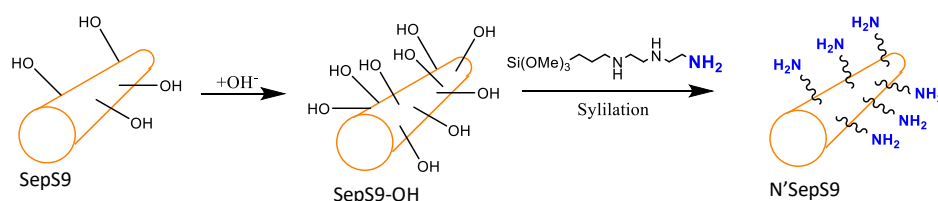
Functionalized Sep fibers, labeled NS-SilSepX, were prepared simultaneously to the acid treatment by using TESPT as silane coupling agent (synthetic pathway with H⁺/TESPT in Scheme 1). TESPT (64.7 g) was added to the HCl mixture containing SepX (120.0 g). The reaction conditions and workup procedure were the same as those reported above (Paragraph 2.2.1.1).

2.2.2 Ionic functionalization of SepS9

A different approach on promoting the Sep-rubber interaction was explored by an ionic interaction between filler-rubber. This requires the introduction of ionic groups in both Sep fillers and SBR polymer chains. To this aim, a simple ionic functionalization of Sep was applied. Firstly, a basic treatment was used for increasing the number of hydroxyl groups by maintaining the shape and AR of the particles. Meanwhile the SBR matrix was functionalized with sulfonate group.

2.2.2.1 Basic treatment and functionalization of SepS9 with amino silane

SepS9 (4 g) was dispersed in 300 ml of deionized water in a 500 ml three neck flask. Subsequently NaOH (0.116 mg) was added in the Sep dispersion and let to react under stirring at room temperature (r.t.) for 24 h. The obtained hydroxylated SepS9, namely SepS9-OH was then separated by centrifugation at 9000 rpm for 30 min. and washed with deionized water until pH reached 7. Finally, SepS9-OH was dried at 120 °C for 24 h. SepS9-OH (3 g) was dispersed in 400 ml of deionized water and ultrasonicated for 10 min. Then N1-(3-trimethoxysilylpropyl) diethylenetriamine (6 g) was added dropwise. The obtained mixture was heated at 70 °C under stirring for 24 h. After that, the suspension was cooled at r.t. and transferred in a SnakeSkin dialysis tubing (10k MWCO, Pierce) and dialyzed against deionized water for 72 h while changing the water twice a day. The obtained product was labeled N'SepS9. Scheme 2.2 illustrates the changes in SepS9 after the above described approach.



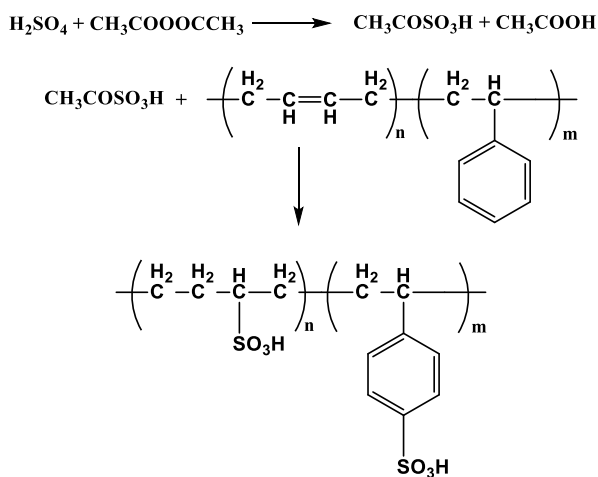
Scheme 2.2 Schematic representation of functionalization of SepS9 with amino silane

2.2.2.2 Synthesis of sulfonated SBR

The preparation of sulfonated SBR was adapted from a procedure set up reported by Willis and Pottick [18].

Firstly, the sulfonating reagent acetyl sulfate was prepared by reaction of concentrated sulfuric acid and acetic anhydride, as reported in Scheme 2.3. Previously acetic anhydride (7.63 ml) was diluted in dichloromethane (39.6 ml).

Then the solution was cooled to 0 °C and H₂SO₄ 95% was added (2.8 ml). By considering the reaction yield quantitative, a solution of acetyl sulfate 1M was obtained.



Scheme 2.3 Chemical reactions for the preparation of sulfonated SBR

In the second step, block copolymer SBR (15.0 g) was dissolved in dichloromethane (300 ml). After purged with nitrogen for 30 min., the solution was heated at 55 °C to favor the SBR dissolution. Acetyl sulfate (2 ml) was diluted in 50 ml of dichloromethane, previously cooled down to 0 °C, and added dropwise to SBR solution. The obtained solution was stirred for 2 h at 55 °C, after which the reaction was stopped by adding 20 ml of *i*-PrOH. The functionalized polymer was isolated by precipitating it in methanol (500 ml), filtered and washed with water, ethanol and vacuum dried at r.t. for 24 h.

2.2.3 Preparation of Sep/SBR nanocomposites by melt mixing

SepX, NS-SepX and NS-SilSepX were used to prepare SBR nanocomposite and TC materials. SBR nanocomposites were prepared by blending technique in a Brabender Plasti-Corder Lab (Fig. 2.4) station internal mixer (65 mL mixing

chamber, 0.6 filling factor). Meanwhile TC materials were prepared by an internal tangential rotor mixer, namely Banbury[®].

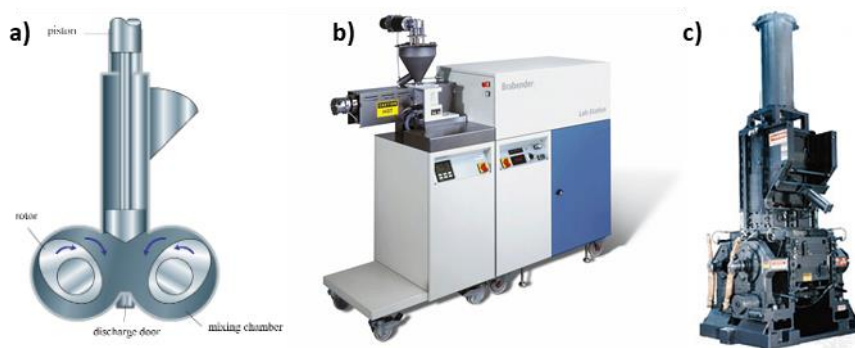


Figure 2.4 Schematic representation of (a) the internal chamber of a mixer, (b) the Brabender and (c) Banbury

All the materials of a typical formulation are thermos-mechanically mixed in a closed chamber. During the mixing, several processes start to take place: adsorption of the polymer and additives in to the surface, destruction of the aggregates and incorporation of polymer chains in to the voids of the filler structure.

In order to have a homogeneous blend three physical mixing process should happen:

- Laminar mixing
- Distributive mixing
- Intensive or dispersive mixing

The mixing process start with the deformation of the rubber matrix that helps the distribution of the components within the matrix and contemporary breakdown of filler agglomerate in to fine aggregates.

Fillers, rubber, additives and curing agent are introduced in the chamber pushed by a piston and mixed in a temperature controlled environment. This takes place at a high temperature (90-150 °C) which improves the workability of the rubber.

This technique is well-known in the rubber industry and described in various ASTM standards for the preparation of rubber composites (ASTM D 3188, D 3185 1A).

2.2.3.1 Preparation of Sep/SBR nanocomposites

The preparation of Sep/SBR nanocomposites consisted of three mixing steps at different temperatures (140, 90 and 50 °C), according to the thermal stability of the reactants. In the first step, rubber was masticated at 140 °C and 60 rpm rotor speed; then pristine or modified Sep (35 phr) were added in three subsequent aliquots, together with TESPT (2.8 phr). Two minutes after the last filler addition, 6PPD (2 phr), zinc oxide (3.5 phr) and stearic acid (2 phr) were added; this lag time avoids secondary reaction between ZnO and silica silanols. In the second step, the obtained materials were reloaded in the internal mixer operating at 90 °C at 60 rpm. CBS (3 phr) and sulfur (1 phr) were then added and mixed for 2 min. In the last step, the composites were finally processed in a two-rolling mill at 50 °C for 3 min. to improve their homogeneity. Uncured composites are labeled SepX/SBR, NS-SepX/SBR and NS-SilSepX/SBR. The reference material was prepared by using Silica Zeosil 1165 instead of Sep and labeled SiO₂/SBR. Finally, cured composites containing 35 phr of SepX, NS-SepX and NS-SilSepX were obtained, by vulcanization performed in a hydraulic press at 170 °C and 100 bar for 20 min. Vulcanized samples are called respectively V-SepX/SBR, V-NS-SepX/SBR and V-NS-SilSepX/SBR in the following. Cured reference material is called V-SiO₂/SBR.

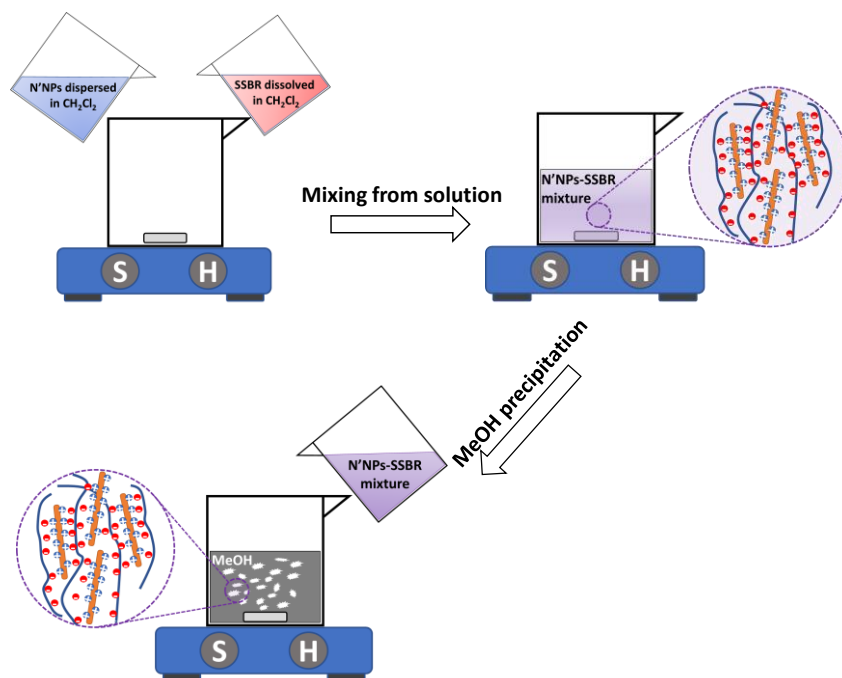
2.2.3.2 Preparation of TC materials

The NS-SepX were incorporated in BR/IR matrix together with conventional silica and carbon black in TC for vulcanisable elastomeric materials. The mixing was conducted in three steps using an internal tangential rotor mixer (banbury): in the first step, BR/IR (60/40 phr), NS-SepX (7 phr), silica (10 phr), carbon

black (35 phr) and TESPT (5 phr) were introduced and the mixing was continued for 5 min, heating up to 135 °C, when the composition was unloaded. After 12 h, in the second step, ZnO (4 phr), stearic acid (1 phr), TMQ (1 phr) and 6-PPD (1.5 phr) were added and mixed for 3 min, up to 125 °C, when the composition was unloaded. After 12 h, in the third step, TBBS (4 phr) and sulphur (2.3 phr) were added and mixed for 2 min, up to 95 °C. These materials, namely V-NS-SepX/TC, were compared with the same elastomeric materials with only silica (20 phr), called V-SiO₂/TC.

2.2.4 Preparation of Sep/SSBR nanocomposites by solution mixing

An alternative to the thermo-mechanical mixing is the preparation of composites from solution, as reported in Scheme 2.4. In this case, fillers are previously dispersed in dichloromethane and successively mixed with a solution of SSBR. N'SepS9(0.45 g) was dispersed in of dichloromethane (30 ml) and sonicated for 30 min. in order to have a good dispersion of the Sep fibers. In the meantime, SSBR (3.0 g) was dissolved in dichloromethane (80 ml). N'SepS9 dispersion was transferred in the SSBR solution and the resulting mixture was stirred at r.t. for 24 h. The obtained polymer composite was isolated by precipitating in methanol (200 ml), filtered and washed with water and ethanol, and vacuum dried at r.t. for 24 h. The sample was labeled N'SepS9-SSBR



Scheme 2.4 Experimental procedure for N'SepS9/SSBR nanocomposites

2.3 Methods of Characterization

2.3.1 Morphological, structural and spectroscopic characterization of fillers

2.3.1.1 Electron microscopy

Scanning Electron Microscopy (SEM) analysis was performed by a Vega TS5136 XM Tescan microscope. The electron beam excitation was 30 kV at a beam current of 25 pA, and the working distance was 12 mm. In this configuration the beam spot was 38 nm sized. Prior to SEM analysis, samples were gold-sputtered.

High Resolution Transmission Electron Microscopy (HR-TEM) was performed on a Jeol 3010 operating at 300 kV with a high-resolution pole piece (0.17 nm

point to point resolution) and equipped with a Gatan slow-scan 794 CCD camera. The powders were suspended in *i*Pr-OH, and a 5 μ L drop of this suspension was deposited on a holey carbon film supported on 3 mm copper grid for TEM investigation (in collaboration with Dr Paola Stagnaro of ISMAC-CNR of Genova).

2.3.1.2 X-Ray Diffraction

The crystal structure of fillers was investigated by X-Ray Diffraction (XRD), recorded in X'Pert Pro PXRD (Panalytical) diffractometer in Bragg-Brentano geometry, using Cu K- α source 1.54 \AA length.

2.3.1.3 Infrared spectroscopy

Chemical surface modification of Sep was studied by Attenuated Total Reflection-Fourier Transform Infrared Spectroscopy (ATR-FTIR), performed on a Perkin Elmer Spectrum 100 instrument (1 cm^{-1} resolution spectra, 650-4000 cm^{-1} region, 16 scans). All the spectra are normalized respect to the most intense peak.

2.3.1.4 Nuclear Magnetic Resonance (NMR)

Sep fillers were also characterized by solid-state NMR (SS-NMR) with a Bruker 400WB spectrometer operating at a proton frequency of 400.13 MHz. Magic Angle Spinning (MAS) NMR spectra were acquired with cross polarization (CP) and single pulse (SP) sequences. CP experiments: ^{13}C frequency 100.48 MHz, $\pi/2$ pulse length 3.5 μs , contact time 2 ms, decoupling length 6.3 μs , recycle delay 5 s, 2k scans. SP sequence: ^{29}Si frequency 79.48 MHz, $\pi/4$ pulse 3.9 μs , recycle delay 100 s, 1k scans; ^1H frequency 400.13 MHz, $\pi/2$ pulse length 5 μs , 16 scans. Samples were packed in 4 mm zirconia rotors, which were spun at 9 kHz under air flow. Adamantane, Q8M8 and EtOH were used as external secondary references. Si units are labeled according to the usual NMR notation: T_n and Q_n represent trifunctional CSiO_3 and tetrafunctional SiO_4 units,

respectively and n is the number of oxo-bridges. (The NMR analysis was performed in collaboration with Prof Sandra Dire' of Trento University)

2.3.1.5 Inductively Coupled Plasma Atomic Emission Spectrometry (ICP-AES)

The fraction of Mg^{2+} cations leached during the acid treatment was determined by ICP-AES, using a PerkinElmer OPTIMA7000 DV spectrophotometer. Acid treatments were carried out in a reaction flask under mechanical stirring as previously described in the Paragraph 2.2. During the acid attack, samples of 5 mL were withdrawn at intervals of 10 min and separated by centrifugation. Thus, the Mg^{2+} content of the supernatant was analyzed.

2.3.2 Morphological, structural and spectroscopic characterization of nanocomposites

The morphological investigation of both uncured and vulcanized composites was carried out by TEM using a Zeiss EM 900 microscope. Ultrathin sections (about 50 nm thick) of composites were obtained with a Leica EM FCS cryo-ultramicrotome, equipped with a diamond knife, by keeping the samples at $-130^{\circ}C$.

In order to investigate how the dynamics of the polymer matrix is affected by the presence of the Sep particles, a low-resolution SS-NMR study, based on measurements of 1H spin spin relaxation times (T_2), was carried out on both the unfilled SBR and SBR/filler composites. A complete characterization of the dynamic properties of the systems under investigation could be achieved combining SE and CPMG experiments. SE was used to refocus the signal from dipolar-coupled protons in rigid domains characterized by very short T_2 (typically on the order of 10-20 μs), which would otherwise decay during the instrumental dead time. On the other hand, CPMG experiments were exploited to accurately measure the intrinsic T_2 relaxation times of the long-decaying

liquid-like components of the FID, which can be affected by non-dynamic contributions, such as magnetic susceptibility of the sample and/or fluctuations and inhomogeneity of the external magnetic field. Low-resolution SS- NMR experiments were carried out on a Stelar PC-NMR spectrometer coupled with a Niumag permanent magnet working at the ^1H Larmor frequency of 20.8 MHz. ^1H Free Induction Decays (FID's) were recorded under on-resonance conditions by means of a Solid Echo (SE) pulse sequence, which allows solid-like components with short T2 to be also detected. A discrete analysis of the FID's was performed using a non-linear least square fitting procedure implemented in the Mathematica® environment. In order to get quantitative data solid echo FID's were recorded at different echo delays in the range 13-31 μs , and the intensities obtained at the different echo delays were extrapolated to a zero delay, assuming a linear trend. The spin-spin relaxation times of the long-decaying, liquid-like components of the FID were accurately determined using a Carr-Purcell-Meiboom-Gill (CPMG) pulse sequence with an echo delay of 13 μs . The CPMG experiments provided relaxation curves, which were fitted to a linear combination of exponential functions. A relaxation delay of 1 s and a number of scans of 200 were always used. The temperature was always in the range 24-26 °C. The 90° pulse duration was 3 μs . (The low field NMR analysis was performed in collaboration with Prof Marco Geppi of Pisa University)

2.3.3 Dynamic-mechanical analysis of nanocomposites

2.3.3.1 Mechanical analysis by Rubber Process Analyzer (RPA) of Sep/SBR Nanocomposites

Curing profiles of uncured composites were obtained with RPA2000 (Alpha Technologies) under the following conditions: $\pm 1^\circ$ oscillation angle, 170°C temperature, 15.65 kPa pressure and 20 min running time. This analysis gave the optimal conditions for the curing of composites.

Specimens for RPA analysis were cut by using a Constant Volume Rubber Sample Cutter (CUTTER 2000, Alpha Technologies); the dimensions were 3.5 cm diameter and ≈ 0.2 cm thickness, the weight 4.5 ± 0.3 g. Two measurements were carried out for each sample, and the average value was reported.

Dynamic-mechanical measurements on nanocomposites were performed with the same rheometer operating in the shear stress mode. For the uncured samples the strain sweep tests were carried out at 70°C and 1 Hz from 2 to 100% of elongation. In the case of cured samples, the strain sweep test was carried out at 70°C and 10 Hz.

The rheological properties of nanocomposites were also evaluated by a Anton Paar rheometer (Rheoplus MCR 501). Rheological tests were carried out at r.t. with a parallel plate probe with a diameter of 10 mm. Samples with a diameter of 10mm and thickness of 0.7 mm were prepared and during measurement were put under 5N of normal force. the strain sweep tests were carried under an oscillation of 1 rad/s, from 0.1 to 100% of shear strain.

2.3.3.2 Dynamic Mechanical Thermal Analysis (DMTA) of Sep/SBR Nanocomposites

Mechanical properties of Sep/SBR nanocomposite were measured using dynamic mechanical analysis (DMA; TA Instruments, Q800) equipped with two clamps in a tensile geometry. The sample dimensions were 15 mm high, 3 mm in width and a thickness of 1.5 mm. To obtain the dynamic storage moduli (E'), loss modulus (E'') and $\tan\delta$ of the nanocomposites as a function of temperature, the samples were set under a preloaded force of 0.1 N and was applied a frequency of 1 Hz using 0.1% of tensile strain, $[L - L_0] / L_0 - 1$, where L_0 is original specimen length and L is ultimate specimen length. The measurement was carried out in the range temperature -40 - 80 °C at 3 °C/min.

2.3.3.3 Tensile Test

In order to measure tensile strength, elastic modulus and elongation at break, tensile test was carried out on a Zwick/Roell model Z010 testing system. The displacement rate applied on the dog bone samples was 10 mm/min at r.t. and the dimensions of dog bone are shown in Fig 2.5

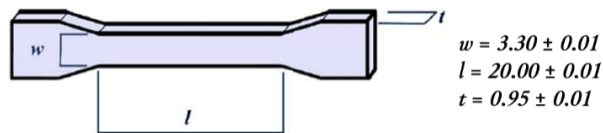


Figure 2.5 Schematization and dimension in mm relative to the samples analyzed in tensile test

2.3.4 Static and dynamic mechanical characterization of TC materials

TC material was vulcanized in order to prepare specimens on which the assessment of static and dynamic mechanical properties was conducted. The static mechanical properties were measured at different elongation (50%, 100% and 300%) the tensile test was carried out on a Dumbell specimens according to the ISO 37:2005 standard.

Dynamic mechanical properties were also evaluated in compression modules using a Instron dynamic device. A TC sample having a cylindrical shape (length = 25 mm and diameter = 14 mm) was preloaded in compression up to a longitudinal strain of 25% and maintained at the predetermined temperature (23 °C or 70 °C) the sample was subjected to a dynamic sinusoidal strain of $\pm 3.5\%$ in amplitude with respect to the length under pre-load at 100 Hz. The dynamic mechanical properties are expressed in terms of dynamic elastic modulus (E'), loss modulus (E'') and $\text{Tan } \delta$ (loss factor).

2.4 Bibliography

- [1] K. Nagdi, *Rubber As an Engineering Material: Guideline for Users*. Hanser Publishers, 1993.
- [2] T. Sabu and R. Stephen, *Rubber Nanocomposites. Preparation, properties, and applications*. John Wiley & Sons, 2010.
- [3] T. Sabu and J. M. Hanna, *Progress in rubber nanocomposites, A volume in Woodhead Publishing Series in Composites Science and Engineering*. 2017.
- [4] S. K. De and J. R. White, *Rubber technologist's handbook*. Rapra Technology Ltd, 2001.
- [5] M. Maiti, M. Bhattacharya, and A. K. Bhowmick, "Elastomer Nanocomposites," *Rubber Chem. Technol.*, vol. 81, no. 3, pp. 384–469, Jul. 2008.
- [6] M. López-Manchado, B. Herrero, and M. Arroyo, "Preparation and characterization of organoclay nanocomposites based on natural rubber," *Polym. Int.*, vol. 52, no. 7, pp. 1070–1077, Jul. 2003.
- [7] S. Varghese and J. Karger-Kocsis, "Melt-compounded natural rubber nanocomposites with pristine and organophilic layered silicates of natural and synthetic origin," *J. Appl. Polym. Sci.*, vol. 91, no. 2, pp. 813–819, Jan. 2004.
- [8] J. Siramanont, V. Tangpasuthadol, A. Intasiri, N. Na-Ranong, and S. Kiatkamjornwong, "Sol-gel process of alkyltriethoxysilane in latex for alkylated silica formation in natural rubber," *Polym. Eng. Sci.*, vol. 49, no. 6, pp. 1099–1106, Jun. 2009.
- [9] M. Akiba and A. S. Hashim, "Vulcanization and crosslinking in elastomers," *Prog. Polym. Sci.*, vol. 22, no. 3, pp. 475–521, Jan. 1997.
- [10] C. Goodyear, "US Patent," 3.633, 1844.
- [11] J. W. ten Brinke, P. J. van Swaaij, L. a. E. M. Reuvekamp, and J. W. M. Noordermeer, "The Influence of Silane Sulfur and Carbon Rank on Processing of a Silica Reinforced Tire Tread Compound," *Rubber Chem. Technol.*, vol. 76, no. 1, pp. 12–35, 2003.
- [12] A. Nohales, R. Muñoz-Espí, P. Félix, and C. M. Gómez, "Sepiolite-reinforced epoxy nanocomposites: Thermal, mechanical, and morphological behavior," *J. Appl. Polym. Sci.*, vol. 119, no. 1, pp. 539–547, 2011.

- [13] N. M. Nahmias, L. Giannini, and A. Lostritto, "High-performance tyre for motor vehicle wheels," WO 2012164436 A1, 2012.
- [14] A. Esteban-Cubillo, R. Pina-Zapardiel, J. S. Moya, M. F. Barba, and C. Pecharromás, "The role of magnesium on the stability of crystalline sepiolite structure," *J. Eur. Ceram. Soc.*, vol. 28, no. 9, pp. 1763–1768, 2008.
- [15] J. L. Valentín, M. A. López-Manchado, A. Rodríguez, P. Posadas, and L. Ibarra, "Novel anhydrous unfolded structure by heating of acid pre-treated sepiolite," *Appl. Clay Sci.*, vol. 36, no. 4, pp. 245–255, 2007.
- [16] A. J. Aznar, J. Sanz, and E. Ruiz-Hitzky, "Mechanism of the grafting of organosilanes on mineral surfaces. IV. Phenyl derivatives of sepiolite and poly (organosiloxanes)," *Colloid Polym. Sci.*, vol. 270, no. 2, pp. 165–176, 1992.
- [17] J. L. Valentín, M. A. López-Manchado, P. Posadas, A. Rodríguez, A. Marcos-Fernández, and L. Ibarra, "Characterization of the reactivity of a silica derived from acid activation of sepiolite with silane by ^{29}Si and ^{13}C solid-state NMR," *J. Colloid Interface Sci.*, vol. 298, no. 2, pp. 794–804, 2006.
- [18] R. A. Weiss, A. Sen, C. L. Willis, and L. A. Pottick, "Block copolymer ionomers: 1. Synthesis and physical properties of sulphonated poly(styrene-ethylene/butylene-styrene)," *Polymer (Guildf.)*, vol. 32, no. 10, pp. 1867–1874, 1991.

3

Sep Rubber Nanocomposites by Melt Mixing: Results and Discussion

This chapter reports the results concerning Sep rubber nanocomposites based on size-controlled Sep nanofibers, obtained by applying a controlled surface treatment on bare Sep.

Firstly, a complete characterization of the modified Sep clays will be reported followed by dynamic-mechanical analysis of clay polymer nanocomposites. Finally, technical nanocomposites will be described in order to verify their possible industrial use as co-filler in tire formulations.

3.1 Modified Sepiolites NS-SepX and NS-SilSepX: chemical structural and characterization

It is well known that the acid treatment of Sep generally leads to partial or total destruction of the magnesium octahedral sheets in the structure, depending on the more or less drastic conditions applied, giving rise to the formation of amorphous silica [1],[2].

The aim of the acid treatment described in in this thesis is to: i) favoring the magnesium extraction but preserving the Sep structure and morphology, ii) increasing the number of reactive silanol groups on the Sep surface, improving the clay interfacial reactivity and iii) decreasing the size of Sep fibers toward the nanometric range, in order to favor their dispersion and to enhance the surface available for interaction with polymer chains. Moreover, the simultaneous functionalization with TESPT allows to obtain ex-situ modified Sep fibers suitable for compatibilization with rubber composites.

3.1.1 Morphological investigation by SEM and TEM analyses

The morphology of the pristine SepX and modified NS-SepX and NS-SilSepX samples were investigated by SEM and TEM analyses. In Fig. 3.1, the SEM micrographs show the characteristic fibrous morphology of SepS9 and SepB5, with fibers strongly interconnected and forming bundles-like aggregates.

In detail, the fibers present needle-like morphology with 20–30 nm diameter, as shown by TEM images in Fig. 3.2) and 1–1.5 μm length on average (SEM images in Fig. 3.1), in agreement with the literature data [3]. SepS9 and SepB5 present the same fiber size, while the way each fiber gathers together to form bigger fibrous structures differs slightly.

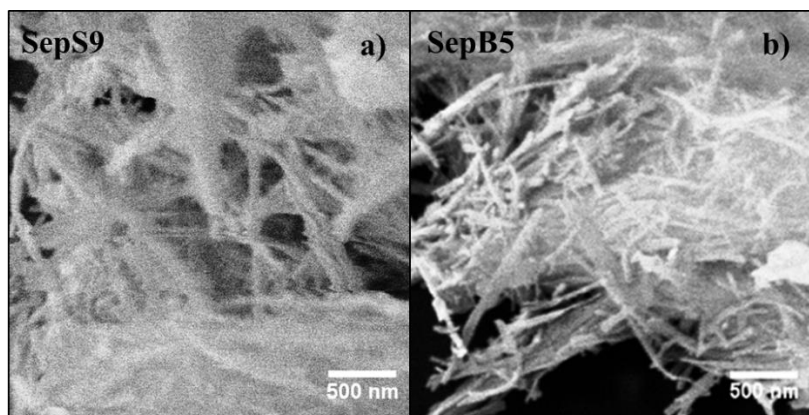


Figure 3.1 SEM micrographs of (a) SepS9 and (d) SepB5.

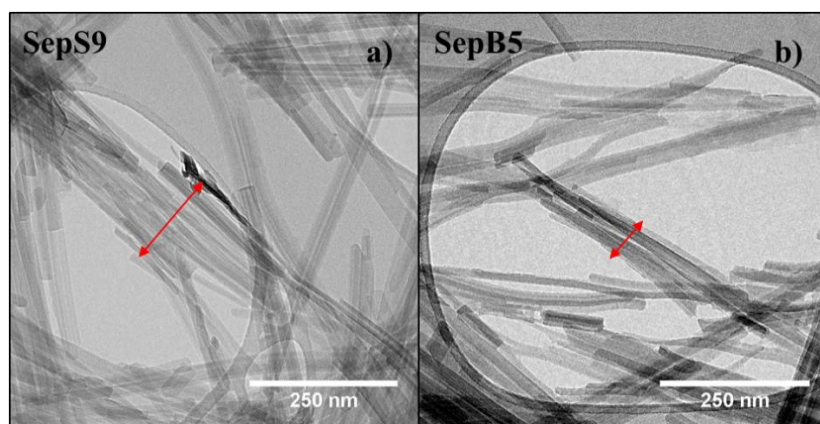


Fig. 3.2 TEM images of (a) SepS9 and (b) SepB5.

After acid treatment, NS-SepX samples (a and b in Fig. 3.3) exhibit significant disaggregation. In details, after drying *in vacuo*, the obtained nanomaterials present aggregates made up of fibers with parallel orientation without tangles, as in SepX. In addition, our treatment produces a significant decrease of the fibers length (see dimensional data reported in Table 3.9 - Paragraph 3.2.3 obtained from composites TEM analysis).

Similar morphological changes were produced by the acid procedure in the presence of TESPT (Fig. 3.3 c and d and Fig. 3.4 a and b) gives. In addition, it

is noteworthy the occasional presence of few spherical nanoparticles, which can be associated to a possible silane self-condensation reaction, as reported in similar treatments [4].

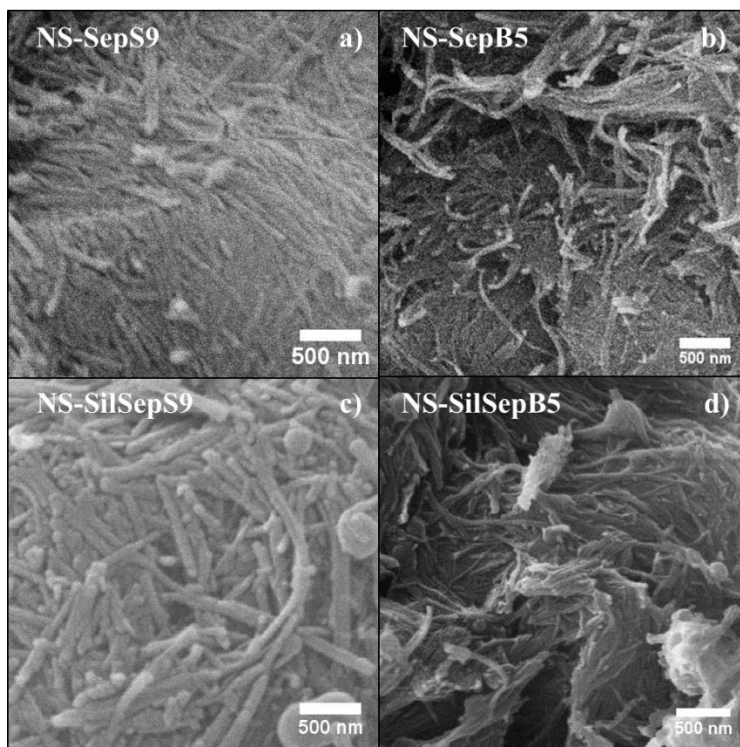


Figure 3.3 SEM micrographs of (a) NS-SepS9, (b) NS-SepB5, (c) NS-SilSepS9 and (d) NS-SilSepB5.

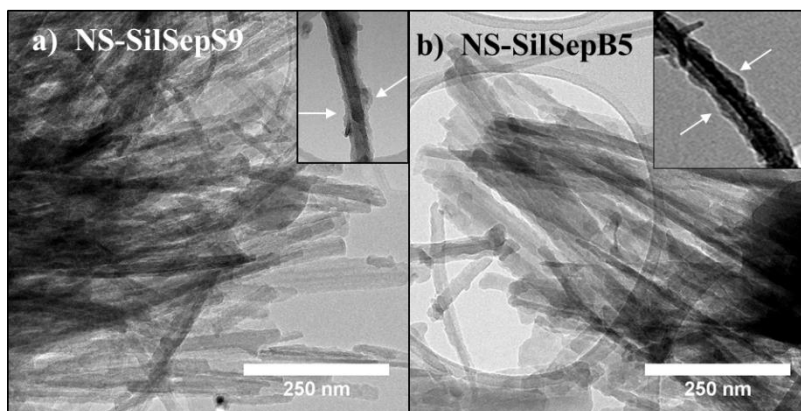


Figure 3.4 TEM images of (a) NS-SilSepS9 and (b) NS-SilSepB5. In the insets, the HR-TEM of an individual fiber of NS-SilSepX.

In general, it is possible to assume that most of TESPT reacts with the Sep surface, as further confirmed by NMR investigation. HR-TEM images reveal a uniform silicate coating of the fiber surface, clearly distinguishable from the silicate fiber (insets magnification of Fig. 3.4).

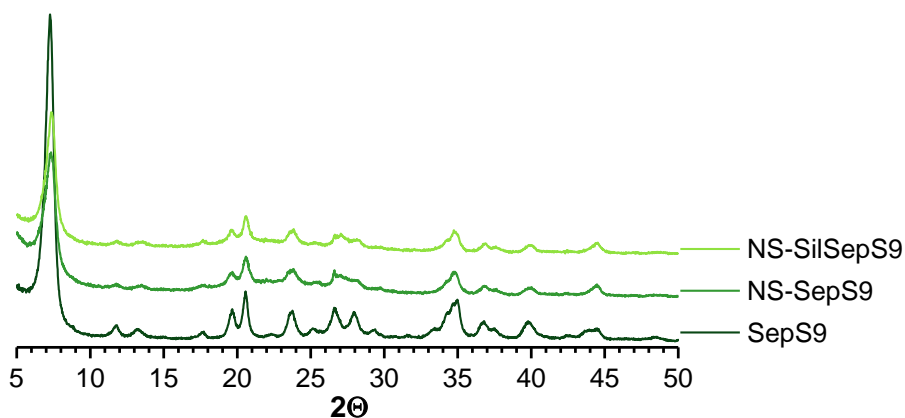
3.1.2 Powder X-Ray diffractometry

XRD analysis was performed on SepX, NS-SepX and NS-SilSepX samples in order to verify that the acid treatment and the functionalization process do not alter the crystalline structure of Sep (Fig. 3.5).

The diffractograms of pristine SepS9 and SepB5 are similar to those of the materials obtained after 2h of acid treatment. The characteristic reflections at $2\theta = 7.3^\circ, 12.3^\circ, 17.7^\circ, 19.8^\circ, 35.0^\circ$ correspond to the (110), (130), (150), (060) and (371) crystal planes of Sep, respectively [5]. Thus, the acid procedure does not destroy the clay crystal structure. According to the Scherrer equation, the slight broadening and weakening of (110) reflection of the modified Sep suggests that acid treatment produces a size reduction of Sep fibers. On the other hand, these changes could be related to different crystallinity of the samples.

The band component analysis of the (110) reflection of the studied Sep allows the detection of two components in this diffraction peak with differences related to both positions and the full width at half maximum (FWHM) of the components. Peak position hasn't undergone any change, as expected for a system like this that does not exfoliate. By considering the FWHM a measure of the crystallinity of the sample (near to the delta of Dirac near to the complete crystallinity) a simple peak analysis (Fig. 3.6) shows that acid treatment gives rise significant changes in the FWHM compared to the not treated samples.

a)



b)

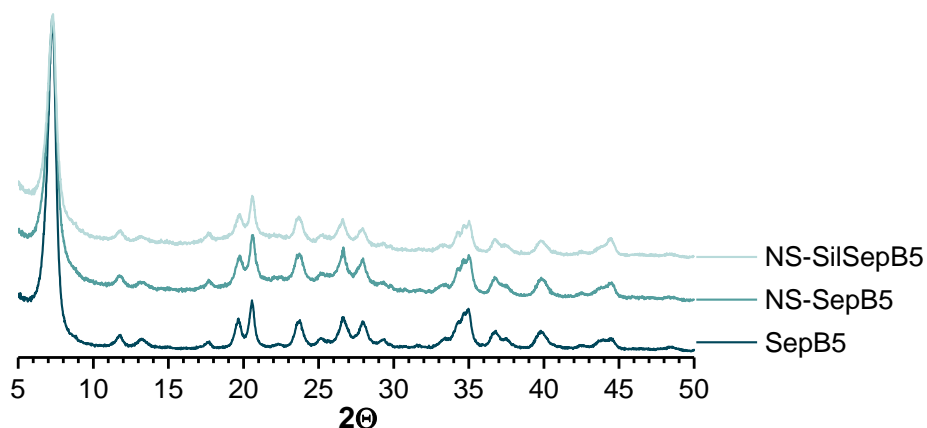


Figure 3.5 XRD patterns of top SepS9 (dark green), NS-SepS9 (green), NS-SilSepS9 (light green) (a) and (b) SepB5 (dark blue), NS-SepB5 (blue), NS-SilSepB5 (light blue).

Sample NS-SepS9 shows the higher increment in FWHM indicating a higher loss of crystallinity. This is supported from ICP data (paragraph 4.1.6) that shows the maximum Mg leached for that sample. Furthermore, the evaluation of particle dimension shows that NS-SepS9 shows the bigger decrement in length (see Table 3.9 of Paragraph 3.2.3).

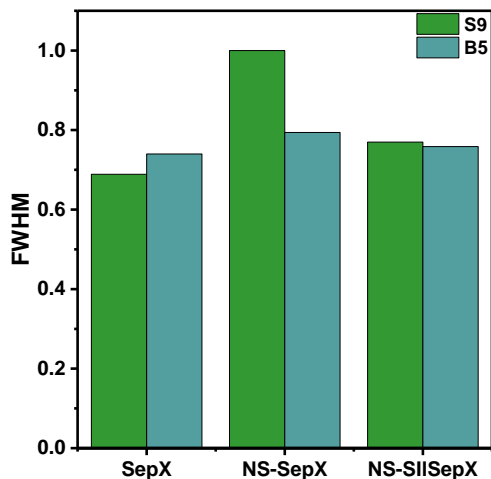


Figure 3.6 FWHM of the (110) peak calculated from the normalized peak.

3.1.3 FT-IR Spectroscopy

The changes in Sep chemical structure after acid treatment were studied by ATR-FTIR. The spectra of pristine and modified Sep samples are shown in Fig.3.7 and the characteristics vibrations are highlighted and listed in Table 3.1

The NS-SepS9 spectra (green line in Fig. 3.7 a) evidences the adsorption bands at $3700\text{--}3555\text{ cm}^{-1}$, attributable to the stretching vibrations of O-H groups and water molecules bounded to octahedral magnesium centers, and at 692 cm^{-1} , assignable to the Mg-O bending vibrations.[6] Although reduced in intensity with respect to pristine Sep (black dashed line in Fig. 4.36a), these peaks confirm that the Mg-OH bonds were only partially destroyed by the acid treatment.

Simultaneously, the band at 3754 cm^{-1} , assigned to structural hydroxyls attached to silanol groups, increases in intensity mainly in NS-SepS9 indicating the formation of the reactive silanol groups after acid treatment.

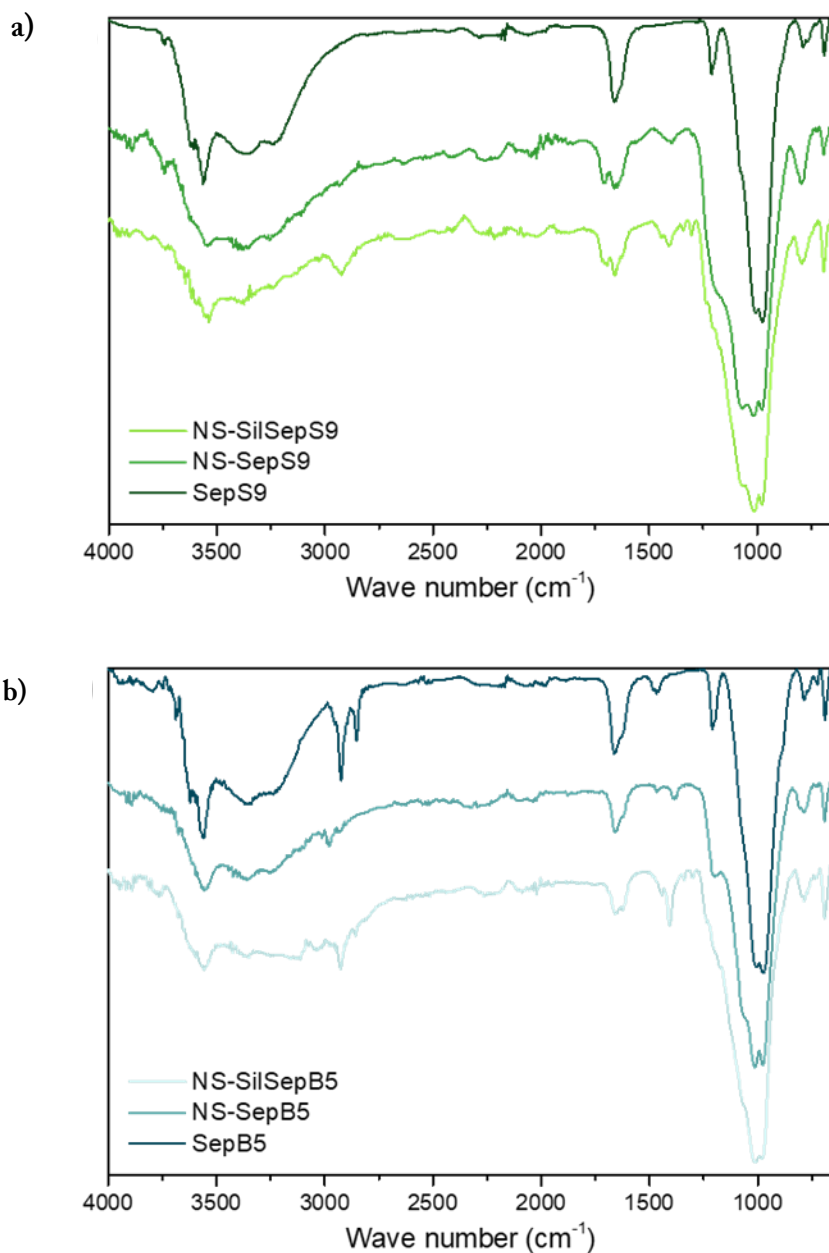


Figure 3.7 FTIR adsorption spectra of (a) SepS9 (dark green), NS-SepS9 (green), NS-SilSepS9 (light green) and (b) SepB5 (dark blue), NS-SepB5 (blue), NS-SilSepB5 (light blue).

The Si–O bands of tetrahedral sheets changed their shapes, in particular the bands at 1057 and 1018 cm⁻¹ merge into one peak occurring at 1068 cm⁻¹ which

is associated to amorphous silica [7]. Moreover, the band of amorphous silica near 795 cm^{-1} increases in intensity along the acid treatment [8],[9]. The changes of the Si–O stretching band and the shift toward 1068 cm^{-1} indicate a progressive release of the Mg atoms from the octahedral sheets.

The NS-SilSepS9 spectrum (light green Fig. 3.7a) confirms the silane functionalization with the appearance of bands ascribable to the CH_3 and CH_2 stretchings of TESPT ($2977\text{--}2890\text{ cm}^{-1}$) and the corresponding bending modes ($1346, 1303, 1438\text{ cm}^{-1}$).

Table 3.1 Characteristic vibrational frequencies (cm^{-1}) for SepX, NS-SepX and NS-SilSepX.

SepS9	NS-SepS9	NS-SilSepS9	SepB5	NS-SepB5	NS-SilSepB5	Assignment
3754	3754	3760	3750	3757	3750	SiO-H stretching
3700-3555	3700-3555	3700-3555	3710-3555	3710-3555	3710-3555	MgO-H stretching
—	—	2977-2890	2923, 2846, 1661	2923, 2850,	2923, 2849, 1661 2977-2850	Alkyl asym. stretching
—	—	1346, 1303, 1438	1467	1468	1346, 1303, 1438	Alkyl asym. bending
1057,1000	1069, 1012	1069, 1012	1076, 1000	1063, 1015	1063, 1015	Si-O asym. stretching
976	979	979	977	977	977	Si-OH
689	692	692	687	693	691	Mg-O bending
—	796	798	—	794	796	Si-O-Si sym stretching

The SepB5 spectrum (dark blue Fig. 3.7b) presents the vibrations of benzyl alkyl chain at $2923, 2849, 1661\text{ cm}^{-1}$, in addition to the SepS9 absorption bands. NS-

SepB5 (blue) and NS-SilSepB5 (light blue) spectra have similar trends and changes comparable to those described above for the SepS9.

The NS-SilSepS9 spectrum (light green Fig. 3.7a) confirms the silane functionalization with the appearance of bands ascribable to the CH₃ and CH₂ stretchings of TESPT (2977-2890 cm⁻¹) and the corresponding bending modes (1346, 1303, 1438 cm⁻¹).

The SepB5 spectrum (dark blue Fig. 3.7b) presents the vibrations of benzyl alkyl chain at 2923, 2849, 1661 cm⁻¹, in addition to the SepS9 absorption bands. NS-SepB5 (blue) and NS-SilSepB5 (light blue) spectra have similar trends and changes comparable to those described above for the SepS9.

3.1.4 Solid State NMR

Multinuclear solid-state NMR analysis was performed in order to further understand and confirm the Sep structural and chemical changes due to both, acid etching and silanization.

Sep structure has four types of silicon atoms: three Q³ Si atoms and one Q² Si atom. Q³ refers to a silicon atom that is attached to three other silicon atoms through oxygens; the Q² silicon atom is attached to two other silicon atoms through oxygens. In literature, ²⁹Si CPMAS NMR for pure Sep shows three well-resolved resonances (Fig. 3.8a top) of approximately equal intensity for its three Q³ silicon atoms at -92.7 (Si2), -94.3 (Si3) and -98.2 ppm (Si1)[10][11]. Each of the three main resonances has been attributed to one of the three pairs of equivalent Si nuclei in the basal plane, and the resonance at about -85 ppm to Q² (Si-OH) Si nuclei. In literature, proofs of the assignment can be found: On the basis of the COSY experiment, the resonance at -92.7 ppm is unambiguously assigned to the intermediate, near-edge Si sites. The HETCOR experiment revealed that the resonance at -94.3 ppm cross-polarizes almost entirely from the Mg-OH protons, and therefore is assigned to the central Si position. The remaining resonance at -98.2 ppm correlates strongly to the

protons of the structural water molecules and therefore is assigned to the edge Si sites [10]. The Si local environment is almost identical for SepB5 with that of SepS9, pointing out that the organic modification in SepB5 does not affect the Si sites.

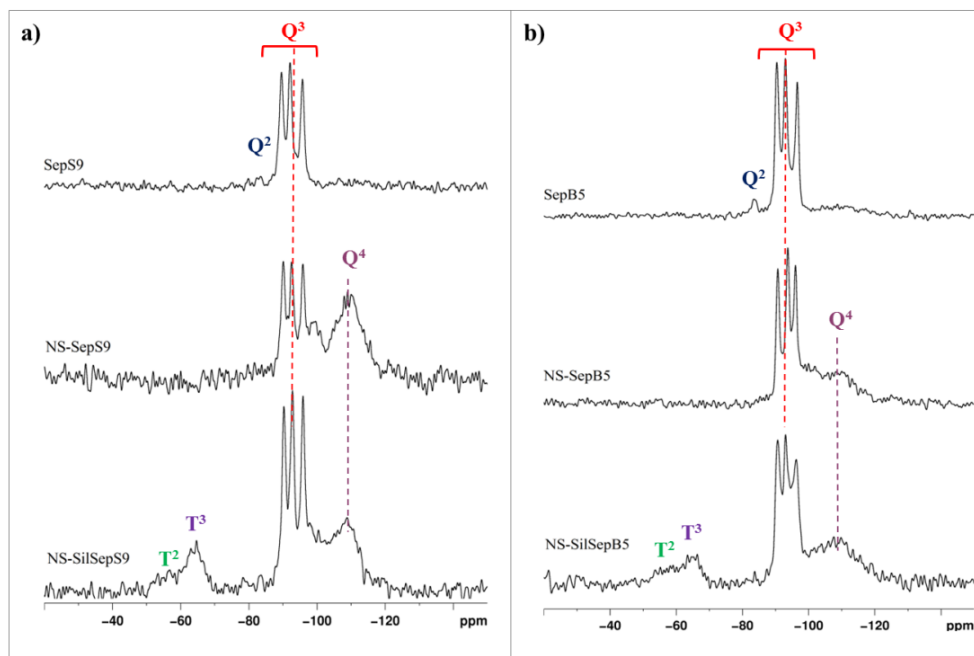


Figure 3.8 ^{29}Si MAS NMR spectra of (a) SepS9, NS-SepS9 and NS-SilSepS9 and (b) SepB5, NS-SepB5 and NS-SilSepB5.

Acid treatment of both SepS9 and SepB5 causes the following changes in the spectra relative to NS-SepS9 and NS-SepB5: i) disappearance of $\text{Q}^2(\text{Si-OH})$ peak, ii) the appearance of a broad resonance at about -100 and -110 ppm, due to Q^3 and Q^4 units due to the amorphous SiO_2 and iii) the small shift of the resonance assigned to Si2 and Si3 in the basal plane. As reported in the literature [12], the Q^4 units derive from the partial dissolution of Mg^{2+} cations of the octahedral sheet [1],[13] that leads to the formation of new silanol groups, in agreement with the presence of the Q^3 units.

The silanization treatment leads, in the spectra of the samples NS-SilSepS9 and NS-SilSepB5, to the appearance of the signals at -56 and -65 ppm, respectively due to the T² and T³ units derived from TESPT. The control experiments (data not shown) confirmed that the reaction of Sep with TESPT in isopropanol does not proceed in the absence of the acid treatment. As a matter of facts, no peaks attributable to pristine or condensed TESPT were detectable in the ²⁹Si NMR spectra.

The degree of TESPT condensation, namely DOC was calculated on the basis of the following equation:

$$\text{DOC \%} = \frac{T^1 + 2 * T^2 + 3 * T^3}{3 * (T^0 + T^1 + T^2 + T^3)} * 100 \quad (\text{Eq. 3.1})$$

DOC is about 90% and the Sep/TESPT ratio is about 100:20 in sample NS-SilSepS9. According to the results reported in Table 3.2, both DOC and amount of TESPT are slightly lower in the samples prepared with SepB5. Interestingly, the position and the ratio among the three sharp Q³ resonances of the clay are kept in both samples, thus demonstrating that the removal of Mg²⁺ cations and the silanization step takes place without depleting the original phyllosilicate structure. The broad resonance due to Q⁴ and Q³ units in the amorphous silica counts for about 46% and 56% of the whole Sep Si units, for NS-SilSepB5 and NS-SilSepS9 respectively. According to the results of Table 4.2, it appears that the organic functionalization of the pristine Sep as in the case of SepB5 reduces the extent of the reactions both with the acid solution and the silane. The amount of amorphous silica decreases in both cases with TESPT addition respect to the pure acid treatment.

Table 3.2 ^{29}Si NMR chemical shifts δ (ppm), amounts and assignments.

Si unit	SepS9	SepB5	NS-SepS9	NS-SepB5	NS-SilSepS9	NS-SilSepB5
T ²	—	—	—	—	-55.4	-56.7
T ³	—	—	—	—	-65.2	-64.5
Q ² (Si-OH)	-85.8	-85.5	—	—	—	—
Q ³ (1Mg) Si2	-92.4	-92.4	-92.8	-93.2	-93.0	-93.1
Q ³ (1Mg) Si3	-94.9	-95.0	-95.3	-96.2	-95.4	-95.5
Q ³ (1Mg) Si1	-98.6	-98.6	-98.6	-98.6	-98.6	-98.6
Q ³	—	—	-100.4	-100.6	-100.9	-100.4
Q ⁴	—	—	-110.5	-110.0	-110.2	-110.2
Sep/TESPT	—	—	—	—	80.3/19.7	82.7/17.3
%Q of Sep.	—	—	68.7	54.6	55.9	45.5
DOC % (TESPT)	—	—	—	—	91.5	87.7

The ^{13}C CPMAS spectra of Fig. 3.9 clearly show the differences between the two used Sep. Signal positions and peak assignments are summarized in Table 3.3. The ^{13}C spectrum of SepS9 is featureless, since the pristine Sep does not possess any organic component and no isopropanol molecules are retained in the channels even after acid treatment. Indeed, the spectrum of NS-SepS9 appears flat. On the contrary, SepB5 spectrum shows at about 33 ppm the signal of the methylene groups ascribable to the Sep functionalization with N,N-didodecyl-N-methylammonium; in addition, the sharp resonances of the iPr-OH trapped in the channels are clearly visible in the NS-SepB5 spectrum. In the spectra of both NS-SilSepX, the successful functionalization with TESPT is proved by the presence of the characteristic carbon signals of the propyl chain linked to the silicon atom. The presence of iPrOH is confirmed by the small broad peak at 67 ppm but no signals due to the -OEt groups are detected suggesting their complete hydrolysis in the presence of acid.

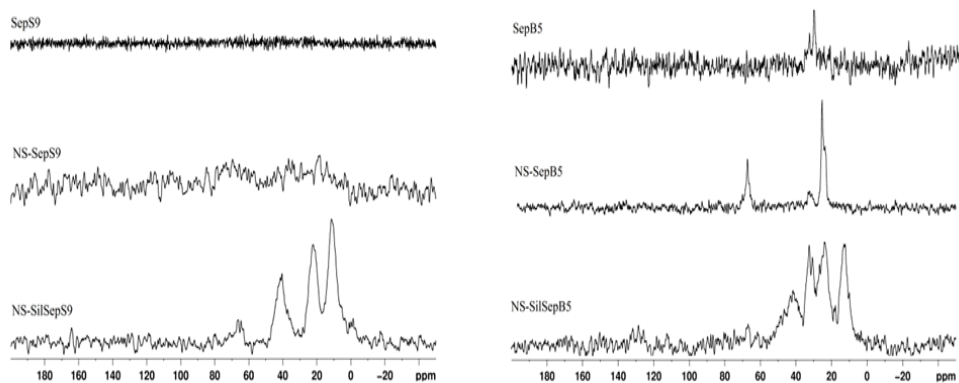


Figure 3.9. ^{13}C CPMAS spectra of the Sep samples.

Table 3.3 ^{13}C NMR chemical shifts and assignments for SepB5 and SepS9 samples.

δ (ppm)	Functional group	Assignment
13.4	Si-CH ₂ -	TESPT
23.9	-CH ₂ -	TESPT
25.2	-CH ₃	iPr-OH
32.9	-CH ₂ -	R-N ⁺ -didodecyl chain
41.7	-CH ₂ -S	TESPT
67.6	-CH ₂ --OH	iPrOH

It is worth of noting that NS-SilSepB5 spectrum shows the maintenance of the original functionalization with N,N-didodecyl-N-methylammonium. The presence in SepB5 of organic molecules with large steric demand and locally affecting the medium polarity could be the reason for the lower yield in amorphous silica formation and TESPT functionalization respect to SepS9, as pointed out by the ^{29}Si NMR study.

The ^1H MAS NMR spectrum of the pristine Sep SepS9 presents two overlapped resonances as shown in Fig. 3.10

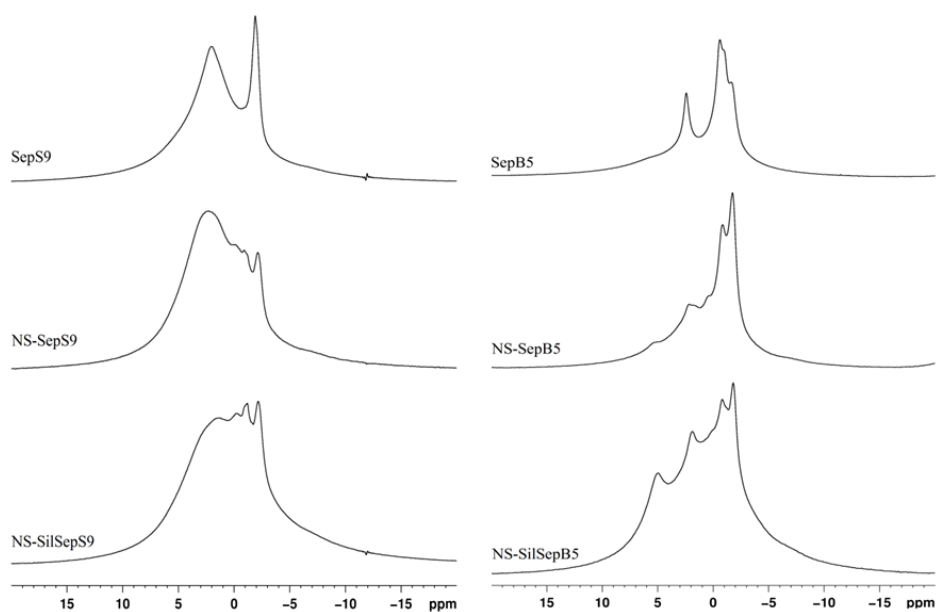


Figure 3.10 ^1H CPMAS spectra of the Sep samples.

According to the literature [10], the sharp component centered at -1.8 ppm is assigned to MgOH groups and the broad signal centred at 2.2 ppm is produced by the contribution of water molecules on the external surface of the Sep, those free to move inside the Sep tunnels and those coordinated to magnesium. The acid treatment in *i*Pr-OH (NS-SepS9) leads to the appearance of a new resonance at -0.9 ppm similar in intensity to that of MgOH signal. This peak is present in both the modified samples as the resonance at around 0.3 ppm. The reaction with HCl generates a very broad and intense peak at about 2 ppm which is also present, but broader in NS-SilSepS9, probably as a consequence of the overlapping with the TESPT methylene signals. Aramendia [12] proposed that the formation of amorphous silica by acid treatment leads to the appearance of new silanols. In agreement with the signals of Q^3 units detected in the ^{29}Si spectra, the Si-OH functions could contribute to the proton spectrum with a signal around 2 ppm that overlaps to the water signal at 2.2 ppm.

The ^1H spectra of pristine and modified SepB5 present some differences respect to those of SepS9 samples, as a consequence of the organic modification with N,N-didodecyl-N-methylammonium and the favorable interaction with isopropanol pointed out by the ^{13}C NMR spectra. In SepB5 spectrum, the water resonance at 2.2 ppm peak is sharp according to the main contribution of the free water molecules entrapped in the tunnels with a low amount of external water (left shoulder). The MgOH peak is overlapped with two intense sharp peaks at -0.8 and -1.1 ppm, probably due to the methylene protons of the dodecyl chain. The spectrum of sample NS-SepB5 shows the presence of other peaks related to the iPr-OH entrapment in the Sep channels, as already suggested by ^{13}C spectrum. The broadening increases after silanization due to the overlapping with the TESPT methylene signals, but the water resonance in NS-SilSepB5 appeared reduced in comparison to the corresponding signal in NS-SilSepS9.

In conclusion, the NMR results confirm that the acid treatment causes the formation of the amorphous silica by Mg extraction and, in these conditions, TESPT can hydrolyze and condense interacting with Sep, as clearly demonstrated by the TEM images. The behavior of SepB5 appears conditioned by the organic modifier which partially reduces the reactivity of the Sep against acid etching and silanization in comparison with SepS9.

3.1.5 Elemental analysis

On the basis of CHNS data (Table 3.4), the degree of functionalization of NS-SilSepX with TESPT was estimated 17.88% for NS-SilSepS9 and 18.45% for NS-SilSepB5, in agreement with NMR and TGA analyses. This estimation was made considering that the S is given only by the TESPT grafted on the fibers.

Table 3.4 CHNS analysis of Sep samples.

	C %	H %	N %	S %
SepS9	2.70	2.10	0.00	0.00
NS-SepS9	2.19	2.02	0.00	0.00
NS-SilSepS9	7.66	2.42	0.00	10.73
SepB5	10.64	2.96	0.00	0.00
NS-SepB5	2.36	1.92	0.00	0.00
NS-SilSepB5	10.62	2.72	0.00	11.07

3.1.6 ICP-AES analysis Mg^{2+} determination

ICP-AES analysis were performed to quantify the amount of extracted magnesium (Fig. 3.11) in relation with the presence of both TESPT and organic modifier of SepB5. The results are in perfect agreement with the conclusions of the NMR study on the effects of organic modifier in SepB5 and TESPT addition. The maximum fraction of Mg^{2+} leached after 2h of acid treatment was 80% for SepS9 and only 45% for SepB5: so, it is lower in the presence of organic modifier. Besides in the presence of TESPT, the percentage is lower with respect to the simple acid treatment (46% for SepS9 e 32% for SepB5). This suggests that the Mg^{2+} extraction is strongly affected by both TESPT and the organic modifier. In particular, we can hypothesize that, in the presence of TESPT, the Mg^{2+} extraction is accompanied by the linkage of organosiloxyl groups that form a layer coverage of the residual silicate. This coating should delay further extraction of Mg^{2+} ions. In the case of SepB5, the alkylammonium in the interlayers prevents the income of the protons into the Sep interlamellar region, especially in the presence of TESPT (45% respect to 32% of extracted Mg^{2+}), as reported in the literature for different kind of clays [14].

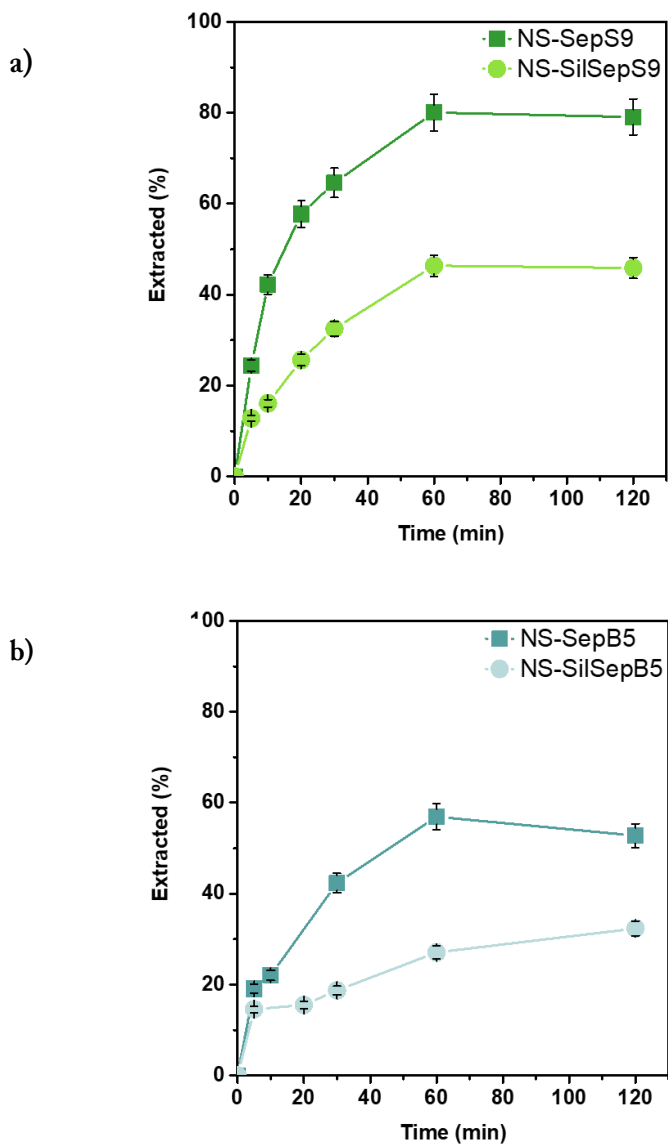


Figure 3.11 The percentage of extracted Mg^{2+} ions for (a) SepS9 during the acid treatment (green ■ line) and in the presence of TESPT (light green ● line) and (b) SepB5 during the acid treatment (blue ■ line) and in the presence of TESPT (light blue ● line) at different reaction times.

In all cases, the ICP analysis confirms the possibility of removing Mg^{2+} cations without depleting the original phyllosilicate structure, as demonstrated by XRD and ^{29}Si NMR spectra.

3.1.7 Nitrogen adsorption-desorption experiments

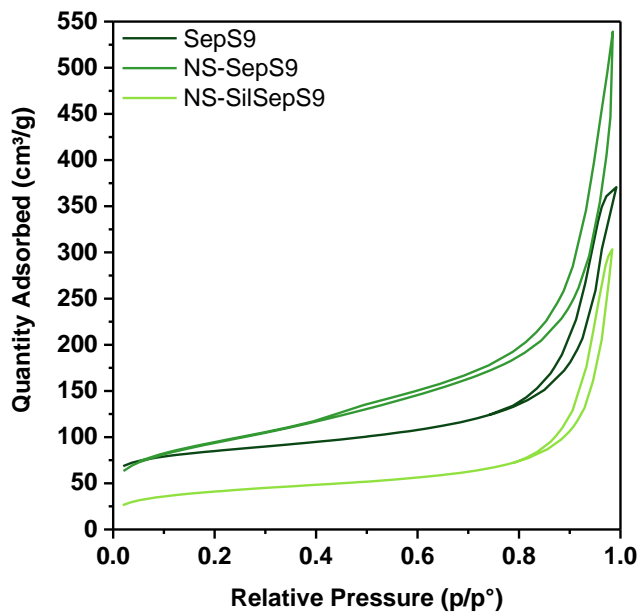
As reported in the literature [15], Sep in its pristine form exhibit high specific surface area (SSA) mainly due to the small size of its particles, the fibrous morphology and intra crystalline channels. SSA is influenced by the external surface area and the micropores. BET surface areas of Sep reported in literature range from 80 to 350 m²/g [15]. This large range can be attributed to the variability of natural samples and different procedures of sampling.

The nitrogen adsorption-desorption isotherms for pristine Sep and obtained products are shown in in Fig 3.12

Since all samples are evacuated and analyzed with the same procedures and conditions, the changes of isotherm profile can be attributed to acid treatment and functionalization. Pristine SepS9 exhibited a type II isotherm according to the classification of Brunauer–Deming–Deming–Teller (BDDT)[16] associated with a micro-mesoporous structure with a hysteresis loop. The isotherms of the modified samples correspond to type II typical of materials with mesopores of 2-50 nm[17] and present very small hysteresis loops corresponding to Type H4, which suggests the presence of narrow slit-shaped pores [15][18].

The main results of the textural analysis of both starting and modified Sep are shown in in Table 3.5.

a)



b)

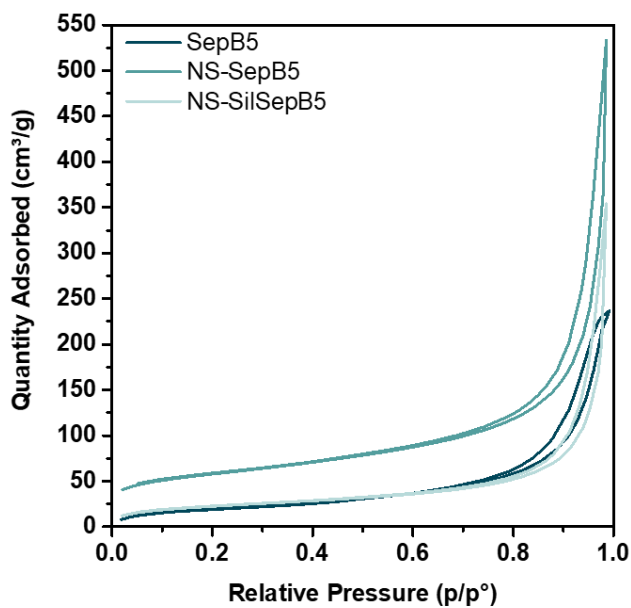


Figure 3.12. Adsorption-desorption isotherm at liquid nitrogen temperature of (a) SepS9 (dark green line), NS-SepS9 (green line), NS-SepS9 (light green line) and b) of SepB5 (dark blue line), NS-SepB5 (blue line) and NS-SilSepB5 (light blue line)

Table 3.5 Properties of SepX, NS-SepX and NS-SilSepX

	SSA _{BET}	SSA _{Ext}	SSA _{mp}	V _{mp,t}	V _{mp,BJH}
	(m ² /g)	(m ² /g)	(m ² /g)	(cm ³ /g)	(cm ³ /g)
SepS9	310	121	189	0.0767	0.544
NS-SepS9	331	210	121	0.0713	0.708
NS-SilSepS9	147	74	73	0.0319	0.44
SepB5	72	87	nd	nd	0.366
NS-SepB5	204	158	46	0.0182	0.578
NS-SilSepB5	82	71	10	0.0026	0.313

n.d. not determined.

SSA: specific surface area; SSA_{Ext} external specific area, V_{mp,t} volume of micropores. V_{mp,BJH} specific mesopore volume

SepB5 exhibited the lowest SSA due to the presence of the quaternary ammonium which limits the accessibility of N₂ molecules along the micro channels.

After acid treatment, SSA increases in both NS-SepX, especially for NS-SepB5. The increase of SSA for NS-SepS9 can be attributed to the extraction of Mg²⁺: the magnesium leaching creates new defects in the Sep structure that can lead to a more accessible area. In addition, this increase in SSA has been classically related to the appearance of an amorphous silica phase due to the partial dissolution of the octahedral sheet of sepiolite with the acid treatment [19]. This is supported by the increment in the mesoporous volume from 0.544 to 0.708, as reported in Table 3.5.

Similarly, the increase of SSA of NS-SepB5 can be attributed to the partial elimination of the quaternary ammonium salt, as confirmed by NMR and CHNS data.

As expected, both NS-SilSepX samples show a SSA decrease due to the grafting of TESPT on the Sep surface which blocks the access of the N₂ molecules used in the BET measurements to the micro channels. This was demonstrated by the pore distribution of Sep samples (Fig. 3.13).

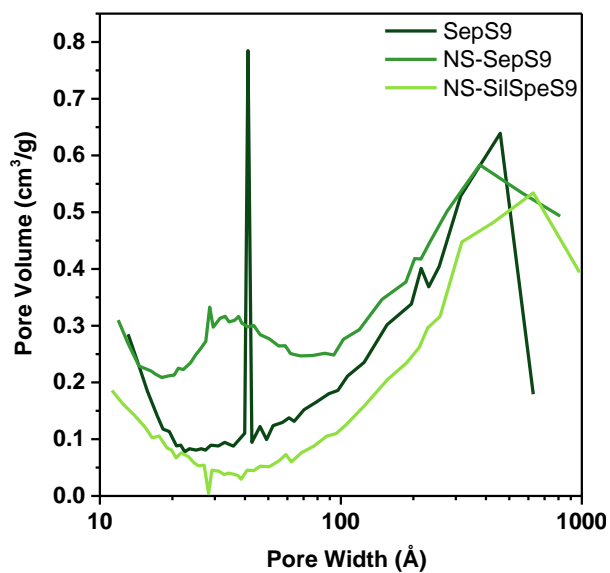
The distribution of micro and mesoporosity varies after acid treatment for both SepX materials. In fact, SepS9 shows a peak around 30-40 Å which is characteristic to all Sep samples [15]. This peak is related to the entrance of N₂ molecules inside the Sep intra crystalline channels. Instead SepB5 does not present peak in the micro porous area due to the presence of alkyl ammonium salt, but only a broadened peak in the meso and macro porous mainly due to the fiber aggregation.

After acid treatment, NS-SepS9 exhibits a peak broadening in the 30-50 Å area, related to the Mg²⁺ ions leaching that causes an increment on the channel dimension, while NS-SepB5 is characterized again by the appearance of the peak at 30-40 Å due to the partial extraction of magnesium ions of quaternary ammonium salt.

After silanization acid treatment, NS-SilSepX samples show the same pore distribution: the presence of silane grafted on Sep surface prevents the N₂ access inside the channels so SSA is given from the meso pores and macro pores derived from the fibers aggregation.

To summarize, this exhaustive analysis supports that the acid surface activation, here described, provides NS-SepX with reduced particle size, preserving the anisotropic features and increasing the bonding sites at the Sep surface.

a)



b)

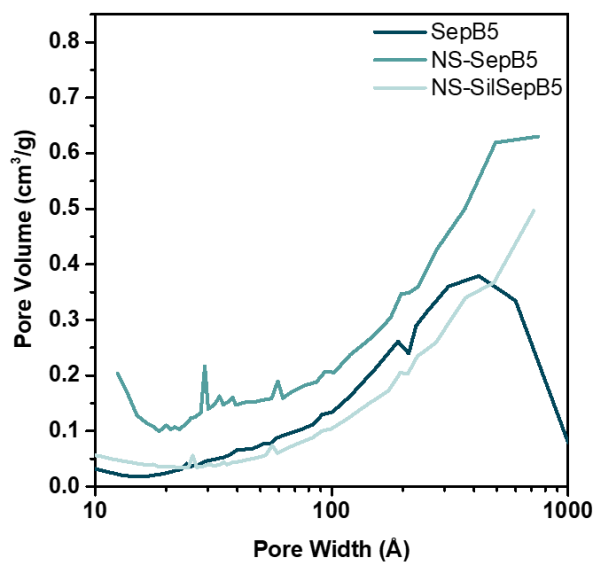


Figure 3.13 Pore distribution of (a) SepS9 (dark green), NS-SepS9 (green) and NS-SilSepS9 (light green) and (b) SepB5 (dark blue), NS-SepB5 (blue) and NS-SilSepB5 (light blue)

3.2. Sep SBR Nanocomposite

NS-Sep fibers were used to prepare SBR nanocomposites by ex-situ blending.

Dynamic-mechanical tests were performed in order to study the filler-filler and filler-rubber interactions. An integrated approach of TEM analysis with NMR was applied to visualize the stiffer elastomer zone at the interface. The mobility of rubber chains close to the filler particles were investigated by low field ^1H NMR measurements. Thus, morphological observations were correlated to the dynamic-mechanical data in order to highlight the role of the Sep nanofibers in enhancing the functional properties.

3.2.1 Rheological and dynamic-mechanical properties

The effect of modified Sep fillers in comparison to pristine Sep was studied by rheological and dynamic-mechanical analyses.

The rheometric characteristics of the Sep/SBR nanocomposites, such as the minimum torque (M_L) and the maximum torque (M_H) are reported in Table 3.6.

The minimum torque (M_L), defined as the torque at the initial stage of vulcanization and related to the viscosity of the compounds, reflects the clay dispersion aptitude in the uncured samples. In fact, the SepB5/SBR composite showed lower M_L , likely due to the presence of some free ammonium salt in SepB5, working as lubricant and secondary accelerator. When the ammonium salt is partially removed during acid treatment, M_L value is higher for NS-SepB5/SBR and NS-SilSepB5/SBR composites.

The presence of the modified Sep fillers in SBR polymer produces positive effect on the maximum torque (M_H), which is a measure of crosslink density and stiffness of the rubber. In particular the improved M_H of NS-SilSepX/SBR with respect to both SepX and NS-SepX/SBR suggests good interaction between Sep

filler and rubber in NS-SilSepX cured composites, thanks to the presence of TESPT.

Table 3.6. Curing characteristic of Sep/SBR nanocomposites.

Samples	Scorch time (min)	M _L (Nm)	M _H (Nm)	M _H -M _L (Nm)
SepS9/SBR	2.67	2.73	13.36	10.63
NS-SepS9/SBR	4.08	2.47	10.43	7.96
NS-SilSepS9/SBR	4.35	2.38	14.65	12.27
SepB5/SBR	2.81	1.29	15.43	14.14
NS-SepB5/SBR	4.10	2.30	12.87	10.57
NS-SilSepB5/SBR	3.37	2.61	17.56	14.95

Nanocomposite with NS-SilSepB5, having better dispersibility and surface chemistry, shows the best interaction with the sulfur-based vulcanization compounds, leading to enhanced mechanical properties in the rubber composition. Probably, the presence of quaternary ammonium salts favors a more efficient curing of sulfur-based rubber compositions [20].

Successively, a detailed RPA analysis was performed to evaluate the filler-filler interaction of the Sep network and the Sep-polymer interaction, over a large shear range. The storage modulus (G') of the uncured composites containing NS-SepX and NS-SilSepX, as well as of the vulcanized ones, has been assessed and compared with that of the composites with pristine SepX (Fig. 3.14 and 3.15).

Fig. 3.14 shows the dependence of the G' of SepS9/SBR, NS-SepS9/SBR and NS-SilSepS9/SBR samples against the strain amplitude. In all cases a significant nonlinear trend is observed. In fact, the G' value at low strain decreases quickly by increasing the strain amplitude, and at large strain, it approaches the lowest

value. In agreement with the literature [21],[22], this marked dependence of the modulus, referred to as Payne effect, can be related to:

- i. the destruction-reformation of a filler network;
- ii. the adsorption-desorption of polymeric chains at the filler interface;
- iii. the disentanglement of bulk polymer from the rubber bounded to the filler surface;
- iv. the strain-softening of the more rigid polymer shell surrounding the particles surfaces.

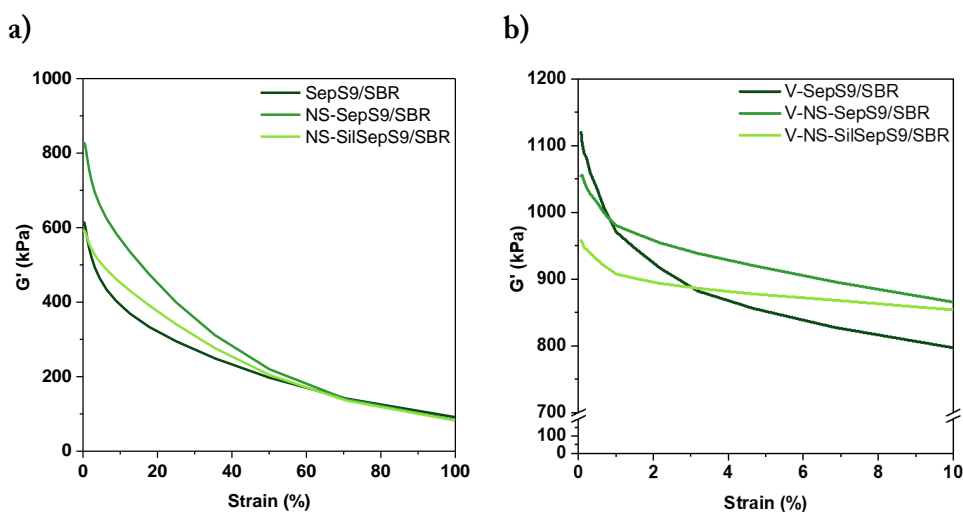


Figure 3.14 Storage modulus G' vs strain of (a) SepS9/SBR (dark green line), NS-SepS9/SBR (green line), NS-SilSepS9/SBR (light green line) and (b) V-SepS9/SBR (dark green line), V-NS-SepS9/SBR (green line), V-NS-SilSepS9/SBR (light green line).

Before curing, the NS-SepS9/SBR and NS-SilSepS9/SBR composites show highest moduli at low strain (G'_0). At the highest deformation, the modulus (G'_∞) resulted very similar for all the composites (Fig. 3.14 a).

After curing (Fig. 3.14b), an increase of the modulus either at low or at high strain is observed for all the composites. In particular the highest G'_0 value was obtained for V-SepS9/SBR, compared with V-NS-SepS9/SBR and V-NS-

SilSepS9/SBR composites. Instead at high strain, the effect is much more evident for the NS-SepS9/SBR and NS-SilSepS9/SBR composites, resulting in the highest G'_{∞} value. In any case, the composites containing modified Sep fibers exhibit the lowest decrease of modulus versus strain, that is, the lowest Payne effect. This suggests a strong immobilization of the polymer chains close to the nanofibers surfaces or within their network, which increases the mechanical reinforcement of the composites. Evidently after acid treatment and ex-situ silanization, the fiber interaction with the polymer improves as well as the cross-linking coupling because of the high number of bonding sites. Considering this higher reinforcing effect, we can also assume that the nanofibers are percolated within SBR matrix, in agreement with the TEM evidences (see Paragraph 3.2.3).

RPA analysis of SepB5 composites is reported in Fig. 3.15. The G' of SepB5/SBR, NS-SepB5/SBR and NS-SilSepB5/SBR (Fig. 3.14a) shows trends similar to those of the SepS9 composites; although G'_0 values of NS-SepB5/SBR and NS-SilSepB5/SBR are much greater than those of pristine SepB5/SBR. In comparison to the SepS9/SBR (dark green line in Fig. 3.15a), G'_0 value of SepB5/SBR is approximately 50% lower, corresponding to 300 KPa. This indicates that the presence of the organic linker on the surface hinders both the fibers aggregation in SBR matrix and the formation of a percolating network.

After curing, the RPA curves in Fig 3.15b show:

- i) increase of the modulus both at low and high strain;
- ii) higher G'_0 value of V-SepB5/SBR;
- iii) higher G'_{∞} value of V-NS-SepB5/SBR and V-NS-SilSepB5/SBR;
- iv) $\Delta(G'_{\infty}-G'_0)$ values much lower in V-NS-SepB5/SBR and V-NS-SilSepB5/SBR than in V-SepB5/SBR.

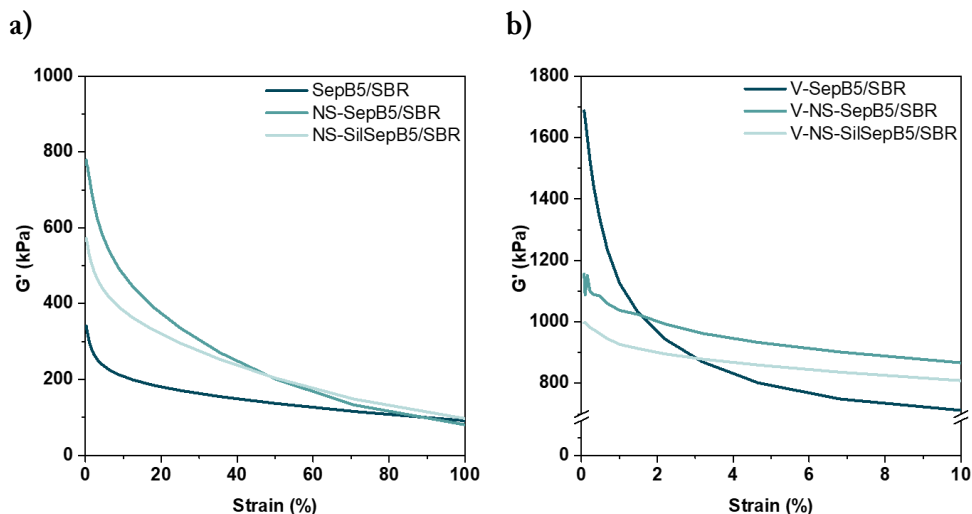


Figure 3.15 Storage modulus G' vs strain of (a) SepB5/SBR (dark blue line), NS-SepB5/SBR (blue line), NS-SilSepB5/SBR (light blue line) and (b) V-SepB5/SBR (dark blue line), V-NS-SepB5/SBR (blue line), V-NS-SilSepB5/SBR (light blue line).

On the basis of these results, the acid treatment seems to be critical for modulating the filler-filler and even more the filler-rubber interactions. In fact, the use of NS-Sep fibers filler, obtained by acidification of pristine SepX, simultaneously provides greater reinforcing effect and enhanced filler-rubber interaction, as well as excellent strain independence of modulus.

To better understand the improvement in mechanical properties due to NS-Sep fibers with respect to SepX and to the standard nanosilica, we analyzed the values of $G'(9\%)$, $\Delta(G'_{\infty}-G'_0)$ and loss tangent as Tan Delta (9%), which represent respectively the measure of reinforcement, Payne effect and hysteresis in vulcanized rubbers (Table 3.7).

Compared with pristine SepX, the presence of NS-SepX and NS-SilSepX produce an enhanced reinforcement in corresponding composites, consisting in the higher $G'(9\%)$ value. It is worthy noted that the $G'(9\%)$ value of all Sep based samples are consistent with that of SiO_2 nanocomposite, while the Payne effect of both V-NS-SepX/SBR and V-NS-SilSepX/SBR turns out to be lower.

Table 3.7 Dynamic properties: Storage modulus (9%), Payne effect as $G'(0.5)-G'(10)$, Loss factor as TanDelta (9%) of V-NS-SepX/SBR and V-NS-SilSepX/SBR composites in comparison with the standard V-SiO₂/SBR and V-SepX/SBR composites.

	G'(9%) (MPa)	G'(0.5)-G'(10) (MPa)	TanDelta (9%)
V-SiO ₂ /SBR	0.834	0.252	0.081
V-SepS9/SBR	0.797	0.242	0.084
V-NS-SepS9/SBR	0.866	0.152	0.105
V-NS-SilSepS9/SBR	0.854	0.077	0.052
V-SepB5/SBR	0.705	0.614	0.132
V-NS-SepB5/SBR	0.864	0.218	0.089
V-NS-SilSepB5/SBR	0.807	0.153	0.072

Finally, it is worth noting that the dynamic loss tangent of NS-SilSepX fibers in SBR matrix are significantly reduced. Thus, when Sep is functionalized ex-situ during the acid procedure (such as for V-NS-SilSepX) the compatibilization reaction is complete, resulting in a significant improvement of filler-rubber interaction.

The $\tan \delta$ values at 10 Hz and 9% of dynamic strain is a good marker of rubber material hysteresis and can be associated to the rolling resistance, defined as the energy consumption under tire operative conditions. For this, on the basis of data reported in Table 3.7, it appears that NS-SilSepX fibers could significantly improve rolling resistance.

In conclusion, the mechanical analyses support that the presence of NS-Sep fibers, generated by the acid treatment, clearly improves the reinforcing effect while reducing the hysteretic behavior of SBR nanocomposites.

3.2.2 Temperature dependent dynamic-mechanical analysis

DMTA analyses of cured Sep composites were made in order to correlate the filler morphology with storage (E') and loss (E'') modulus and with loss tangent ($\tan \delta$), in the temperature range from -40 to $+80$ °C.

The measurements show the effect of the reduced rubber mobility, due to the Sep fibers, on the mechanical properties of the nanocomposites. The E' trend is plotted in Fig. 3.16 for pristine and modified SepX in comparison with unfilled V-SBR composite.

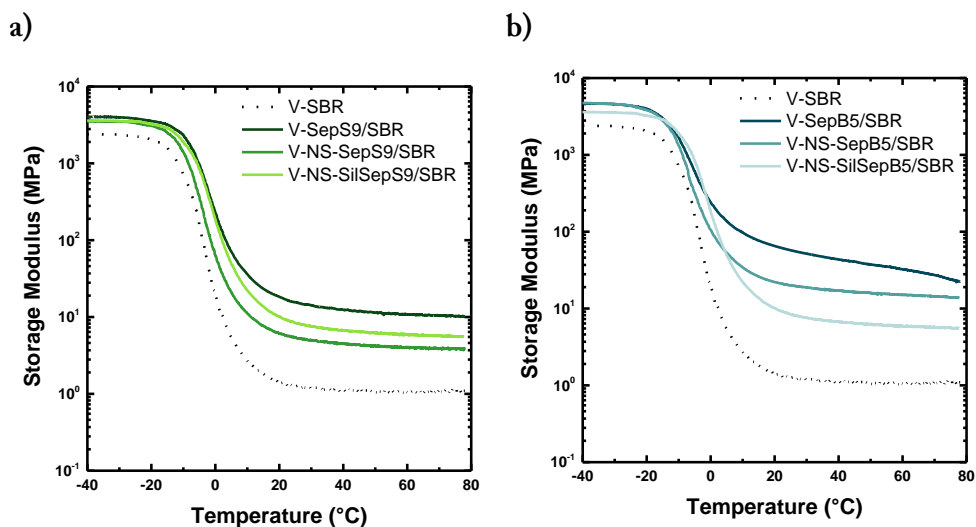


Figure 3.16 Storage modulus vs. temperature for (a) V-SBR (black dotted line), V-SepS9 (dark green line), V-NS-SepS9 (green line), V-NS-SilSepS9 (light green line) and for (b) V-SBR (black dotted line), V-SepB5 (dark blue line), V-NS-SepB5 (blue line) and V-NS-SilSepB5 (light blue line)

The E' reflects the elastic modulus of the rubber materials, which measures the recoverable strain energy in a deformed specimen. As expected, the modulus of the neat SBR is lower than that of the SepX/SBR composites (Fig. 3.16) due to the absence of reinforcing fillers. At higher temperatures, due to the fast segmental mobility of rubber chains, the reinforcing effect of Sep fillers becomes

more apparent. It is evident that with the increase of temperature, the addition of Sep enhances the stiffness of SBR and a shift of rapid decreasing region of E' can be seen for the pristine Sep composites. A sharp fall in E' after $-20\text{ }^{\circ}\text{C}$ evidence the T_g region as modulus decreases drastically on going from the glassy state to the rubbery state. However, the trend changes at higher temperatures (above $0\text{ }^{\circ}\text{C}$) as the composites containing pristine Sep show an increase in storage modulus compared to pure SBR. The Sep nanocomposites exhibit much enhancement in storage modulus as compared to that of neat SBR in the temperature range of $0\text{--}40\text{ }^{\circ}\text{C}$. This is due to the mechanical reinforcement by particles at high temperatures. Above T_g , when materials become soft, the reinforcement effect of the filler particles becomes prominent and hence the composites exhibit strong enhancement of modulus. The significant increase in storage modulus is marked above the glass transition region because the relative reinforcing effect of rigid nanoclay on SBR matrix is enhanced over this temperature change. The result is also supported by the contribution of hydrodynamic reinforcing effect due to the dispersion of the nanosized filler in the SBR matrix, which is well controlled by the shape factor and filler volume fraction of the organoclay.

Elastic modulus of composites prepared with modified Sep is lower than that of the pristine one. This can be correlated to the change in AR induced by the acid treatment (see Paragraph 3.2.3) which allows the self-assembly of Sep nanofibers. As described in the literature [23][24], anisotropic rod-like particles provide stronger reinforcement of the rubber if compared with the spherical ones. This is due to the ability of anisotropic particles to self-assemble in filler superstructures where rubber chains are immobilized in the inter-particle region [24].

Figure 3.17 shows the loss modulus (E'') data for all Sep composite materials.

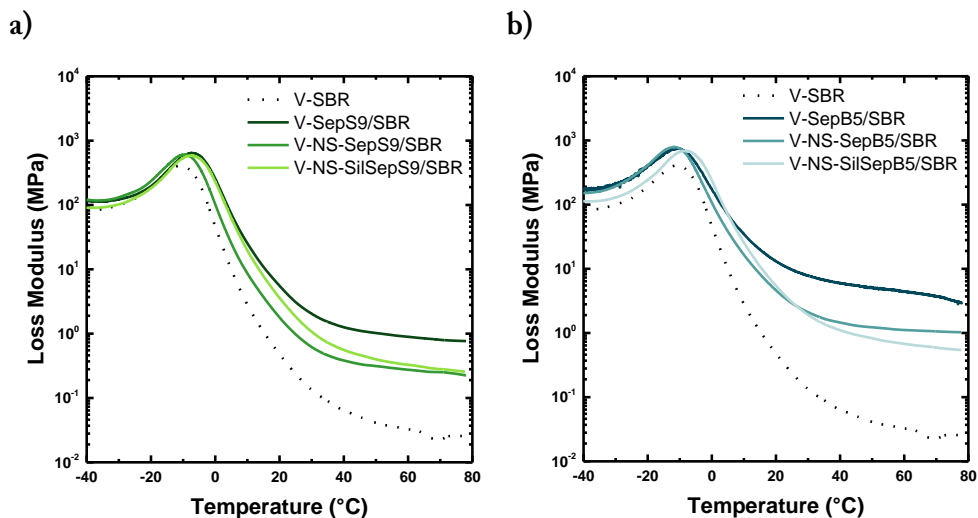


Figure 3.17 Loss Modulus vs. temperature for (a) V-SBR (black dotted line), V-SepS9 (dark green line), V-NS-SepS9 (green line), V-NS-SilSepS9 (light green line) and for (b) V-SBR (black dotted line), V-SepB5 (dark blue line), V-NS-SepB5 (blue line), V-NS-SilSepB5 (light blue line).

Generally, E'' is a measure of dissipated energy as heat per cycle under deformation, i.e. the viscous response of the material. The E'' peak represents the temperature at which the material is undergoing the maximum change in polymer mobility, which corresponds to the chemical definition of the glass transition. E'' increases by increasing temperature until to reach a maximum value that gives the T_g , according to some authors [25]. Above T_g , this friction is reduced and E'' value decreases for higher temperatures, as a result of the free movement of the polymer chains. T_g value of Sep nanocomposites are reported on Table 3.8

It is clear that E'' increase after the introduction of SepX (Fig. 3.17) over the entire temperature regime in comparison with neat SBR (dotted line in Fig 3.17).

Table 3.8 E', E'' and tan δ values of Sep nanocomposites at 30 and 70 °C and Tg values of Sep nanocomposites

	E' at 30 °C (MPa)	E' at 70 °C (MPa)	E'' at 30 °C (MPa)	E'' at 70 °C (MPa)	tan δ at 30 °C	tan δ at 70 °C	Tg from E'' (°C)	Tg from tan δ (°C)
SBR	1.11	1.09	0.13	0.02	0.11	0.02	-10.73	0.73
SepS9	14.23	10.43	2.03	0.80	0.14	0.07	-7.1	1.93
NS-SepS9	4.99	3.89	0.62	0.25	0.12	0.06	-9.68	0.09
NS-SilSepS9	7.60	5.69	1.06	0.28	0.14	0.04	-7.44	2.8
SepB5	51.74	27.32	7.77	3.71	0.15	0.13	-11.5	-3.03
NS-SepB5	18.82	10.43	2.1	1.05	0.11	0.07	-11.8	-2.97
NS-SilSepB5	14.47	10.47	1.91	0.59	0.13	0.05	-8.3	1.21

In addition, the incorporation of Sep fibers causes a broadening of the loss modulus peak. This broadening may be attributed to the inhibition of the relaxation process within the composites as a consequence of a higher number of chain segments interacting with Sep fibers. There is also an apparent shift in Tg toward higher temperatures for V-SepS9 (Table 3.8) that can be primarily attributed to the segmental immobilization of the matrix chain at the fiber surface[26]. In the case of SepB5, the Tg has a shift at lower temperatures (Table 3.8), mainly due to the presence of the alkylammonium salt that acts as a plasticizer.

It is worth noting that V-NS-SepX/SBR and V-NS-SilSepX/SBR show a significant lower value of E'' in the rubbery region. This indicates that the modification of the Sep fibers introduces a better interaction with the matrix reducing the dissipative process in the rubber nanocomposites. Especially in the case of V-NS-SilSepX, the presence of the grafted silane allows the better filler-rubber interaction. The E'' value at 30 and 70 °C for composites studied are listed in Table 3.8.

Damping factor was also analyzed to better understand the relationship between elastic and loss modulus and relative data are presented in Fig 3.18.

Generally, the $\tan\delta$ value quantifies the measure of balance between the elastic phase and the viscous phase in a polymeric structure. In composites, damping

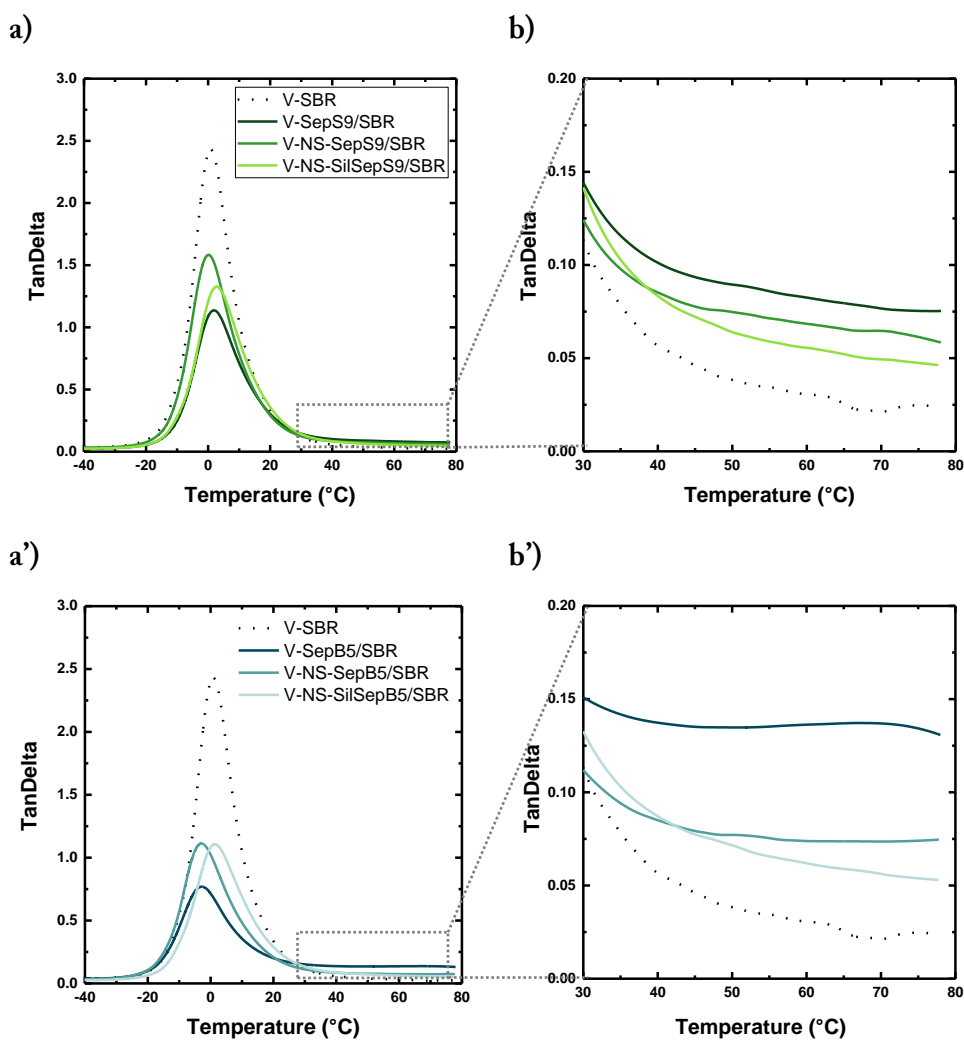


Figure 3.18. $\tan\delta$ vs. temperature for (a) V-SBR (black dotted line), V-SepS9/SBR (dark green line), V-NS-SepS9/SBR (green line) and V-NS-SilSepS9/SBR (light green line); (b) V-SBR (black dotted line), V-SepB5/SBR (dark blue line), V-NS-SepB5/SBR (blue line) and V-NS-SilSepB5/SBR (light blue line) and the corresponding magnification (a' and b') in the 40 °C- 80 °C range at their right.

factor is influenced by the incorporation, type and distribution of fibers, as well

as the fiber/matrix interaction and the void content. Some authors also suggest the use of the maximum value of $\tan\delta$ as T_g [27][28]. The T_g of rubber composites, obtained from $\tan\delta$ values, is listed in Table 3.8.

Interestingly, there is a significant effect of Sep fibers on shape of damping curve. In fact, in the presence of both pristine and modified SepX, the height of damping maximum decreases while simultaneously the damping peak is broadened. The compounds with Sep show strong decrease in $\tan\delta$ peak compared to pure SBR. This corresponds to reinforcing tendency of the filler in the matrix. In particular, the mobility of rubber chains is reduced at interface of active fillers or in the confinement of the filler network. Reduction in the magnitude of peak loss factor is quantitatively related to reduction in the amount of free rubber as a result of its immobilization in the presence of filler particles. Reduced chain mobility owing to physical and chemical adsorption of the SBR chain segments on the filler surface causes a height reduction of $\tan \delta$ peak during dynamic mechanical deformation.

As an indication of skidding behavior (grip, traction) on dry roads, the level of the loss tangent around 25 °C can be taken. The range between +30 °C and approximately +70 °C comprises the running temperatures of a tyre. Under these temperature conditions, the loss factor essentially determines the degree of rolling resistance. Tan delta value at 70 °C is an indication of rolling resistance. It should be pointed out that $\tan\delta$ value at 70 °C (Table 3.8) for both modified NS-SepX and NS-SilSepX is significantly lower than that of pristine Sep. Replacement of pristine Sep by modified Sep results in a decrease of $\tan\delta$ at higher temperatures and thereby in a reduction in the rolling resistance. This means that on increasing the temperature, nanoSep filled materials display a larger portion of filler network, which can be broken down and reformed during cyclic deformation with respect to modified NS-SepX and NS-SilSepX.

3.2.3 Morphology characterization by HR-TEM

The effect of the acid treatment on the size and dispersion of Sep fibers was investigated by TEM analysis of uncured and cured composites. Thus, morphological observations through spatial TEM analysis were correlated to the mechanical data to highlight the role of the Sep nanofibers in enhancing the functional properties.

TEM images of uncured composites, namely SepS9/SBR, NS-SepS9/SBR and NS-SilSepS9/SBR are reported in Fig. 3.19, while TEM images of V-SepS9/SBR, V-NS-SepS9/SBR and V-NS-SilSepS9/SBR are reported in Fig. 3.20. Dark lines in the figures correspond to the fibers dispersed in the rubber matrix.

Images at low magnification (Fig. 3.19 a,b,c and Fig. 3.20 a,b,c) testify the particle distribution in a large area of the nanocomposites. In all samples, the materials seem to have a partial aggregation of Sep fibers. Especially in the V-NS-SepS9/SBR and V-NS-SilSepS9/SBR, the rubber matrix shows several zones, poorer in filler particles. That is, the polymer network appears to be more discontinuous in samples containing modified Sep fibers than in samples with pristine SepS9. However, images at higher magnification (Fig.3.19 a', b', c' and Fig. 3.20 a', b', c') reveal a more complex fibers spatial distribution.

In the Fig. 3.20a', V-SepS9/SBR contains exclusively individual fibers and tactoids, homogeneously distributed in the matrix without any preferential orientation.

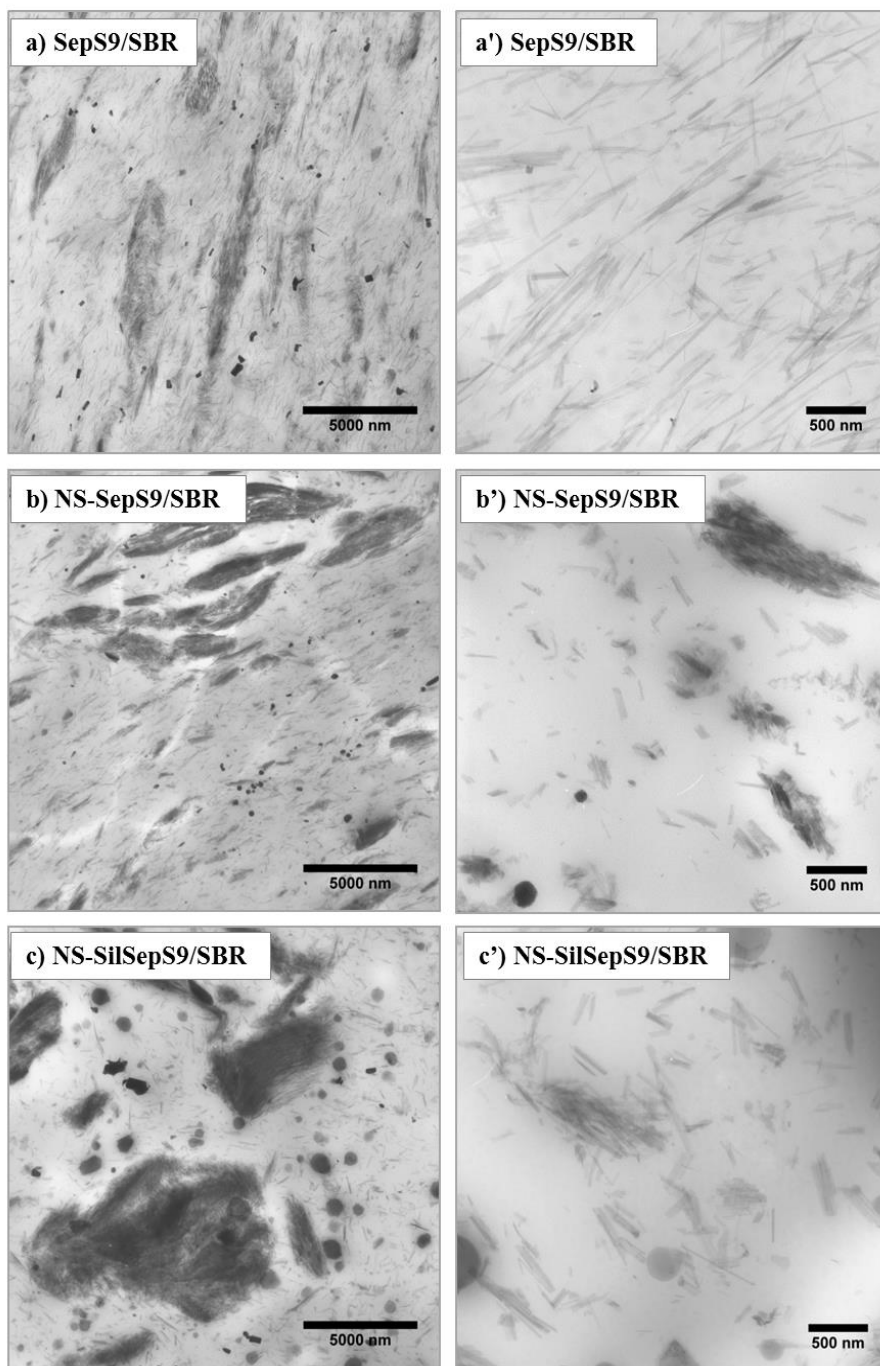


Figure 3.19 TEM images at different magnification of uncured SBR composites containing respectively a) and a') SepS9, b) and b') NS-SepS9, c) and c') NS-SilSepS9

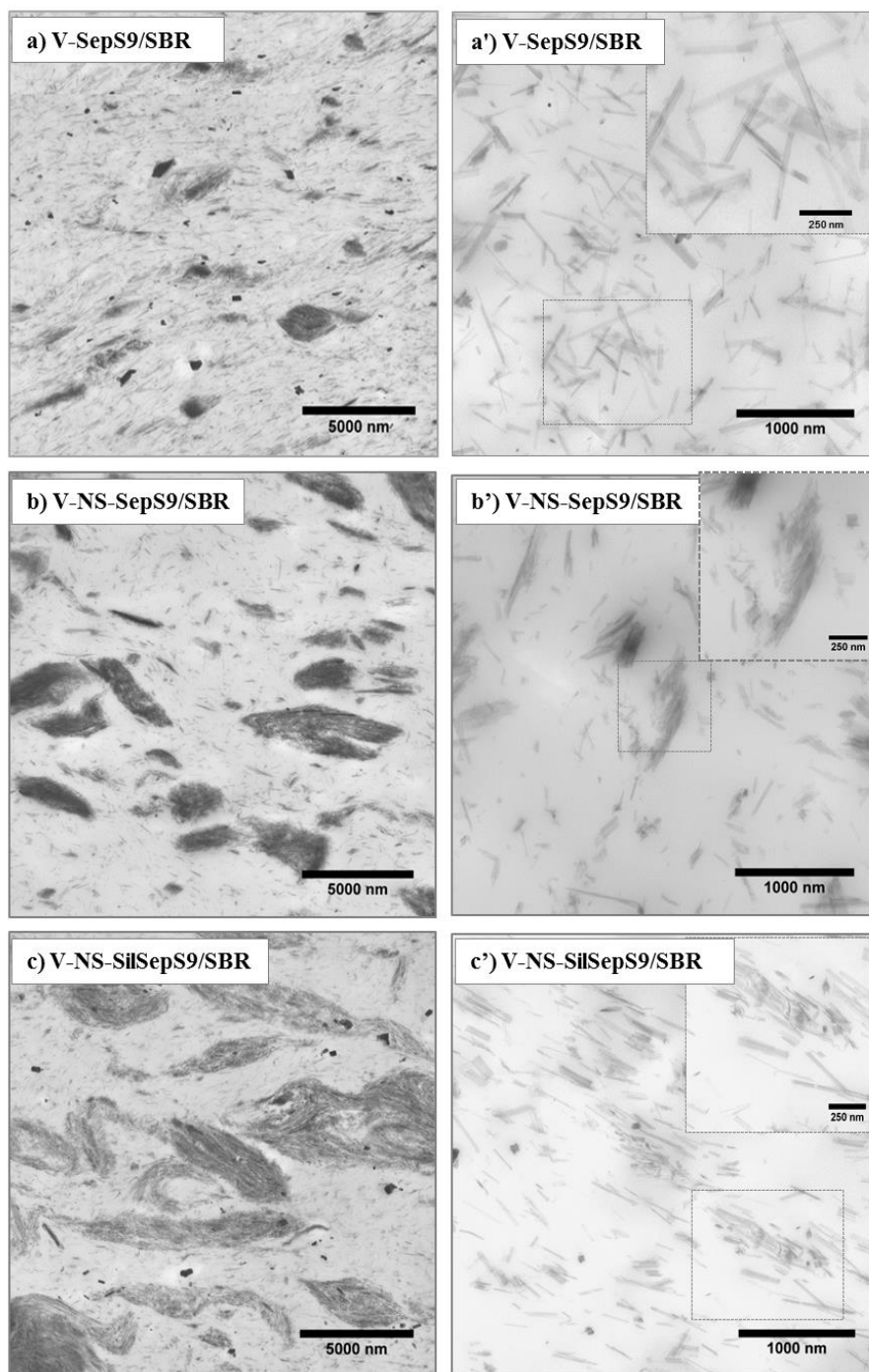


Figure 3.20 TEM images at different magnifications of (a, a') V-SepS9/SBR, (b, b') V-NS-SepS9/SBR, (c, c') V-NS-SilSepS9/SBR.

The individual fibers preserve the geometric size of pristine Sep and the anisotropic feature, roughly estimated through the representative TEM images and reported in Table 3.9. The AR values for SepS9 is about 30, while the length and cross-section are 770 ± 187 and 24 ± 7 nm respectively.

Table 3.9 Size dimensions* of SepX, NS-SepX and NS-SilSepX and corresponding filler network structure, obtained by TEM analysis.

	INDIVIDUAL FIBER			FILLER NETWORK STRUCTURE	
	Length (nm)	Cross-section (nm)	AR	Length (nm)	Cross-section (nm)
SepS9	767 ± 187	24 ± 7	30 ± 16	–	–
NS-SepS9	88 ± 29	21 ± 6	4 ± 2	1488 ± 468	567 ± 213
NS-SilSepS9	484 ± 157	20 ± 6	23 ± 14	1076 ± 286	275 ± 85
SepB5	886 ± 244	20.3 ± 6.2	44 ± 25	–	–
NS-SepB5	348 ± 93	29 ± 12	12 ± 8	988 ± 400	526 ± 73
NS-SilSepB5	523 ± 198	33 ± 19	15 ± 14	1497 ± 308	410 ± 79

*Calculated as average of 29 fibers in 3 different TEM micrographs

Instead, in the V-NS-SepS9/SBR and V-NS-SilSepS9/SBR composites, the fiber size, due to acid treatment, are significantly reduced: AR is 4 for NS-SepS9 and 23 for NS-SilSepS9. Interestingly, when the fibers length decreases, a preferential self-organization of the particles in anisotropic structures occurs. TEM images clearly show the presence of “percolative filler network structures”, consisting not only of directly interacting particles, but also of polymer chains bridging the particles. This filler-rubber interaction is evident by rubber layer surrounding the particles (see the insets in Fig. 3.20 b', c'). The wideness of network structures ranges from 0.57 to 0.87 micron in V-NS-SepS9/SBR, while

in V-NS-SilSepS9/SBR it is about 0.27-1.3 μm . Particle alignment is diffused in the whole rubber matrix and the filler network structures seem not oriented in only one direction. This fiber organization occurs in spite of the mixing process used to obtain the composites and though no external or internal procedure was performed to drive the particle arrangement [29].

Fig. 3.21 shows TEM images of SepB5/SBR, NS-SepS9/SBR and NS-SilSepS9/SBR, while the images of corresponding cured nanocomposites V-SepB5/SBR, V-NS-SepB5/SBR and V-NS-SilSepB5/SBR are reported in Fig. 3.22). By images at low magnification of samples containing pristine SepB5 (3.21 a, and 3.22 a), it is evident that the quaternary ammonium salt improves the compatibility between fibers and SBR matrix, and thus the SepB5 dispersion. In addition, the SepB5 fibers are totally orientated in V-SepB5/SBR sample (Fig. 3.22 a and b), while they are randomly dispersed in SepS9/SBR (Fig. 3.20 a and b). As well documented in the literature [30] this orientation occurs when anisotropic particles were subjected to shear strain of the RPA analysis during vulcanization process. This phenomenon does not occur for SepS9 because of strong inter-particle aggregation.

After acid treatment, TEM analysis again display a complex structural distribution of the modified NS-SepB5 and NS-SilSepB5 (Fig. 3.21 b, c and Fig. 3.22 b, c). Once more, fibers spontaneously assemble and form filler network structures, approximately of cross-section about 530 nm for NS-SepB5 and 310 nm for NS-SilSepB5. Also in this case, the reduced size dimensions of individual Sep fibers (Table 3.9) can be related to the typical networking distribution in NS-SepB5 and NS-SilSepB5.

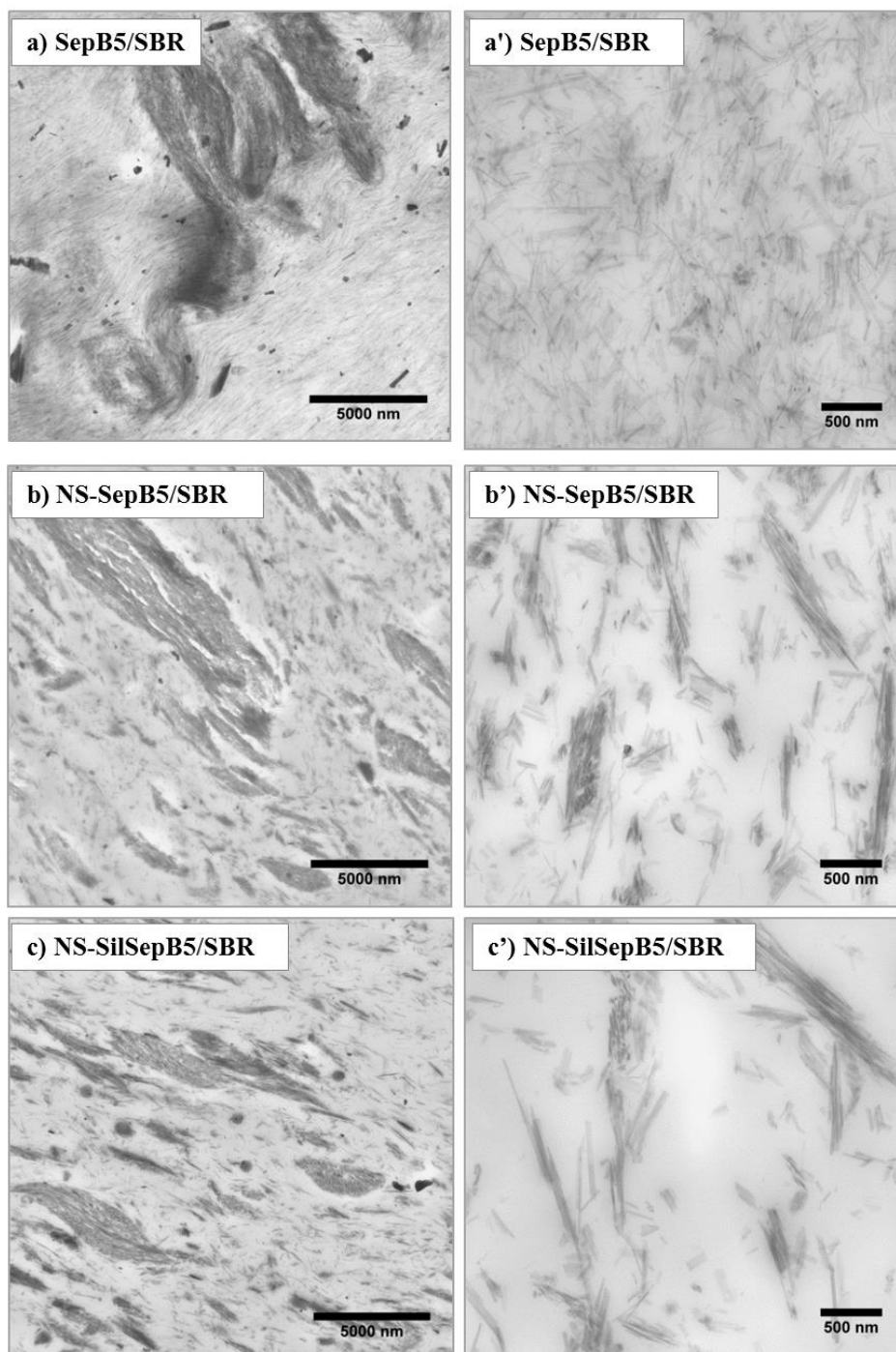


Fig 3.21 TEM images at different magnification of uncured SBR composites containing respectively a) and a') SepB5, b) and b') NS-SepB5, c) and c') NS-SilSepB5

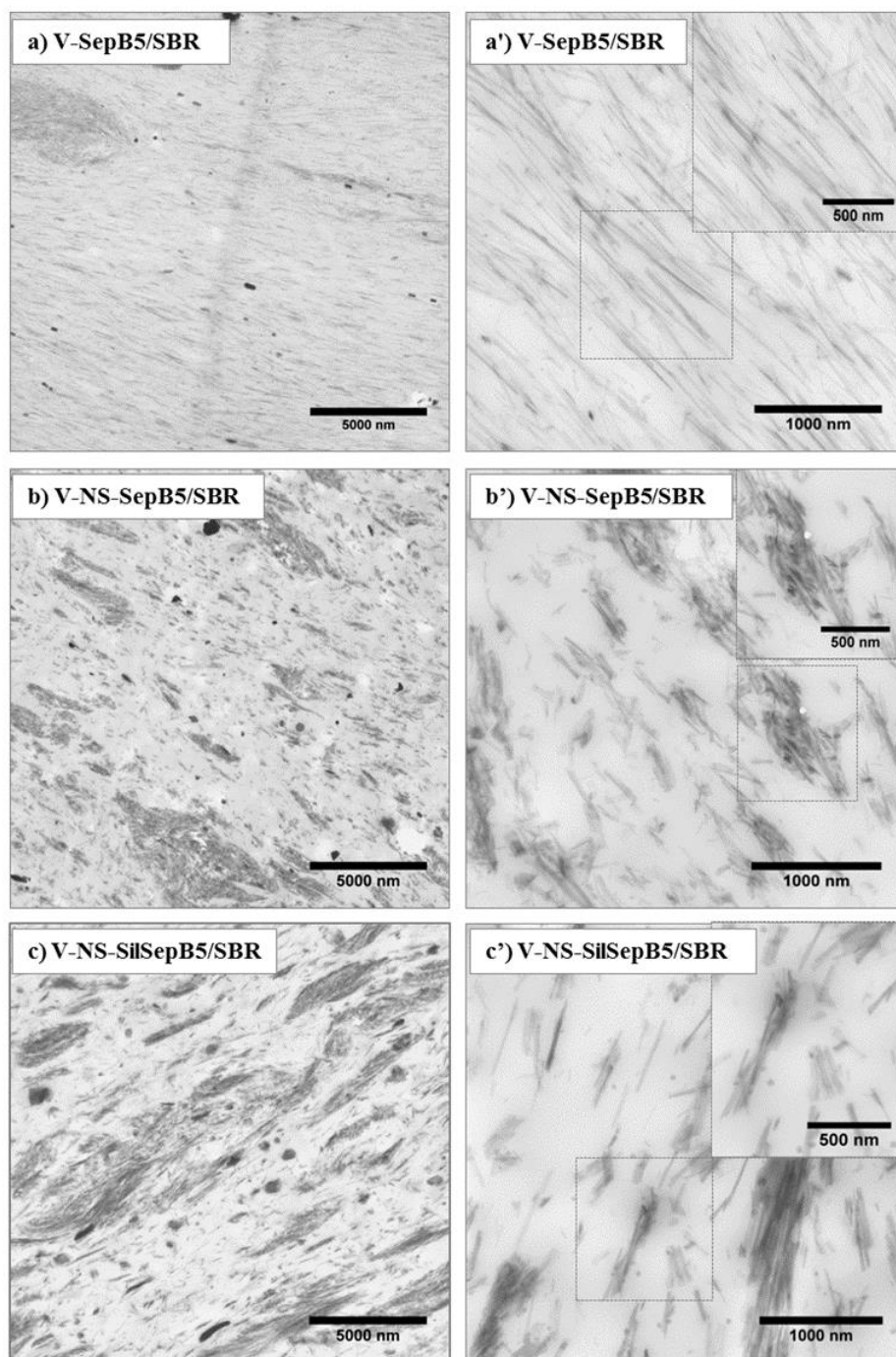
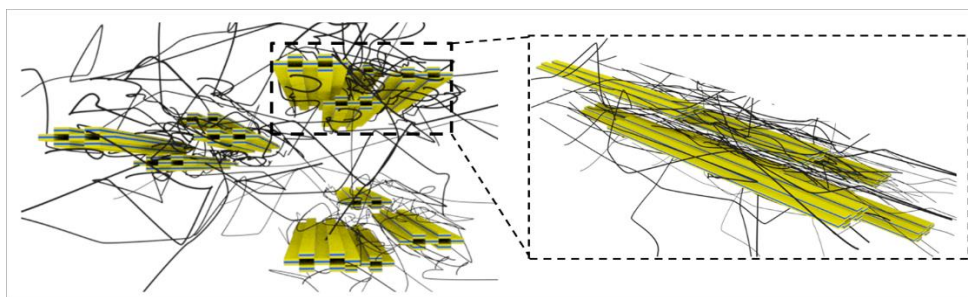


Fig 3.22 TEM images at different magnifications of (a, a') V-SepB5/SBR, (b, b') V-NS-SepB5/SBR, (c, c') V-NS-SilSepB5/SBR

It's interesting to note that the surface modification and the decrease in particle size obtained by the acid treatment are triggering off the filler network self-assembly. Self-assembly of particles is as an important process where the building blocks spontaneously organize into ordered structures and it is promoted by different constraints[31].

In rubber-like materials, the filler self-assembly depends on the competition and delicate balance between two opposite actions: on one hand the hydrophilic particle cores tend to contact each other to shield themselves from organic matrix, on the other hand they interact with polymeric chains thanks to the presence of silane functional groups[32]. The particle shape as well as their interaction with polymer chains determine the ordered structures in which they can assemble.

Evidently, the particles have to be small enough to physically align and accommodate within the hosting polymeric architecture, so consideration of the components size is an important criterion. In this respect, TEM analysis of V-NS-SepX/SBR and V-NS-SilSepX/SBR strongly suggests that only the Sep fibers, which are interfacially activated and display reduced particle dimensions, succeed to align and yield strong specific interactions which permit to the polymer chains to efficiently diffuse into the interspace of the modified fibers. This disrupts the tactoids interaction and favors the filler network self-assembly, as shown in the Scheme 3.1.



Scheme 3.1 Schematic representation of self-assembly of NS-SepX/SBR and NS-SilSepX/SBR.

The existence of the filler network self-assembly agrees with the reported mechanical performance. In fact, the pristine SepS9 and SepB5 do not show a significant reinforcement effect (respect to nanosilica, in Table 3.9), as it would be expected on the basis of their high AR.1 Moreover, despite the good distribution of the SepS9 and SepB5, as shown in the TEM images (a in Fig. 3.20 and 3.22), the filler-rubber interaction of corresponding nanocomposites is low even in presence of the TESPT compatibilizer.

On the contrary, although the fibers distribution appears not homogeneous and discontinuous (b and c in Fig. 3.20 and 3.22), the NS-SepX and NS-SilSepX produce a slightly higher value of reinforcement indicator ($G'(9\%)$) and an improved hysteretic behavior. It is evident that the continuous percolative network of Sep fiber (b' and c' in Fig. 3.20 and 3.22), connected by thin polymer films, is dominant in determining the high performance of investigated composites. More in depth, the percolating network structures are observed only in the presence of fibers with specific size and surface functionality, obtained by a controlled acid treatment and therefore able to self-assemble.

While filler homogenous distribution is believed to critically affect mechanical properties, we here found that it is the self-assembly into highly anisotropic structures which optimizes the macroscale properties, if such organization is repeated in a continuous manner throughout the polymer matrix. It is suggested that the design of high performance materials requires excellent control over filler spatial distribution.

3.2.4 Analysis of immobilized rubber at filler/rubber interface by TD-NMR

Low field ^1H NMR measurements of filled SBR composite and of the unfilled reference were used to investigate the mobility of rubber chains and the effect in the mobility induced by the presence of both pristine and modified Sep.

NMR study was based on measurements of ^1H spin spin relaxation times (T_2) A complete characterization of the dynamic properties of the obtained materials could be achieved combining SE and CPMG experiments. SE was used to refocus the signal from dipolar-coupled protons in rigid domains characterized by very short T_2 (typically on the order of 10-20 μs), which would otherwise decay during the instrumental dead time. On the other hand, CPMG experiments were exploited to accurately measure the intrinsic T_2 relaxation times of the long-decaying liquid-like components of the FID, which can be affected by non-dynamic contributions, such as magnetic susceptibility of the sample and/or fluctuations and inhomogeneity of the external magnetic field.

The discrete analysis of a ^1H FID recorded on resonance by SE allows domains with different degree of mobility to be identified and quantified. The ^1H FID is fitted to a linear combination of functions (f_i), each characterized by a spin-spin relaxation time T_{2i} and a weight percentage w_i . The value of T_{2i} , out of the so-called rigid lattice regime, monotonically increases with the increase of mobility, while w_i is related to the percentage of protons belonging to the i -th domain [33]. Since in the presence of multiple ^1H - ^1H dipolar interactions the efficiency of SE progressively brakes down by increasing the echo delay (ED), quantitative values of w_i can be determined by performing SE experiments at different echo delays and extrapolating the intensity of each component f_i to a zero delay. For all the samples, the experimental ^1H FID's were well reproduced with a linear combination of two exponential and one Gaussian functions, as shown, as an example, in Fig. 3.23a for sample V-NS-SilSepS9/SBR. The Gaussian function

(Gau) is characterized by a very short T_2 of $\sim 20 \mu\text{s}$ typical of protons located in rigid solid-like environments, and could arise not only from rigid SBR domains but also from protons located in sepiolite particles. It is worth noticing that the rigid SBR domains can include immobilized rubber at the SBR/filler interface as well as entangled and crosslinked rubber chains [34].

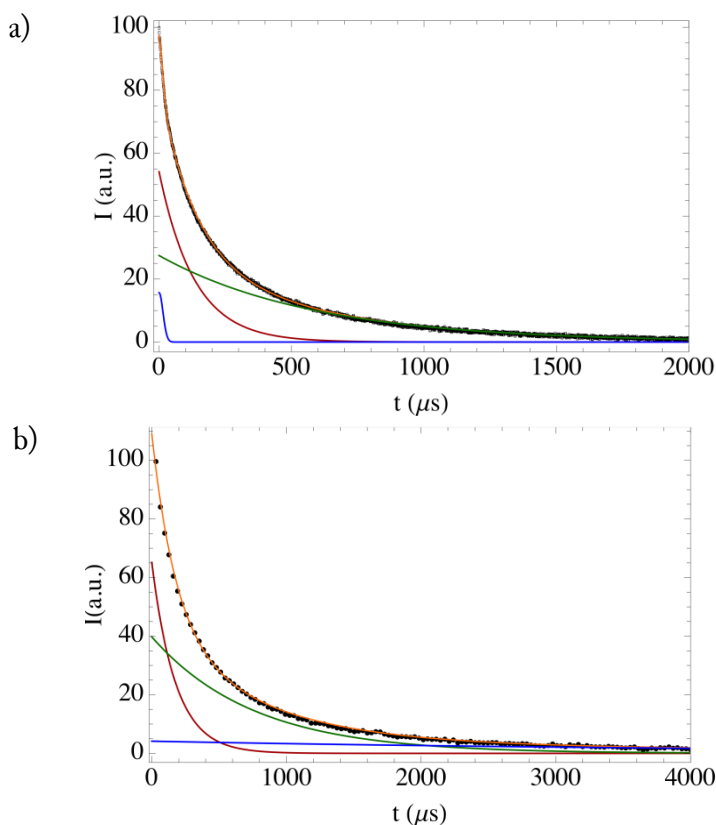


Figure 3.23 (a) Fitting of the on-resonance ^1H FID (dotted line) recorded by SE for sample V-NS-SilSepS9/SBR. The fitting function (orange line) and the single contributions of the Gaussian (blue line), short- T_2 (red line) and long- T_2 (green line) exponential components are shown. (b) Fitting of the CPMG relaxation curve (dotted line) recorded for sample V-NS-SilSepS9/SBR. The fitting function (orange line) and the single contributions of the three exponential components, exp1 (red line), exp2 (green line) and exp3 (blue line), are shown.

On the other hand, the two exponential functions, representing from 84 to 95 % of the ^1H FID, are characterized by long liquid-like T_2 values in the ranges 150–250 and 500–800 μs , and are ascribable to protons in very mobile environments and/or to isolated hydroxyl groups of the filler. A more accurate description of the T_2 relaxation behaviour of these long-decaying components was obtained from the analysis of CPMG relaxation curves. In all cases, the CPMG curves could be well fitted by a linear combination of three exponential functions, here indicated as exp1, exp2 and exp3, where T_2 increases in going from exp1 to exp3. In particular, T_2 values of ~ 300 , ~ 1200 , and ~ 6500 μs and of 130–180, 580–760 and 3400–4500 μs were found for the uncured and vulcanized samples, respectively. An example of fitting is shown in Fig. 3.23b. These three exponential components provide a more complete and reliable picture of the non-rigid environments present in the samples. In particular, exp1 and exp2 indicate the presence of a distribution of mobile environments with different mobility, mainly ascribable to the SBR matrix, while exp3 can be assigned to SBR free chain ends. The decrease of the T_2 values observed in passing from uncured to vulcanized samples is in agreement with a decrease of mobility of the rubber chains due to the formation of cross-links induced by vulcanization. In Table 3.10 the weights w_i of the different protons fractions obtained combining SE and CPMG experiments are reported. The shortest- and longest- T_2 exponential components of the ^1H FID's recorded by SE were assumed to correspond, respectively, to exp1 and to the sum of exp2 and exp3.

Table 3.10 Weight percentages (w_i) of the proton fractions located in regions with different degree of mobility obtained for the investigated samples combining SE and CPMG experiments as described in the text. The sum of the weights of exp2 and exp3 components was taken as that of the longest exponential component determined by SE, while the ratios between exp2 and exp3 weights were obtained from CPMG curves.

Solid echo / CPMG w_i (%)				
Sample	Gau	exp1	exp2	exp3
SBR-REF-0	6	52	37	5
SepS9/SBR	9	48	39	4
NS-SepS9/SBR	10	49	36	5
NS-SilSepS9/SBR	12	48	35	5
SepB5/SBR	10	44	40	6
NS-SepB5/SBR	10	52	34	4
NS-SilSepB5/SBR	13	51	32	4
V-SBR-REF-0	12	60	25	3
V-SepS9/SBR	13	57	27	3
V-NS-SepS9/SBR	13	58	26	3
V-NS-SilSepS9/SBR	19	57	22	2
V-SepB5/SBR	13	49	33	5
V-NS-SepB5/SBR	15	62	20	3
V-NS-SilSepB5/SBR	19	57	21	3

The increase of the weight percentage of exp1 with respect to exp2 in passing from the uncured to the vulcanized samples further confirms the reduced mobility of SBR chains after vulcanization. On the other hand, only slight changes of the weights of the different exponential components were observed in passing from pure SBR to the SBR/sepiolite composites, indicating that the presence of the sepiolite particles does not significantly influence the mobility of rubber chains, which are not directly involved in the interaction at the SBR/filler interface.

Table 3.11 Molar percentages (%H) of ^1H nuclei belonging to the filler ($f_{\text{H}}^{\text{Sep}}$) and of ^1H nuclei in rigid environments, as determined by FID analysis using the procedure described in the text. $f_{\text{Hrigid}}^{\text{TOT}}$ is the total fraction of protons in rigid environments, while $f_{\text{Hrigid}}^{\text{Sep}}$ and $f_{\text{Hrigid}}^{\text{SBR}}$ are the fractions of filler and rubber protons in rigid environments, relative to the whole composite, respectively. $f_{\text{Hrigid}}^{\text{SBR}^*}$ is the fraction of rubber protons in rigid environments relative to the sole SBR component.

Sample	%H relative to the composite				%H relative to SBR only
	$f_{\text{Hrigid}}^{\text{TOT}}$	$f_{\text{H}}^{\text{Sep}}$	$f_{\text{Hrigid}}^{\text{Sep}}$	$f_{\text{Hrigid}}^{\text{SBR}}$	$f_{\text{Hrigid}}^{\text{SBR}^*}$
SBR-REF-0	6	-	-	6	6
SepS9/SBR	9	4	2	7	7
NS-SepS9/SBR	10	4	1	9	9
NS-SilSepS9/SBR	12	6	3	9	10
SepB5/SBR	10	5	2	8	8
NS-SepB5/SBR	10	7	1	9	10
NS-SilSepB5/SBR	13	6	4	9	10
V-SBR-REF-0	12	-	-	12	12
V-SepS9/SBR	13	4	2	11	11
V-NS-SepS9/SBR	13	4	1	12	13
V-NS-SilSepS9/SBR	19	6	3	16	17
V-SepB5/SBR	13	5	2	11	12
V-NS-SepB5/SBR	15	7	1	14	15
V-NS-SilSepB5/SBR	19	6	4	15	16

As already stated, for the SBR/sepiolite composites the weight of the Gaussian component ($f_{\text{Hrigid}}^{\text{TOT}}$) accounts for all protons in rigid environments, from both rubber domains with restricted mobility and the filler. In order to investigate the influence of the different sepiolite fibers in the formation of a surface-immobilized rubber layer (physical absorption and chemical bond of rubber on filler surface) at the SBR/filler interface it was therefore necessary to separate these two contributions by determining the fraction of rigid protons belonging to the filler ($f_{\text{Hrigid}}^{\text{Sep}}$). To this aim, the following methodological approach was applied, in agreement of some authors [24]:

- 1) a calibration curve was built using weighted standard samples with known hydrogen contents, where the total ^1H FID intensity to sample weight ratio was plotted against the hydrogen weight percentage (% wt/wt) (Table A1 and Figure A1 in the Appendix);
- 2) the total hydrogen content (% wt/wt) in each type of filler was determined by interpolating the calibration curve, after measuring the total ^1H FID intensity of weighted pure sepiolite samples (Table A2 in the Appendix);
- 3) the ^1H FID's recorded for the pristine Sep fillers were then analysed in order to evaluate the fraction of protons in rigid environments (Table A2 in the Appendix);
- 4) knowing the amount of filler in the composite samples, the fraction of protons from rigid rubber ($f_{\text{Hrigid}}^{\text{SBR}}$) was calculated as $f_{\text{Hrigid}}^{\text{TOT}} - f_{\text{Hrigid}}^{\text{Sep}}$.¹

¹ It is worth noticing that in order to calculate f_{H}^{ep} in the composite samples the presence of TDAE extender oil in the amount of 37.5 phr had to be taken into account. Since the exact composition of TDAE, containing aromatic, naphthalenic and paraffinic components, is not known, an average hydrogen content of 10 % (H%, wt/wt), similar to that of SBR, was assumed for this oil. It was also verified that by varying H% in the range 9-11% the calculated values of the different proton fractions remain within the experimental error. Moreover, since TDAE was added in the same amount to all the samples, its contribution does not substantially affect the differences in terms of amount of rigid rubber observed among the samples.

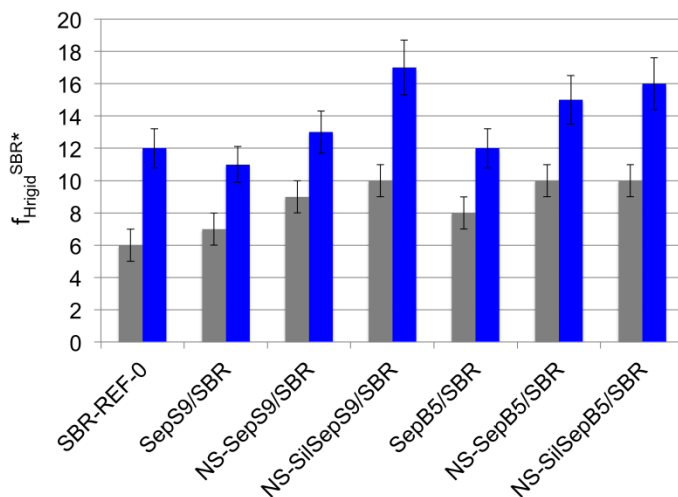


Figure 3.24 Fraction of rigid rubber (f_{Hrigid}^{SBR*} , %) determined for the uncured (gray) and vulcanized (blue) samples from the analysis of 1H FID's, as described in the text.

The final results are reported in Table 3.11 and Fig. 3.24. First, it can be noticed that the percentage of rigid SBR is significantly larger in vulcanized (11-17%) than in uncured samples (6-10%). This result was expected and could be explained with a higher amount of "immobilized" rubber chains in correspondence of the cross-links formed as a consequence of vulcanization.

In Fig.3.24, it is evidenced that filling with both pristine SepX has virtually no effect on the rubber matrix. Only a slight shift of the cross-link density to lower values is seen, which can be explained by inactivation of parts of the vulcanization system by adsorption to the high-surface filler, leading to somewhat lower cross-link densities. In addition, it can be noticed that no significant improvements in terms of immobilized rubber layer formation was obtained by using the organically modified SepB5 sepiolite with respect to SepS9.

Thus, NMR analysis indicates that the a significant effect of pristine Sep on the cross-link density in the interface is not detectable. This result clearly reveals that pristine particles do not significantly interact with the rubber matrix, no matter whether they are better dispersed, as in the case of organoclay SepB5 or not (SepS9).

Moreover, for both uncured and vulcanized samples the fraction of rigid rubber was found to slightly increase in passing from pure SBR to the NS-Sep/SBR composites. Assuming that a possible contribution from entangled rubber chains does not significantly change among the samples, this increase can be entirely ascribed to the formation of immobilized rubber at the interface with the filler. In particular, SSNMR results indicate that surface-immobilized rubber layer forms only in the presence of both modified NS-SepX and NS-SilSepX fillers, while for composites with untreated sepiolite fillers (SepB5 and SepS9) the fraction of rigid rubber did not significantly vary with respect to pure SBR (Fig. 3.24). The surface-immobilized rubber layer of composites containing modified Sep is about 1-4% of total rubber. Although this surface-immobilized rubber layer is only a small fraction of the entire polymer matrix, its influence on mechanical properties can be tremendous since the immobilized rubber layer is possibly important for the percolation and the morphology of the solid phase [35].

Therefore, the modified Sep is able to create some interfacial phenomena, in terms of filler/rubber interactions that affect the entire bulk, as suggest by the improvement of hysteretical behavior of NS-Sep nanocomposites (see Paragraph 3.2.1). An immobilized rubber layer could consistently explain the strain independence of storage modulus of NS-Sep composites (Figure 3.14 and 3.15). Up to now, it is reported that clay particles, even if exfoliated and well dispersed are not able to significantly interact with the rubber matrix. In fact, the reinforcement effects in rubber-clay nanocomposites, achieved without chemical or physical bonds between polymer and filler, has been mainly attributed to geometric effect of stiff and well-dispersed filler particles. In other words, the reinforcement mainly benefits from the increased modulus of the percolated mechanical network as compared to the soft matrix [36]

On the contrary the modification of the Sep fibers introduces a better interaction with the matrix and the formation of immobilized rubber, as demonstrated by

NMR, reducing the dissipative process in the rubber nanocomposites, as result by the DMTA analysis (see Paragraph 3.2.1).

In addition, the self-assembly of nanosized Sep particles allows the organization of anisotropic fibers in filler superstructures where rubber chains are immobilized in the inter-particle region

3.3. TC Sep Nanocomposite

The NS-SepS9 and NS-SepB5 fibers were also formulated in TC for vulcanisable elastomeric materials of internal tyre components, suitable for various applications, such as elastomeric under-layer materials (car and heavy vehicles), soft bead (heavy vehicles), sidewall insert (car), or sidewall.

These materials, namely V-NS-SepS9/TC and V-NS-SepB5 /TC were compared with reference elastomeric materials, V-SiO₂/TC, comprising standard silica as filler. The TC elastomeric materials were subjected to measurement of the static and dynamic mechanical properties, resumed in Table 3.10.

As a formulation is here concerned, 7 phr of NS-SepX were substituted with 10 phr of silica in order to compare compounds with similar stiffness, measured as dynamic compression modulus E' at 70 °C. The analysis of the data in Table 3.10 shows that the incorporating of both NS-SepS9 and NS-SepB5 in the elastomeric material, in replacement of an aliquot of silica, produced satisfactory elongation without affecting tensile strength. For both V-NS-SepX/TC composites, σ 100% increase of more than 20% with respect to reference at comparable value of tensile strength. This effect can be tentatively explained in terms of a strain induced fiber alignment that is known to affect nanocomposites stiffness under tensile strain [37]. Above all, the dissipative properties, measured as Tan Delta in compressive test improve drastically. In fact, the tan delta at 70 °C is lower than 25% in the compression test in the case of NS-SepS9 and NS-

SepB5. This result is even more significant considering that the composition was modified by less than 6% by weight. The TC-samples with NS-SilSepS9 and NS-SilSepB5 (data not shown) confirmed the same dynamic-mechanical behavior.

Table 3.10. Dynamic-mechanical characterization of TC Sep nanocomposites.

	V-SiO ₂ / TC	V-NS-SepS9/TC	V-NS-SepB5 /TC
Traction			
σ 50% ^a [MPa]	1.99	2.51	2.47
σ 100% ^a [MPa]	4.05	5.44	5.42
Tensile strength [MPa]	12.33	12.27	12.58
Elongation at break (%)	255.0	199.70	191.99
Hardness			
IRHD ^b 23 °C	72.8	72.4	72.4
IRHD 100 °C	71.6	71.7	71.7
Dynamic compression			
E' [MPa] ^a 23 °C 100 Hz	9.22	8.55	8.65
70 °C 100 Hz	8.97	8.65	8.66
T. DELTA ^d 23 °C 100 Hz	0.104	0.075	0.074
70 °C 100 Hz	0.069	0.052	0.050

^a σ 50% and σ 100% tensile modulus at 50% and 100% deformation, respectively; ^b IRHD International Rubber Hardness Degrees; ^c E' dynamic elastic modulus; ^d T. DELTA (loss factor) calculated as the ratio between in terms of dynamic elastic modulus (E').

In summary, from the dynamic-mechanical analyses performed on the nanocomposites, it is clear that the presence of NS-Sep fibers generated by the acid treatment, decreases the hysteresis of the elastomeric materials while maintaining a good reinforcement [38].

3.4 Bibliography

- [1] A. Yebra-Rodríguez, F. D. R. Martín-Ramos, C. Viseras, and A. Lopez-Galindo, "Effect of acid treatment on the structure of sepiolite," *Clay Miner.*, vol. 38, no. 3, pp. 353–360, 2003.
- [2] L. G. Hernandez, L. I. Rueda, and A. R. Diaz, "Preparation of Silica by Acid Dissolution of Sepiolite and Study of its Reinforcing Effect in Elastomers," vol. 103, no. 1579, pp. 51–60, 1982.
- [3] E. Galan, "Properties and Applications of Palygorskite-Sepiolite Clays," *Clay Miner.*, vol. 31, no. 4, pp. 443–453, 1996.
- [4] N. García *et al.*, "Surface modification of sepiolite in aqueous gels by using methoxysilanes and its impact on the nanofiber dispersion ability," *Langmuir*, vol. 27, no. 7, pp. 3952–3959, 2011.
- [5] J. E. Post and P. J. Heaney, "Synchrotron powder X-ray diffraction study of the structure and dehydration behavior of palygorskite," *Am. Mineral.*, vol. 93, no. 4, pp. 667–675, 2008.
- [6] J. Cornejo and M. C. Hermosin, "Structural alteration of sepiolite by dry grinding," *Clay Miner.*, vol. 23, pp. 391–398, 1988.
- [7] H. H. W. Moenke, *Silica, the Three-dimensional Silicates, Borosilicates and Beryllium Silicates*, V. C. Farm. London, 1974.
- [8] M. A. Vicente-Rodríguez, M. Suarez, M. A. Bañares-Muñoz, and J. de Dios Lopez-Gonzalez, "Comparative FT-IR study of the removal of octahedral cations and structural modifications during acid treatment of several silicates," *Spectrochim. Acta Part A Mol. Biomol. Spectrosc.*, vol. 52, no. 13, pp. 1685–1694, 1996.
- [9] P. Komadel, "Structure and Chemical Characteristics of Modified Clays," in *Natural Microporous Materials in Environmental Technology*, vol. 362, P. Misaelides, F. Macásek, T. J. Pinnavaia, and C. Colella, Eds. Dordrecht: Springer Netherlands, 1999, pp. 3–18.
- [10] M. R. Weir, W. Kuang, G. A. Facey, and C. Detellier, "Solid-state nuclear magnetic resonance study of sepiolite and partially dehydrated sepiolite," *Clays Clay Miner.*, vol. 50, no. 2, pp. 240–247, 2002.
- [11] J.-B. D. de la Caillerie and J. J. Fripiat, "A Reassessment of the ^{29}Si Mas-Nmr Spectra of Sepiolite and Aluminated Sepiolite," *Clay Miner.*, vol. 29, pp. 313–318, 1994.

- [12] M. a Aramendía, V. Borau, C. Jiménez, J. M. Marinas, and J. R. Ruiz, "Characterization of Spanish sepiolites by high-resolution solid-state NMR.," *Solid State Nucl. Magn. Reson.*, vol. 8, no. 4, pp. 251–6, 1997.
- [13] I. Dékány, L. Turi, A. Fonseca, and J. B. Nagy, "The structure of acid treated sepiolites: small-angle X-ray scattering and multi MAS-NMR investigations," *Appl. Clay Sci.*, vol. 14, no. 1–3, pp. 141–160, 1999.
- [14] C. Breen, R. Watson, J. Madejova, and P. Komadel, "Acid-Activated Organoclays : Preparation , Characterization and Catalytic Activity of Acid-Treated Tetraalkylammonium-Exchanged Smectites," *Langmuir*, vol. 13, no. 24, pp. 6473–6479, 1997.
- [15] M. Suárez and E. García-Romero, "Variability of the surface properties of sepiolite," *Appl. Clay Sci.*, vol. 67–68, pp. 72–82, 2012.
- [16] S. Brunauer, L. S. Deming, W. E. Deming, and E. Teller, "On a Theory of the van der Waals Adsorption of Gases," *J. Am. Chem. Soc.*, vol. 62, no. 7, pp. 1723–1732, 1940.
- [17] B. C. Lippens and J. H. de Boer, "Studies on pore systems in catalysts: V. The t method," *J. Catal.*, vol. 4, no. 3, pp. 319–323, 1965.
- [18] K. S. W. Sing, "Reporting physisorption data for gas/solid systems with special reference to the determination of surface area and porosity (Recommendations 1984)," *Pure Appl. Chem.*, vol. 57, no. 4, pp. 603–619, Jan. 1985.
- [19] M. A. Vicente Rodríguez, J. de D. González Lopez, and M. A. Muñoz Banares, "Acid Activation of a Spanish Sepiolite: Physicochemical Characterization, Free Silica Content and Surface Area of Products Obtained," *Clay Miner.*, vol. 29, pp. 361–367, 1994.
- [20] R. N. Hakim and H. Ismail, "The Comparison of Organoclay with Respect to Silica on Properties of Natural Rubber Nanocomposites," *J. Reinf. Plast. Compos.*, vol. 28, no. 12, pp. 1417–1431, 2009.
- [21] A. R. Payne, "The dynamic properties of carbon black loaded natural rubber vulcanizates. Part II," *J. Appl. Polym. Sci.*, vol. 6, no. 21, pp. 368–372, 1962.
- [22] G. Heinrich and M. Klüppel, *Recent Advances in the Theory of Filler Networking in Elastomers*. .
- [23] R. Scotti *et al.*, "Shape controlled spherical (0D) and rod-like (1D) silica nanoparticles in silica/styrene butadiene rubber nanocomposites: Role of the particle morphology on the filler reinforcing effect," *Polym. (United Kingdom)*, vol. 55, no. 6, pp. 1497–1506,

- Mar. 2014.
- [24] L. Tadiello *et al.*, “The filler–rubber interface in styrene butadiene nanocomposites with anisotropic silica particles: morphology and dynamic properties,” *Soft Matter*, vol. 11, p. , 2015.
- [25] M. P. Sepe, *Dynamic Mechanical Analysis for Plastics Engineering*, vol. 20, no. 12. 1998.
- [26] P. Joseph, G. Mathew, K. Joseph, G. Groeninckx, and S. Thomas, “Dynamic mechanical properties of short sisal fibre reinforced polypropylene composites,” *Compos. Part A Appl. Sci. Manuf.*, vol. 34, pp. 275–290, 2003.
- [27] M. Poletto and a. J. Zattera, “Mechanical and dynamic mechanical properties of polystyrene composites reinforced with cellulose fibers: Coupling agent effect,” *J. Thermoplast. Compos. Mater.*, pp. 1–13, 2015.
- [28] K. P. Menard, *Dynamic Mechanical Analysis: A Practical Introduction, Second Edition*. 2008.
- [29] W. E. Geiger, “Re V iews,” *Organometallics*, vol. 26, pp. 5738–5765, 2007.
- [30] E. K. Hobbie, “Shear rheology of carbon nanotube suspensions,” *Rheol. Acta*, vol. 49, no. 4, pp. 323–334, 2010.
- [31] M. Grzelczak, J. Vermant, E. M. Furst, L. M. Liz-Marzán, and L. M. Liz-marza, “Directed self-assembly of nanoparticles.,” *ACS Nano*, vol. 4, no. 7, pp. 3591–605, 2010.
- [32] R. H. C. & J. F. D. Pinar, Akcora, Hongjun Liu, Sanat K. Kumar, Joseph Moll, Yu Li, Brian C. Benicewicz, Linda S. Schadler, Devrim Acehan, Athanassios Z. Panagiotopoulos, Victor Pryamitsyn, Venkat Ganesan, Jan Ilavsky, Pappanan Thiyagarajan, “Anisotropic self-assembly of spherical polymer-grafted nanoparticles,” *Nat. Mater.*, vol. 8, pp. 354–359, 2009.
- [33] E. W. Hansen, P. E. Kristiansen, and B. Pedersen, “Crystallinity of Polyethylene Derived from Solid-State Proton NMR Free Induction Decay,” *J. Phys. Chem. B*, vol. 102, no. 98, pp. 5444–5450, 1998.
- [34] S. Schlögl, M. L. Trutschel, W. Chassé, G. Riess, and K. Saalwächter, “Entanglement effects in elastomers: Macroscopic vs microscopic properties,” *Macromolecules*, vol. 47, no. 9, pp. 2759–2773, 2014.
- [35] J. Y. Ko, K. Prakashan, and J. K. Kim, “New silane coupling agents for silica tire tread compounds,” *J. Elastomers Plast.*, vol. 44, no. 6, pp. 549–562, 2012.
- [36] D. W. Schaefer and R. S. Justice, “How nano are nanocomposites?,” *Macromolecules*,

vol. 40, no. 24, pp. 8501–8517, 2007.

- [37] M. Okamoto *et al.*, “Biaxial Flow-Induced Alignment of Silicate Layers in Polypropylene/Clay Nanocomposite Foam,” *Nano Lett.*, vol. 1, no. 9, pp. 503–505, 2001.
- [38] L. Giannini *et al.*, “Vulcanisable elastomeric materials for components of tyres comprising modified silicate fibres, and tyres thereof,” 2016.

4

Sep *Ionomer* Nanocomposites by Solution Mixing: Results and Discussion

The current chapter describes the results concerning Sep ionomer NCs, obtained by solution mixing of modified Sep and SBR with functional groups that can be positively or negatively ionized in aqueous solution.

Firstly, the complete characterization of the modified N'SepS9 and SSBR will be reported followed by the morphological and mechanical characterization of the Sep ionomer NCs in order to verify the effect ionic filler-rubber in the elastomer materials.

4.1 Ionic interaction in PNCs

Polymers composed of macromolecules in which a small but significant proportion of the constitutional units have ionic or ionizable groups, **or both**, are called ionomers [1], [2]. Usually they have a relatively small number of ionic groups (up to 10–15 mol%) distributed along non-ionic organic backbone. By controlling the ion content, degree of neutralization, nature of counter ion and additives it is possible to prepare materials with a wide range of properties [3]–[6]. These ionic domains can act as **physical crosslink** (Fig. 4.1).

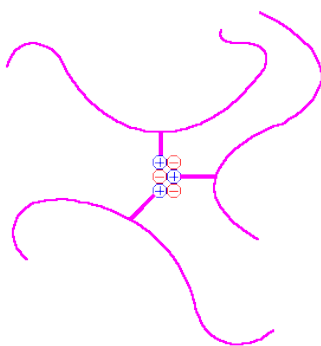


Figure 4.1. Schematization of the ionic interaction in ionomers

Most of the ionomers synthesized have carboxylate, sulfonate, phosphate and phosphonates as pendent anions.

The use of ionomers is an effective approach to modify various polymer properties, such as glass transitions, size and distribution of domains dispersed in the continuous polymer matrix, miscibility between different polymers, melt rheology and mechanical properties. This is because the ionic interactions are strong and can cause significant morphological changes and modifications of physical properties of NCs.

Recently, the ionic bond has been considered especially intriguing to overcome some issues of PCN preparation, such as the control of both arrangement and dispersion of NPs in polymer matrix in order to improve the properties of PNCs.

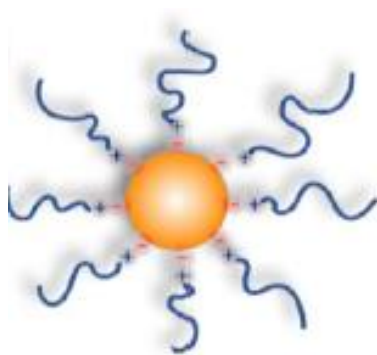


Figure 4.2. Schematic representation of the use of ionic interaction with NPs [7].

One approach that has met with some success is functionalizing the surface of the NPs with brushes of grafted polymer chains forming a canopy around the particle (Fig. 4.2). Since the first demonstration by Bourlinos et al. [8] in 2005, a wide gallery of materials have been synthesized, and a large range of synthetic techniques to form the central ionic bond have been investigated. In this contest, Giannelis et al. reported the preparation of novel Nanoscale Ionic materials (NIMs, Fig. 4.3) comprising a charged nano-sized particle core and an oppositely charged canopy formed through ionic coupling [7].

NIMs exhibit additional dispersion stability due to electrostatic repulsion between particles, both during the synthesis and assembly stages, as well as in the final material. Additionally, the dynamic nature of the ionic links introduces structural and dynamic behavior, which has parallels to ionic liquids and ionomers. In these materials, the ionic motif is the base of the design platform that provides a versatility and a unique set of properties that open up a wide range of applications. For example, silica-based NIMs used as thickeners in traditional lubricating oils has created materials whose mechanical moduli and viscosity can be tuned over a wide range [9].

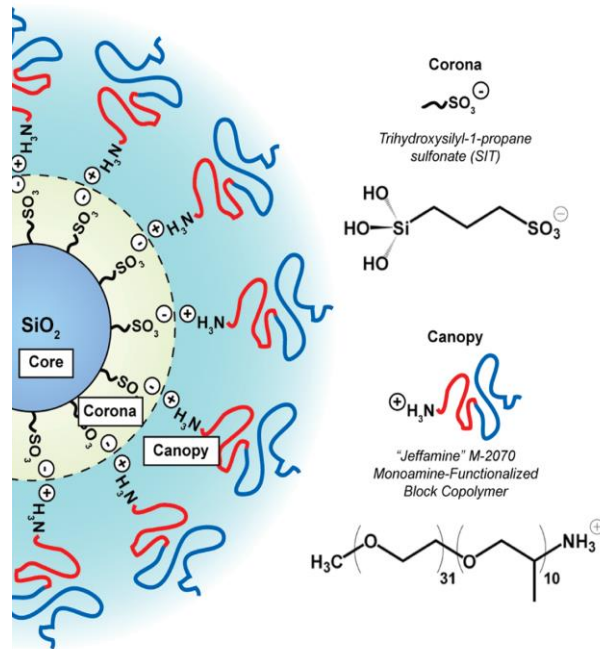


Figure 4.3. Schematic illustration of the NIM.

In line with NIM philosophy and in collaboration with Prof. Giannelis, a new approach was investigated to promote the Sep-rubber interaction by an ionic interaction between filler-rubber. The new approach consists of the functionalization of SepS9 and SBR with functional groups, amino-silane and sulfonate group respectively, that can be positively or negatively ionized in aqueous solution and interact by ionic bonds (Fig. 4.4). The strength of ionic interaction may permit a very strong bond to be created between the sulfonic group and the counter ion present in the Sep nanofibers and consequently an increase in the filler-polymer interaction

A complete characterization of the modified Sep and SBR was performed, while the Sep NCs was preliminary investigated by TEM and static-dynamic analyses. Moreover, self-assembly ability of N'SepSep on rubber matrix was investigated and related to both filler network structures and mechanical properties of obtained NCs.

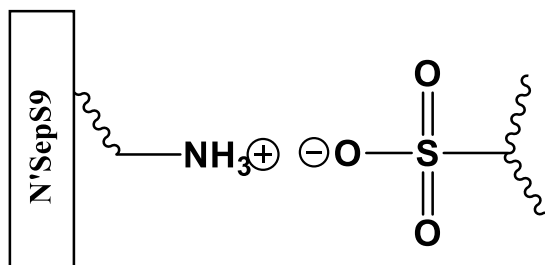


Figure 4.4. Schematic representation of ionic interaction between SSBR and N'SepS9

It is worthy to note that this approach eliminates the need to use compatibilizers and coupling agents with an obvious advantage in the tire industry, lowering the cost of production.

4.2 Chemical and morphological characterization

4.2.1 Characterization of SSBR by FT-IR spectroscopy

The obtained polymer SSBR was characterized by FTIR and compared with the pristine SBR (Fig. 4.5). In the spectra, FTIR evidences: i) the adsorption bands at 2920 cm^{-1} and 2848 cm^{-1} , corresponding to the stretching vibrations of C-H bond of CH_2 butadiene groups, ii) the band at 1600 cm^{-1} corresponds to the C=C stretching of phenyl group, iii) the peak at 966 cm^{-1} of the C=C bond attributable to butadiene backbone.

In the SSBR spectrum, the presence of new peaks at 1195 (a) and 1168 (b) cm^{-1} , attributable to O=S=O stretching of sulfonic acid group, confirms the occurred functionalization. In addition, SSBR shows a noticeable decrease in the relative intensity of the C=C stretching (966 cm^{-1}) suggesting that the sulfonic acid groups are preferentially introduced into the butadiene unit, rather than in the styrene units [10].

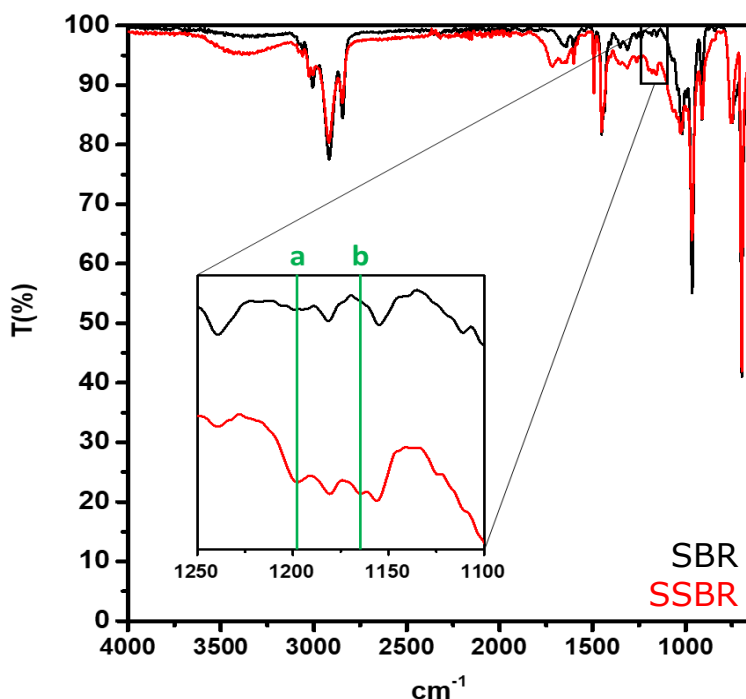


Fig 4.5 FT-IR spectra of the control styrene butadiene rubber (black) and the sulfonated styrene butadiene rubber.

4.2.2 Characterization of *N*'SepS9 by ^{29}Si NMR

Figure 4.6 shows the CPMAS NMR spectra of pristine SepS9, SepS9-OH, after basic treatment and *N*'SepS9 and the relative data are presented in Table 4.1.

As previously described (Paragraph 3.1.4 of Chapter 3) pristine SepS9 presents four types of silicon atoms, three Q^3 and one Q^2 . Q^3 Si atoms refers to silicon atoms attached to three other silicon atoms through oxygen atoms, while Q^2 represents silicon atoms attached to two other silicon atoms through oxygen atoms. Pure SepS9 shows three well resolved resonance of approximately equal intensity for the Q^3 atoms at -92.7 (Si2), -94.3 (Si3) and -98.2 ppm (Si1) [11],[12], a small signal at around -83 ppm attributed to the Q^2 Si unit, and a very low broad shoulder whose chemical shift corresponds to Q^4 units, such as amorphous silica.

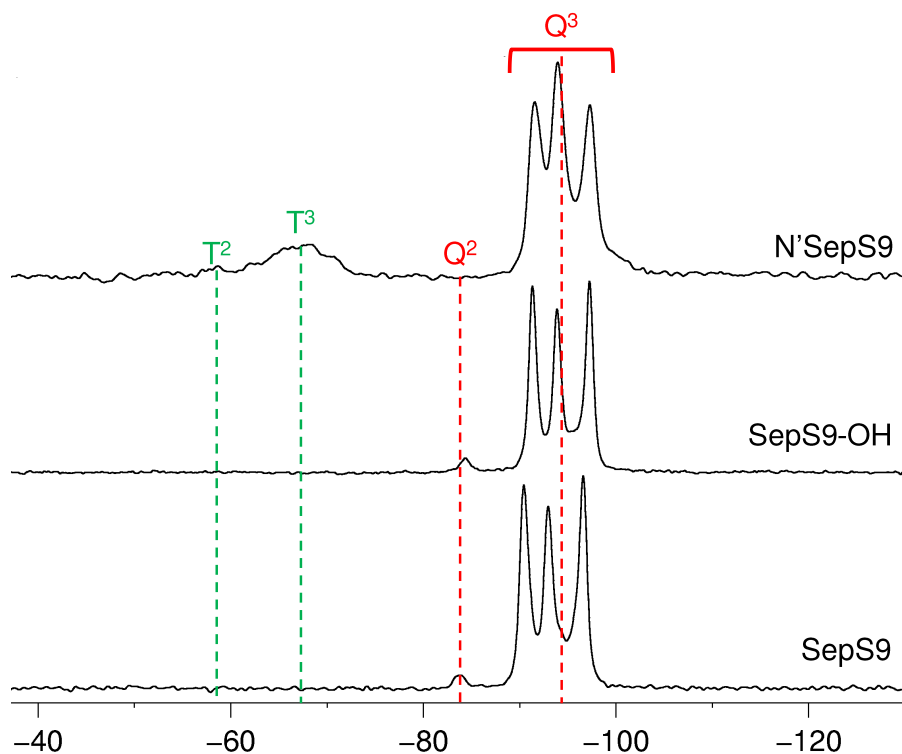


Figure. 4.6 ^{29}Si CPMAS NMR spectra of (a) SepS9 sample, (b) SepS9-OH, (c) N'SepS9.

The preliminary basic treatment of the Sep (SepS9-OH) does not cause appreciable changes in the SepS9 structure. A slight up-field shift of 0.4 ppm can be seen for Si^2 , near the edge and the central Si^3 , probably due to the partial Mg substitution.

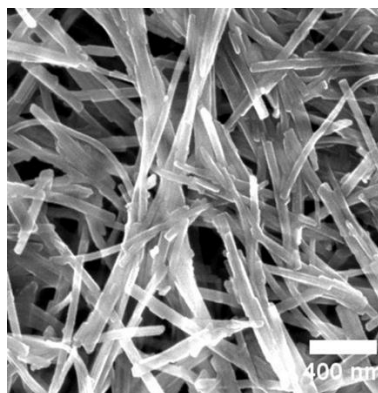
The silanization reaction with (N'SepS9) does not influence the SepS9 structure but reduces the Q^2 resonance and causes the appearance of the typical trifunctional group of Si at -58.4 and -67.0 ppm, correlated to the T^2 and T^3 units. They account for 12.1% with respect to the SepS9 peaks calculated by DOC (Eq. 3.1).

Table 4.1 ^{29}Si NMR chemical shifts δ (ppm), assignment and amount.

Si units	SepS9	SepS9-OH	N'SepS9
T ²			-58.4
T ³			-67.0
Q ²	-83.6	-83.9	
Q ³ (1Mg) Si2	-90.4	-90.9	-91.1
Q ³ (1Mg) Si3	-92	-93.5	-93.5
Q ³ (1Mg) Si3	-94.3		
Q ³ (1Mg) Si1	-95.6		
Q ³ (1Mg) Si1	-96.6	-96.8	-96.9
Q ³			-100.0
Q ⁴			
T/Q			12.1/100

4.2.3 Morphological investigation of N'SepS9 by SEM

The morphology of modified N'SepS9 was investigated by SEM. In Fig 4.7, SEM image shows the characteristic fibrous morphology of the Sep NPs.

**Figure 4.7** SEM micrograph of N'SepS9

N'SepS9 sample presents needle-like morphology with diameter of 20-30 nm and length of 1-1.5 μm in length on average, similar to the characteristic parameters of pristine SepS9. The expected coating on surface fibers due to the functionalizing silane, can be attributed to lower degree of functionalization, as confirmed by NMR analysis.

4.3 Sep Ionomer NC characterization

N'SepS9 was used to prepare the nanocomposite, namely N'SepS9-SSBR by solution mixing with the sulfonated SBR. Dynamic-mechanical and tensile test were performed in order to study the filler-filler and filler rubber interaction. SEM imaging was used to characterize the morphology of the NC. The morphology distribution of N'SepS9 into N'SepS9-SSBR was correlated with the dynamic-mechanical data in order to understand the role of the ionic interaction in the enhancement of the NC properties.

4.3.1 Micro-structure and morphology N'SepS9-SSBR nanocomposite

SEM was employed to determine the dispersion state and compatibility of N'SepS9 and SepS9 in the rubber matrix. The fracture morphology of the reference SepS9-SBR and N'SepS9-SSBR are shown in Fig. 4.8.

By SEM micrograph (Fig. 4.8a), it is clearly shown that pristine SepS9 forms big agglomerates with random orientation inside the SBR matrix. This suggests both a poor interfacial adhesion and interaction between SepS9 and SBR that gives rise even to poor Sep dispersion.

In the other hand, image of N'SepS9 (Fig. 4.8b) shows the presence of interconnected structures, through both direct particles interactions, and their bridging by polymer chains. These superstructures, in which Sep fibers assemble, can be attributed to the electrostatic and ionic interaction between N'SepS9 and SSBR that gives rise to a synergistic effect between the polymer and nanofibers. In these superstructures, N'SepS9 fibers are highly oriented.

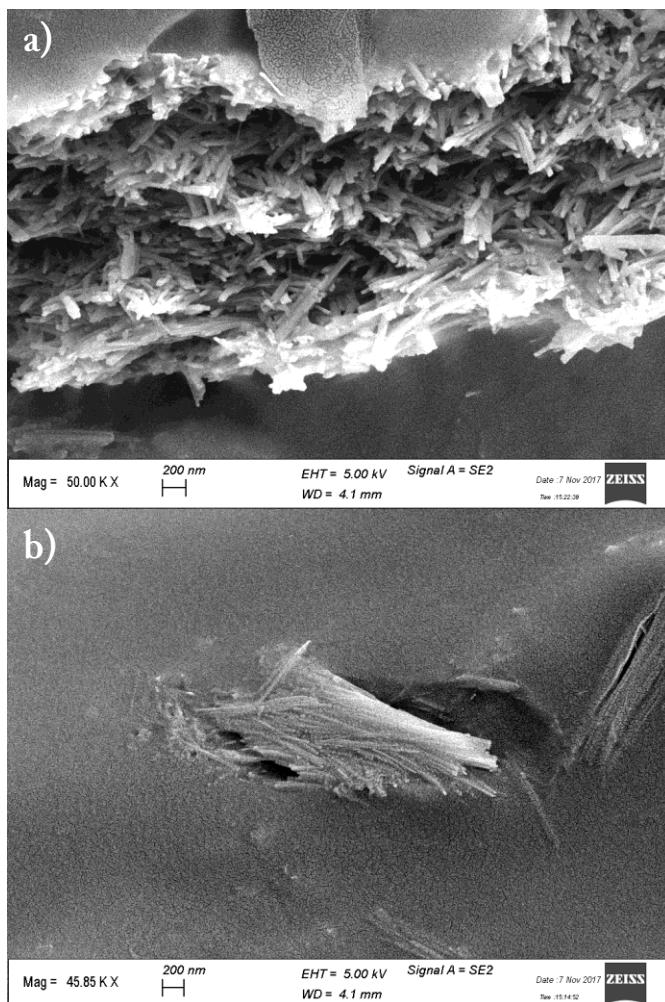


Figure 4.8 SEM images of a) SepS9-SBR and b) N'SepS9-SSBR

4.3.2 Mechanical properties of N'SepS9-SSBR

The effect of ionic interaction of N'SepS9-SSBR on mechanical properties was studied and compared with composite containing pristine Sep NPs and silica NPs.

The mechanical properties of neat SBR, N'SepS9-SSBR and N'SM30-SSBR NCs are illustrated in Fig. 4.9.

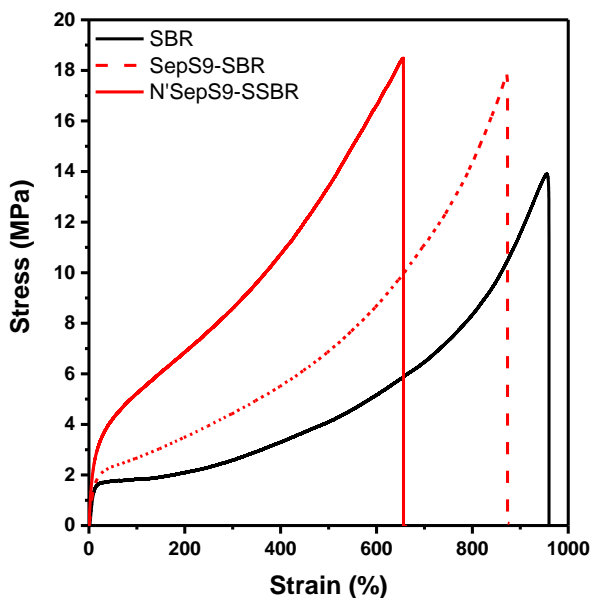


Figure 4.9 Stress-Strain curve for neat SBR (black line), SepS9-SBR (dashed red line) and N'SepS9-SSBR (red line).

The tensile strength, elongation at break and elastic modulus of neat SBR were 13.8 MPa, 950% and 3.37 MPa respectively. The addition of 10% w/w of pristine SepS9 in the SBR polymer lead to an increase of both tensile strength from 13.8 to 17.7 MPa and elastic modulus from 3.37 to 4.14 MPa, while the elongation at break is decreased to 870%.

However, in the case of N'SepS9-SSBR, the addition of the same amount of N'SepS9 on SSBR polymer produced a slightly higher tensile strength than that of the pristine form, equal to 18.5MPa, and a bigger increase of elastic modulus from 4.14 to 29.4 MPa, while elongation at break decreased to 655%.

This significant improvement in the tensile strength and elastic modulus of N'SepS9-SSBR can be related to the strong filler-rubber interaction that favors the organization of fillers into superstructures, as evidenced by SEM image. Moreover the strong ionic interaction provide the decrease in elongability in the

case of N'SepS9-SSBR, where the nanofibers act as a crosslinker and consequently making the NC brittle than the SepS9-SBR.

4.3.3 Temperature dependent dynamic-mechanical analysis

DMA measurements were performed to investigate the dynamic mechanical properties of N'SepS9-SSBR, SepS9-SBR and the neat SBR in order to examine the reinforcement efficiency of ionomer approach. The logarithms of storage modulus (E') and the loss factor $\text{Tan}\delta$ of the prepared NC versus temperature are shown in Fig. 4.10.

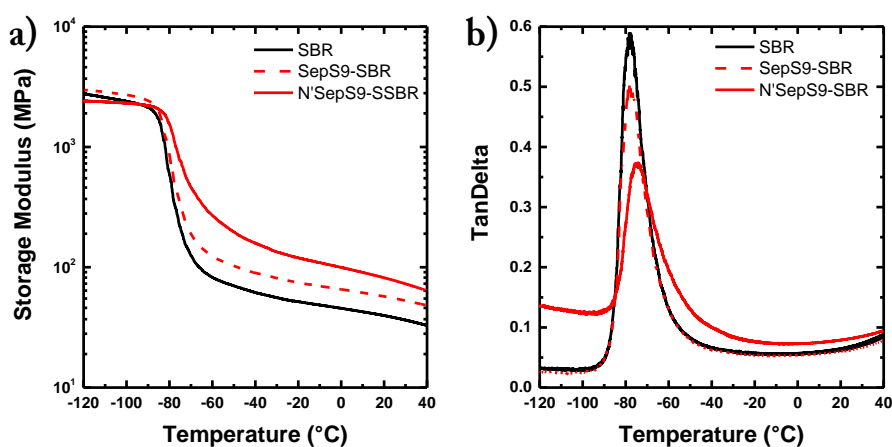


Figure 4.10 (a) Storage modulus and (b) $\text{tan}\delta$ vs. temperature of SBR (black line), SepS9-SBR (dashed red line) and N'SepS9-SSBR (red line).

E' value (Fig. 4.10a) of SepS9-SBR shows an improvement compared to that of neat SBR, as expected when fillers are introduced in the polymer matrix. In the case of N'SepS9-SSBR the improvement in E' value is much more significant, especially considering that the same filler loading was used for both NCs. This enhancement can be attributed to the creation of the ionic interactions that constrain the polymer chains at the filler surface, thus increasing the rigidity of the new NC.

$\text{Tan}\delta$ representing the ratio of the viscous part to the elastic part (E''/E') is an indicator of how efficiently the material loses energy due to molecular

rearrangements and internal friction. Table 4.2 reports the T_g values and the difference between T_g values of NCs and neat SBR.

Table 4.2 Data relative the T_g determination and the change in T_g

Sample	T _g (°C)	ΔT _g
SBR	-78.4	--
SepS9-SBR	-78.3	0.1
N'SepS9-SSBR	-74.9	3.5

SepS9-SBR doesn't show appreciable difference from that of the neat polymer. Only the lower value of T_g maximum peak is observed due to the introduction of the nanofibers [13].

More appreciable changes are noticeable for N'SepS9-SSBR: the lower value of T_g maximum peak, a shift of +3.5 °C of ΔT_g and the appearance of "shoulder" in the range of -60 to -40 °C This indicates that the ionic interaction introduces a higher degree of constrains in the polymer chains that require higher energy.

This data further confirms the idea that N'SepS9 act as a crosslinker in the N'SepS9-SSBR NCs.

4.4 Bibliography

- [1] A. Eisenberg and J.-S. Kim, *Introduction to ionomers*. Wiley, 1998.
- [2] S. Schlick, *Ionomers : characterization, theory, and applications*. CRC Press, 1996.
- [3] Z. Tong, B. Ren, and F. Gao, "Dual behavior of polyelectrolyte and ionomer for an ionizable polymer containing sulfonate groups in DMSO / THF mixtures," *Polymer (Guildf)*, vol. 42, no. 1, pp. 143–149, Jan. 2001.
- [4] C. Genies, R. Mercier, B. Sillion, N. Cornet, G. Gebel, and M. Pineri, "Soluble sulfonated naphthalenic polyimides as materials for proton exchange membranes," *Polymer (Guildf)*, vol. 42, no. 2, pp. 359–373, Jan. 2001.
- [5] V. . Deimede, K. . Fragou, E. . Koulouri, J. . Kallitsis, and G. . Voyiatzis, "Miscibility behavior of polyamide 11/sulfonated polysulfone blends using thermal and spectroscopic techniques," *Polymer (Guildf)*, vol. 41, no. 26, pp. 9095–9101, Dec. 2000.
- [6] D. A. Jackson, J. T. Koberstein, and R. A. Weiss, "Small-angle X-ray scattering studies of zinc stearate-filled sulfonated poly(ethylene-co-propylene-co-ethylidene norbornene) ionomers," *J. Polym. Sci. Part B Polym. Phys.*, vol. 37, no. 21, pp. 3141–3150, Nov. 1999.
- [7] N. J. Fernandes, T. J. Wallin, R. A. Vaia, H. Koerner, and E. P. Giannelis, "Nanoscale ionic materials," *Chem. Mater.*, vol. 26, no. 1, pp. 84–96, 2014.
- [8] A. B. Bourlinos *et al.*, "Functionalized nanostructures with liquid-like behavior: Expanding the gallery of available nanostructures," *Adv. Funct. Mater.*, vol. 15, no. 8, pp. 1285–1290, 2005.
- [9] D. Kim and L. A. Archer, "Nanoscale organic-inorganic hybrid lubricants," *Langmuir*, vol. 27, no. 6, pp. 3083–3094, 2011.
- [10] T. Kim, J. Kim, Y. Kim, T. Lee, W. Kim, and K. S. Suh, "Preparation and characterization of poly(3,4-ethylenedioxythiophene) (PEDOT) using partially sulfonated poly(styrene-butadiene-styrene) triblock copolymer as a polyelectrolyte," *Curr. Appl. Phys.*, vol. 9, no. 1, pp. 120–125, 2009.
- [11] M. R. Weir, W. Kuang, G. A. Facey, and C. Detellier, "Solid-state nuclear magnetic resonance study of sepiolite and partially dehydrated sepiolite," *Clays Clay Miner.*, vol. 50, no. 2, pp. 240–247, 2002.
- [12] J.-B. D. de la Caillerie and J. J. Fripiat, "A Reassessment of the ^{29}Si Mas-Nmr Spectra of Sepiolite and Aluminated Sepiolite," *Clay Miner.*, vol. 29, pp. 313–318,

1994.

- [13] V. Arrighi, I. . McEwen, H. Qian, and M. . Serrano Prieto, “The glass transition and interfacial layer in styrene-butadiene rubber containing silica nanofiller,” *Polymer (Guildf)*, vol. 44, no. 20, pp. 6259–6266, 2003.

Conclusions

The research activity focused to explore the possibility of employing Sep clay fibers as innovative fillers in rubber NCs, potentially exploitable in tires formulation.

Nano-sized anisotropic NS-SepX fibers were obtained thanks to a controlled acid treatment, which allows to maintain the particle morphology while tuning the surface chemistry. The acid treatment increases the number of silanol sites on the Sep surface and reduces the particle size from the micrometric to the nanometric dimension, while preserving the peculiar anisotropic features of the clay.

NS-Sep fibers were used by ex-situ blending to prepare SBR NCs whose mechanical properties were extensively evaluated and compared to those obtained by using pristine Sep as filler. Vulcanisable elastomeric materials containing modified Sep fibers show excellent properties of curing, reinforcement and hysteresis. This was related to the increase of bonding sites on the Sep surfaces that enhances the interaction with the coupling agent. Consequently, the interfacial chemical interaction between Sep fibers and rubber increases the fraction of the rigid polymer. In addition, inside the elastomeric matrix, the smaller size allows the self-assembly of fibers in the Sep network structure. This organization seems to be critical in the improvement of the mechanical properties in both cases, NS-SepX/SBR and NS-SilSepX/SBR with respect to the large-sized SepX and isotropic silica.

In the last part of the PhD activity, a different approach based on the NIMs philosophy was explored. Amino functionalized S was prepared and the introduction of sulfonic groups in the polymer chain was successful by using easy synthetic approaches. N'SepS9-SSBR composite was prepared by solution mixing and showed a better dispersion and interaction of modified Sep fibers with polymer matrix.

N'SepS9-SSBR NCs compared with SepS9-SBR demonstrated enhancement in the mechanical properties, especially in the elastic modulus and tensile strength.

Therefore, inside the functionalized elastomeric matrix, self-assembly of fibers was observed. These results suggest that both filler self-assembly and ionic interaction provide an improvement in the mechanical properties of N'Sep nanocomposites. Further analysis are needed to better understand this synergic effect that is given to the NC from the ionic interaction.

To sum-up, the whole results suggest that Sep clays, suitable modified, can be used as effective filler to design energy innovative tires. In the literature there is no reference to use advantageously of needle-like Sep nanofibers, as additional fillers in rubber and tire materials.

Appendix A:

Characterization Methods

The aim of this appendix is to resume the analytical techniques employed in this PhD thesis.

A1 SS-NMR: Hydrogen content of the sepiolite fillers from ^1H FID analysis

The total hydrogen content in each sepiolite filler was determined from the total intensity of the corresponding ^1H FID at $\text{ED} = 0$ (I_0) extrapolated with the procedure described in the main text. First, a calibration curve was built with the standard samples reported in Table S1, for which the weight and the total hydrogen content (H%, wt%) were known. A linear dependence of the measured I_0 to weight ratio on H% was found, as shown in Figure S1. The values of H% determined by interpolating the calibration curve for the different sepiolite fillers are reported in Table S2.

Table A1 Standard samples with known hydrogen content (H%, wt%): Adam. (Adamantane), HMB (hexamethylbenzene), IBU-S (Ibuprofen sodium salt), DSS (4,4-dimethyl-4-silapentane-1-

Standard	Purity (wt%)	H% (wt%)	sulfonic acid), K_2HPO_4
Adam.	≥ 99	11.7	
HMB	≥ 98.5	11.1	
IBU-S	≥ 98	7.9	
DSS	≥ 97	6.9	
K_2HPO_4	≥ 98	0.6	

(dipotassium hydrogenphosphate).

In order to determine the fraction of protons in rigid environments, the ^1H FID's recorded for the pure sepiolite fillers were analysed performing a discrete fitting with a linear combination of analytical functions, as described in the main text. The results are reported in Table S2. For all the fillers the ^1H FID's could be well reproduced with a linear combination of one Gaussian function (Gau) with a short T_2 of $\sim 18\text{--}20\ \mu\text{s}$, ascribable to dipolar coupled protons in rigid environments, and one or two exponential components with longer T_2 's of ~ 60 (exp1) and $250\text{--}370$ (exp2) μs , which can be ascribed to protons in more mobile environments and/or to isolated hydroxyl groups.

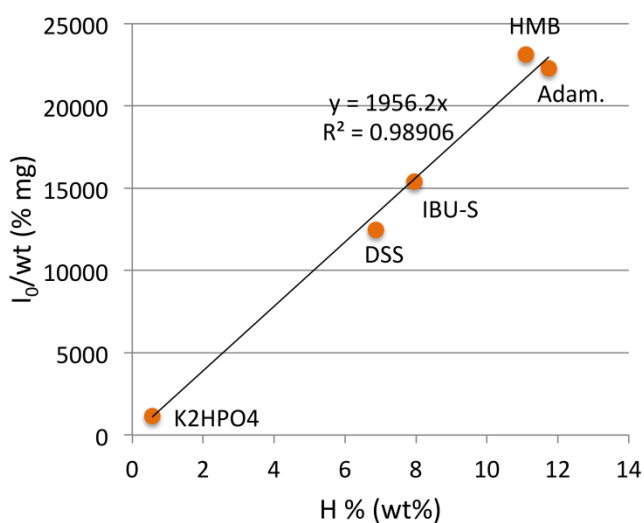


Figure A1 Calibration curve for the dependence of the total ^1H FID intensity to sample weight ratio (I_0/wt (%mg)) on the total hydrogen weight percentage (H%, wt%), built with the indicated standard samples.

Table S1. Results of the analysis of the ^1H FID's recorded for the pure sepiolite fillers. The total FID intensity to sample weight ratio (I_0/wt , %mg) and the total hydrogen content (H%, wt%) determined by interpolating the calibration curve in Table S1 are reported. For each component

of the ^1H FID (Gau, exp1 and exp2) the values of weight (w) and spin-spin relaxation time (T_2) obtained by the fitting procedure are also shown.

Filler	Gau		exp1		exp2		I ₀ /wt	H% (wt%)
	w (%)	T ₂ (μs)	w (%)	T ₂ (μs)	w (%)	T ₂ (μs)		
SepS9	48	20	52	60	-	-	3506	1.8
NS-SepS9	24	18	17	60	59	284	3358	1.7
NS-SilSepS9	62	18	17	60	22	249	4617	2.4
SepB5	43	20	51	60	7	245	4030	2.1
NS-SepB5	21	20	13	60	66	376	6048	3.1
NS-SilSepB5	67	19	29	57	4	351	5264	2.7

A2 Solid State NMR

Solid-state NMR (MAS-NMR) spectroscopy is a kind of nuclear magnetic resonance (NMR) spectroscopy, characterized by the presence of anisotropic interactions. Magic-angle spinning (MAS) is a technique often used to perform experiments in solid-state NMR spectroscopy.

By spinning the sample (usually at a frequency of 1 to 100 kHz) at the magic angle θ_m (ca. 54.74° , where $\cos 2\theta_m = 1/3$) with respect to the direction of the magnetic field, the normally broad lines become narrower, increasing the resolution for better identification and analysis of the spectrum.

In any condensed phase, a nuclear spin experiences a great number of interactions. The main three interactions (dipolar, chemical shift anisotropy, quadrupolar) often lead to very broad and featureless lines. However, these three interactions in solids are orientation-dependent and can be averaged by MAS. The nuclear dipole-dipole interaction, between magnetic moments of nuclei averages to zero only at the magic angle, θ_m . Another important technique is Cross Polarization. When combined with MAS, polarization from abundant nuclei like ^1H , ^{19}F and ^{31}P can be transferred to dilute or rare nuclei like ^{13}C ,

^{15}N , ^{29}Si in order to enhance signal to noise and reduce waiting time between successive experiments.

A3 Attenuated Total Reflectance Fourier Transform Infrared Spectroscopy (ATR-FTIR)

The surface chemistry of examined materials can be determined qualitatively by vibrational spectroscopy. The absorption of infrared radiation at different wavelengths is associated with the vibrational modes of different bonds. ATR spectroscopy uses the phenomenon of total internal reflection in a crystal. The radiation undergoes a total internal reflection when the angle of incidence at the interface between the crystal and the material is greater than the critical angle. The beam penetrates a fraction of a wavelength beyond the reflecting surface. When the material is in close contact with the reflecting surface, the beam loses energy at the wavelength where the material absorbs. The radiation resultant is measured (absorption energy) and plotted as a function of the wavelength. The measurements were performed by a Perkin Elmer Spectrum 100 instrument. (1 cm^{-1} resolution spectra, 650–4000 cm^{-1} region, 16 scan).

A4 Nitrogen physisorption measurements

Specific surface area, external surface area and porosity (pore volume and pore size distribution) was measured out by physical adsorption of N_2 . Regarding the porosity, in particular for pore diameter, an official classification was proposed by the International Union of Pure and Applied Chemistry (IUPAC): micropores (pore size < 2 nm), mesopores (pore size between 2 nm and 50 nm) and macropores (pore size > 50).

Adsorption is a phenomenon in which a fluid interacts with the surface atoms of solid by Van der Waals or weak forces (energies of interaction between adsorbent and adsorbed is in the order of 20 kJ/mol). Among the fluids used for

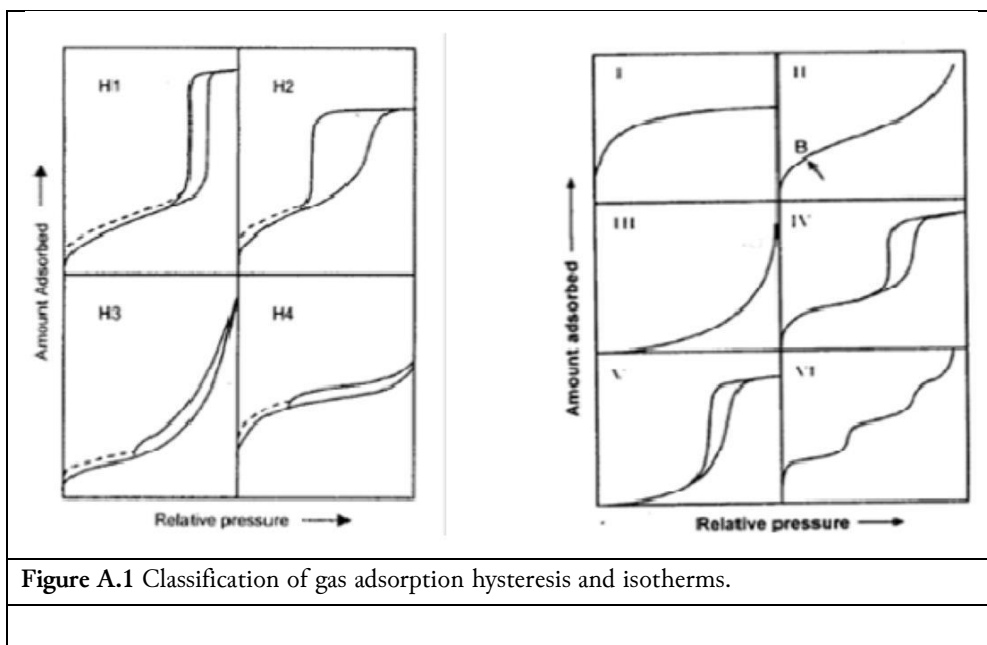
the physical adsorption measurements, N₂ is the most chosen because it is chemically inert and condenses at -196°C .

The increase of the amount of adsorbed fluid corresponds to a variation of pressure in dynamic equilibrium. Isotherm function represents the change of the equilibrium expressed as volume of the adsorbed gas as function of the relative pressure p/p_0 , where p is the pressure of the vapor and p_0 is its saturation pressure.

At low relative pressure the smallest pores are filled with nitrogen. As the pressure is increased further, larger pores are filled; near the saturation pressure, all pores are filled. The total pore volume is determined by the quantity of gas adsorbed near the saturation pressure.

The desorption isotherm rarely overlaps with that of adsorption, creating an hysteresis, due to the presence of pores in the adsorbent material. By studying the hysteresis shape it is possible to determine the total pore volume and size distribution of the pores.

The IUPAC classification recognizes six basic types of isothermes and four different types of hysteresis (Fig A.1): I isotherm is typical for microporous solids and chemisorption isotherms; type II is observed on finely divided non-porous solids, type III and type V are typical for vapor adsorption (e.g. water vapour on hydrophobic materials) and type IV and V feature a hysteresis loop, finally, the rare type VI steplike isotherm is seen on special types of carbons. Regarding the hysteresis, it is due to desorption on mesopores which occurs at lower pressures than those at which adsorption in similar-sized pores would take place.



There are 4 types of hysteresis shape,: H1(associated with solid homogeneous pore size), H2 (porous solids in which the distribution of the shape and size of the pores is not uniform and pores are not intersected with each other), H3 (solid pore forming flat shape (cracks) of non- uniform size); H4 (solid pore forming flat shape (cracks) of uniform size).

Different models can be applied to different regions of the adsorption isotherms to evaluate the specific surface area (e.g. BET method, Dubinin method, Langmuir adsorption isotherm, etc.), or the micro- and mesopore volume and pore size distributions (e.g. BJH method, Horvath and Kawazoe method, Saito-Foley method, etc.). The microporous volume is determined by the t-plot method of de Boer, while mesopore size and volume are determined by the Kelvin equation.

The analysis were carried out by a Quantachrome Autosorb-1 apparatus.

A5 Scanning Electron Microscope (SEM)

A scanning electron microscope (SEM) is a type of electron microscope that produces images of a sample by scanning it with a focused beam of electrons. The electrons interact with atoms in the sample, producing various signals that contain information about the sample's surface topography and composition. The apparatus consists in a column in which the electron beam is accelerated, a sample chamber in UHV condition to avoid collision of the beam with air molecules, a secondary electron detector. The most common SEM mode is detection of secondary electrons emitted by atoms excited by the electron beam. The number of secondary electrons that can be detected depends, among other things, on the angle at which beam meets surface of specimen, i.e. on specimen topography. By scanning the sample and collecting the secondary electrons that are emitted using a special detector, an image displaying the topography of the surface is created.

The types of signals produced by an SEM include secondary electrons (SE), reflected or back-scattered electrons (BSE), photons of characteristic X-rays and light (cathodoluminescence) (CL), absorbed current (specimen current) and transmitted electrons.

The signals result from interactions of the electron beam with atoms at various depths within the sample. In the most common or standard detection mode (secondary electron imaging or SEI), the secondary electrons are emitted from very close to the specimen surface. Consequently, SEM can produce very high-resolution images of a sample surface, revealing details less than 1 nm in size. Back-scattered electrons (BSE) are beam electrons that are reflected from the sample by elastic scattering. They emerge from deeper locations within the specimen and consequently the resolution of BSE images is generally poorer than SE images. However, BSE are often used in analytical SEM along with the spectra made from the characteristic X-rays, because the intensity of the BSE

signal is strongly related to the atomic number (Z) of the specimen. BSE images can provide information about the distribution of different elements in the sample. Characteristic X-rays are emitted when the electron beam removes an inner shell electron from the sample, causing a higher-energy electron to fill the shell and release energy. These characteristic X-rays are used to identify the composition and measure the abundance of elements in the sample.

Due to the very narrow electron beam, SEM micrographs have a large depth of field yielding a characteristic three-dimensional appearance useful for understanding the surface structure of a sample.

A6 High-Resolution Transmission Electron Microscopy (HRTEM)

HRTEM is a technique that allows to obtain images of a nanostructured material at a much higher resolution than SEM. The apparatus is made of an electron beam source, a series of electromagnetic lenses (at least 5) to accelerate the electron beam at very high speed (up to 100KeV), and an imaging system of the electrons going through the sample, which converts the diffraction pattern into a 2D image. Going into detail, the technique makes use of both transmitted electrons and electrons generated by interaction of the beam with the sample, that are elastically scattered in the direction of the imaging system. This means that the imaging system receives a diffraction pattern, that is reconstructed by the projection lens into a 2D image of the sample. Finally, the imaging plate on the bottom converts the incident electrons into visible light by fluorescence, and the visible image is detected by a CCD camera. The resolution depends mainly on the speed of the electron beam used, and modern HRTEM apparatus are able to resolve features as small as few nanometers.

A7 Oscillating Dish Rheometry (ODR) and stress-strain measurements

ODR measurements of the uncured SBR/SiO₂@POSS and SBR/SiO₂+POSS nanocomposites composites was performed by Rubber Process Analyzer (RPA 2000, Alpha Technologies) by applying a shear stress mode (Fig A.2).



Figure A2 Rubber Process Analyzer (RPA 2000, Alpha Technologies)

The strain sweep tests were carried out at 70°C and 1 Hz from 2 to 100% elongation. Same measurements was also performed on cured composites, after vulcanizing the crudes sample in the testing chamber at the optimum temperature. In this case the train sweep was carried out at 70°C and 10Hz, from 0.2 to 10 % elongation. Specimens were cut by using a Constant Volume Rubber Sample Cutter (CUTTER 2000, Alpha Technologies); the dimensions were 3.5cm diameter and 0,2 cm thick, the weight 4.5 ± 0.3 g. Two measurements were carried out for each sample and the average value was reported.

A8 Dynamic Mechanical Thermal Analysis (DMTA)

Dynamo mechanical measurements of the final material can be also conducted along a wide temperature range, above and below the glass transition

temperature of the material. The main interest in using DMTA as an additional dynamo mechanical technique are the identification of the correct glass transition temperature more precisely than DSC, as seen by the mechanical relaxation of polymer chains, and second, the identification of the relaxation modes different from the glass transition. In fact, while increasing the temperature other chain relaxation phenomena can occur, as a result of increasing entropy: for example, in polar polymers hydrogen bonds can break upon a certain temperature, allowing new segmental movements to take place, or in filled polymers the chains interacting with the filler surface can increase their mobility at temperatures that are different from the main glass transition. The instrument setup is composed by a thermostated chamber, in which the sample is a rectangular slab, champed on the upper part with a static clamp, and on the lower part with a moving clamp.

A9 Tensile Tests

Tensile testing is a fundamental materials science test in which a sample is subjected to a controlled tension until failure. The results from the test are commonly used to select a material for an application, for quality control, and to predict how a material will react under other types of forces. Properties that are directly measured via a tensile test are ultimate tensile strength, maximum elongation and reduction in area. From these measurements the following properties can also be determined: Young's modulus, Poisson's ratio, yield strength, and strain-hardening characteristics. Uniaxial tensile testing is the most commonly used for obtaining the mechanical characteristics of isotropic materials. For anisotropic materials, such as composite materials and textiles, biaxial tensile testing is required. The common testing machine has two crossheads; one is adjusted for the length of the specimen and the other is driven to apply tension to the test specimen. There are two types: hydraulic powered and electromagnetically powered machines.

The machine must have the proper capabilities for the test specimen being tested. There are four main parameters: force capacity, speed, precision and accuracy. Force capacity refers to the fact that the machine must be able to generate enough force to fracture the specimen. The machine must be able to apply the force quickly or slowly enough to properly mimic the actual application. Finally, the machine must be able to accurately and precisely measure the gauge length and forces applied; for instance, a large machine that is designed to measure long elongations may not work with a brittle material that experiences short elongations prior to fracturing. A dog-bone shaped specimen is gripped at its two ends and is pulled to elongate at a determined rate to its breakpoint; a highly ductile polymer may not reach its breakpoint. Figure A.6 shows also the standard configuration for tensile testing strip materials. This shape is commonly referred to as a dog bone, with wide ends and a narrow middle. The grips of the testing apparatus hold the specimen firmly at the wide ends. The midsection of the sample has a narrower width than the grip section. This concentrates the stress in the test area, so that fracture and most of the strain occur here. Strain is measured in this section, and stress is calculated from the force load on the grips. If any strain or deformation occurs outside of the test area, the test results will be inaccurate. However, if the fracture occurs outside of the area in which the strain is measured, the test results must be thrown out. It is therefore a good idea to prepare multiple samples if using straight-sided pieces.

A10 Inductively coupled plasma (ICP)

An inductively coupled plasma is a plasma that is energized (ionized) by inductively heating the gas with an electromagnetic coil, and contains a sufficient concentration of ions and electrons to make the gas electrically conductive. Even a partially ionized gas in which as little as 1% of the particles are ionized can have the characteristics of a plasma (i.e., response to magnetic fields and high

electrical conductivity).[citation needed] The plasmas used in spectrochemical analysis are essentially electrically neutral, with each positive charge on an ion balanced by a free electron. In these plasmas the positive ions are almost all singly charged and there are few negative ions, so there are nearly equal amounts of ions and electrons in each unit volume of plasma.

An inductively coupled plasma (ICP) for spectrometry is sustained in a torch that consists of three concentric tubes, usually made of quartz, although the inner tube (injector) can be sapphire if hydrofluoric acid is being used. The end of this torch is placed inside an induction coil supplied with a radio-frequency electric current. A flow of argon gas (usually 13 to 18 liters per minute) is introduced between the two outermost tubes of the torch and an electric spark is applied for a short time to introduce free electrons into the gas stream. These electrons interact with the radio-frequency magnetic field of the induction coil and are accelerated first in one direction, then the other, as the field changes at high frequency (usually 27.12 million cycles per second). The accelerated electrons collide with argon atoms, and sometimes a collision causes an argon atom to part with one of its electrons. The released electron is in turn accelerated by the rapidly changing magnetic field. The process continues until the rate of release of new electrons in collisions is balanced by the rate of recombination of electrons with argon ions (atoms that have lost an electron). This produces a 'fireball' that consists mostly of argon atoms with a rather small fraction of free electrons and argon ions. The temperature of the plasma is very high, of the order of 10,000 K. The plasma also produces ultraviolet light, so for safety should not be viewed directly.

The ICP can be retained in the quartz torch because the flow of gas between the two outermost tubes keeps the plasma away from the walls of the torch. A second flow of argon (around 1 liter per minute) is usually introduced between the central tube and the intermediate tube to keep the plasma away from the

end of the central tube. A third flow (again usually around 1 liter per minute) of gas is introduced into the central tube of the torch. This gas flow passes through the center of the plasma, where it forms a channel that is cooler than the surrounding plasma but still much hotter than a chemical flame. Samples to be analyzed are introduced into this central channel, usually as a mist of liquid formed by passing the liquid sample into a nebulizer.

To maximize plasma temperature (and hence ionization efficiency) and stability, the sample should be introduced through the central tube with as little liquid (solvent load) as possible, and with consistent droplet sizes. A nebulizer can be used for liquid samples, followed by a spray chamber to remove larger droplets, or a desolvating nebulizer can be used to evaporate most of the solvent before it reaches the torch. Solid samples can also be introduced using laser ablation. The sample enters the central channel of the ICP, evaporates, molecules break apart, and then the constituent atoms ionize. At the temperatures prevailing in the plasma a significant proportion of the atoms of many chemical elements are ionized, each atom losing its most loosely bound electron to form a singly charged ion. The plasma temperature is selected to maximise ionization efficiency for elements with a high first ionization energy, while minimising second ionization (double charging) for elements that have a low second ionization energy.